



Technische Universität München

Development of a CALIFA demonstrator benchmark experiment using (p,2p) reactions in direct kinematics

Doctoral dissertation

Benjamin Heiss



Institute E12 for
experimental physics



Technische Universität München

Development of a CALIFA demonstrator benchmark experiment using (p,2p) reactions in direct kinematics

Benjamin Heiss

Vollständiger Abdruck der von der Fakultät für Physik der Technischen Universität München zur Erlangung des akademischen Grades eines Doktors der Naturwissenschaften genehmigten Dissertation.

Vorsitzender: apl. Prof. Dr. Norbert Kaiser

Prüfer der Dissertation:

1. Prof. Dr. Laura Fabbietti
2. Prof. Dr. Stefan Schönert

Die Dissertation wurde am 19.11.2018 bei der Technischen Universität München eingereicht und durch die Fakultät für Physik am 13.12.2018 angenommen.

Abstract

The most exotic nuclei far beyond the 'Valley of Stability' will be studied at the new Facility for Anti-proton and Ion Research FAIR, currently under construction at the GSI Helmholtz Center for Heavy Ion Research in Darmstadt. One of the new experiments at FAIR is R^3B (Reactions with Relativistic Radioactive Ion Beams). The CALIFA calorimeter, based on a highly segmented CsI(Tl) crystal array is one of the key instruments for kinematically complete reaction studies in R^3B . Consisting of 2464 CsI(Tl) and 96 Phoswich detectors this electromagnetic calorimeter is specialized on γ -ray and light charged particle detection. The identification of high energy γ -ray and proton signatures in CsI(Tl) as well as separation of background reactions in the detector material is an important feature.

In the framework of this thesis an experiment using the $^{16}\text{O}(p,2p)^{15}\text{N}$ quasi-free scattering (QFS) reaction in direct kinematics was developed and performed for commissioning and calibrating the subunits of CALIFA, so-called petal detectors consisting of 64 CsI(Tl) crystals. Goal of the experiment was to determine overall energy resolution, detection efficiency and calibration accuracy for γ -rays and light charged particles and as well as their long term stability under realistic conditions. Also the particle identification and background separation was determined at high rates in a combined setup with additional tracking detectors. Key feature of the experiment was the use of a well localized water fiber target ($d = 460 \mu\text{m}$), enabling simultaneous measurements of elastic scattering on hydrogen nuclei for self-calibration and cross check purposes, while using the QFS reaction on the ^{16}O nuclei as a source of coincident protons and γ -rays. This enabled also a relative measurement of the cross section of the $^{16}\text{O}(p,2p)^{15}\text{N}$ reaction. A full scale GEANT4 simulation for the benchmark experiment was created from scratch with a newly written event generator integrated into the framework to study the response of the used detector system.

The experiment was performed with the support of different groups of the R^3B Collaboration at the Bronowice Cyclotron Center in Krakow using a monoenergetic proton beam of $E_p = 200 \text{ MeV}$. Here two petals constructed at the Lund University and one petal constructed at the TU Darmstadt were tested in preparation for the FAIR Phase 0 experiments. Additionally a large fraction of the full data acquisition system of CALIFA with it's FEBEX3 readout cards was tested using input data of 400 channels for the first time. Using a ^{60}Co source and elastic scattering data of a polypropylene target presented accurate calibration data regarding γ -rays and protons. The achieved resolution for γ -rays ranges from 4.98% to 6.06% at 1 MeV which is well within the requirements for CALIFA. The same is true for the proton total energy measurement, where 1.2% at 100 MeV were achieved. Additionally a proton/ γ separation using the QPID algorithm down to 1.2 MeV was possible. Employing the full event reconstruction the proton separation energy for ^{16}O were reconstructed from the calibration procedure to be $S_p = (12.22 \pm 0.02) \text{ MeV}$. In analogy to planned QFS experiments using CALIFA, the excitation energy of two first excited states of ^{15}N were reconstructed using Missing Mass spectroscopy. γ -rays of the 6.3 MeV excitation were detected in coincidence with the QFS protons with an efficiency $\epsilon_\gamma = (4.8 \pm 0.2)\%$. Finally the exclusive cross section for the ground and first excited $\frac{3}{2}^-$ state in the $^{16}\text{O}(p,2p)^{15}\text{N}$ reaction $\sigma_{p,2p}^{GS} = (7.88 \pm 0.79) \text{ mb}$ and $\sigma_{p,2p}^{GS} = (20.67 \pm 1.84) \text{ mb}$ were extracted. Based on the success of this work further experiments at the Krakow beam facility are already planned for more detector elements in 2019.

Die exotischsten Kerne weit jenseits des "Valley of Stability" werden an der neuen Einrichtung für Anti-Protonen- und Ionenforschung FAIR untersucht, welche derzeit am GSI Helmholtz-Zentrum für Schwerionenforschung in Darmstadt gebaut wird. Eines der neuen Experimente bei FAIR ist R^3B (Reactions with Relativistic Radioactive Ion Beams). Das CALIFA-Kalorimeter, das auf einem hoch segmentierten CsI(Tl)-Kristallarray basiert, ist eines der wichtigsten Instrumente für kinematisch vollständige Reaktionsuntersuchungen in R^3B . Bestehend aus 2464 CsI(Tl) und 96 Phoswich-Detektoren ist dieses elektromagnetische Kalorimeter auf die Detektion von γ -Dtrahlen und leichten geladenen Teilchen spezialisiert. Die Identifizierung von hochenergetischer γ -Strahlung und Protonen in CsI (Tl) sowie die Trennung von Hintergrundreaktionen im Detektormaterial ist ein wichtiges Merkmal.

Im Rahmen dieser Arbeit wurde ein Experiment mit der quasi-freien $^{16}\text{O}(p,2p)^{15}\text{N}$ Streureaktion (QFS) in direkter Kinematik zur Inbetriebnahme und Kalibration von Untereinheiten von CALIFA, sogenannten Petaldetektoren bestehend aus 64 CsI (Tl) -Kristallen, entwickelt und durchgeführt. Ziel des Experiments war es, die Gesamtenergieauflösung, die Detektionseffizienz und die Kalibrierungsgenauigkeit für γ -Strahlen und geladene Teilchen sowie deren Langzeitstabilität unter realistischen Bedingungen zu bestimmen. Auch die Teilchenidentifikation und Hintergrundtrennung wurde in einem kombinierten Aufbau mit zusätzlichen Tracking-Detektoren bei hohen Raten bestimmt. Das Hauptmerkmal des Experiments war die Verwendung eines gut lokalisierten Wasserfasertargets ($d = 460 \mu\text{m}$), das die gleichzeitige Messung der elastischen Streuung an Wasserstoffkernen für Selbstkalibrierungs- und Kontrollzwecke ermöglicht, während die QFS-Reaktion an ^{16}O -Kernen als Quelle für koinzidente Protonen und γ -Strahlen verwendet wird. Dies ermöglichte auch eine relative Messung des Wirkungsquerschnitts der $^{16}\text{O}(p,2p)^{15}\text{N}$ -Reaktion. Eine vollständige GEANT4-Simulation für das Benchmark-Experiment wurde von Grund auf mit einem neu geschriebenen Eventgenerator, der in das Framework integriert ist, erstellt, um das Verhalten des verwendeten Detektorsystems zu untersuchen. Das Experiment wurde mit Unterstützung verschiedener Gruppen der R^3B -Kollaboration am Bronowice Cyclotron Center in Krakau mit einem monoenergetischen Protonenstrahl mit $E_p = 200 \text{ MeV}$ durchgeführt. Hier wurden zwei an der Universität Lund und ein an der TU Darmstadt konstruiertes Petal zur Vorbereitung auf die FAIR-Phase-0-Experimente getestet. Außerdem wurde ein großer Teil des vollständigen Datenaufnahmesystems von CALIFA mit seinen FEBEX3-Auslesekarten zum ersten Mal mit Signalen von 400 Kanälen getestet. Unter Verwendung einer ^{60}Co -Quelle und elastischer Streuung an einem Polypropylyentarget wurden genaue Kalibrierungsdaten für γ -Strahlen und Protonen erzielt. Die erreichte Auflösung für γ -Strahlen reicht von 4,98% bis 6,06% bei 1 MeV, was den Anforderungen für CALIFA entspricht. Gleiches gilt für die Protonen-Gesamtenergiemessung, bei der 1,2% für 100 MeV erreicht wurden. Zusätzlich war eine Proton/ γ -Trennung mit dem QPID-Algorithmus bis 1,2 MeV möglich. Unter Verwendung der vollständigen Eventrekonstruktion wurde die Protonenseparationsenergie für ^{16}O aus der Kalibrierung zu $S_p = (12,22 \pm 0,02) \text{ MeV}$ rekonstruiert. In Analogie zu geplanten QFS-Experimenten mit CALIFA wurde die Anregungsenergie der zwei ersten angeregten Zuständen von ^{15}N mithilfe der Missing-Mass-Spektroskopie rekonstruiert. Die γ -Strahlen der 6,3 MeV-Anregung wurden in Koinzidenz mit den QFS-Protonen mit einer Effizienz von $\epsilon_\gamma = (4,8 \pm 0,2)\%$ detektiert. Schließlich wurde der exklusive Wirkungsquerschnitt für den Grund- und ersten angeregten $\frac{3}{2}^-$ -Zustand der $^{16}\text{O}(p,2p)^{15}\text{N}$ -Reaktion zu $\sigma_{p,2p}^{GS} = (7,88 \pm 0,79) \text{ mb}$ und $\sigma_{p,2p}^{GS} = (20,67 \pm 1,84) \text{ mb}$ extrahiert. Basierend auf dem Erfolg dieser Arbeit sind weitere Experimente in der Krakauer Strahlanlage bereits für das Jahr 2019 für weitere Detektorelemente geplant.

Contents

Abstract	iii
1 Introduction and Motivation	1
1.1 Models of the Atomic Nucleus	2
1.2 R ³ B and CALIFA	6
1.2.1 R ³ B Setup	6
1.2.2 Experimental Tools	8
1.2.3 Quasi-free scattering	9
1.2.4 The CALIFA Calorimeter	11
2 CsI(Tl) and Pulse Shape Analysis	15
2.1 Features of CsI(Tl)	15
2.1.1 Basic properties	15
2.1.2 Scintillation properties	15
2.1.3 Particle identification with CsI(Tl)	16
2.2 Pulse shape analysis	16
2.2.1 Baseline reconstruction	17
2.2.2 Moving Averaging Unit	17
2.2.3 Moving Window Deconvolution	17
2.2.4 Quick Particle Identification	18
3 Krakow experiment	23
3.1 Excitation of ¹⁵ N	24
3.2 Experiment Setup	26
3.2.1 Beam and Target	26
3.2.2 Detectors	28
3.2.3 Electronics and Data Acquisition	29
3.2.4 Setup	31
4 Full scale (p,2p) simulation	35
4.1 Simulation models for QFS	35
4.2 Simulation of Quasi-free scattering in Geant4	38
5 Data analysis	47
5.1 Calibration	47
5.1.1 γ calibration	47
5.1.2 Proton calibration with polypropylene target	49
5.1.3 Position calibration	51
5.2 Event selection	54
5.2.1 Vertex reconstruction	56
5.2.2 Selection of fully stopped protons	57
5.2.3 Selection of correlated pairs	58
5.3 Quasi-free scattering on Oxygen	61
5.3.1 Particle- γ -correlations	64
5.3.2 Momentum distribution and excitation energy	66

5.3.3 $^{16}\text{O}(p,2p)^{15}\text{N}$ cross section	69
6 Summary and Outlook	75
6.1 Resume	75
6.2 Improvements of the experiment setup	76
6.3 Light crosstalk in CALIFA	76
6.4 Outlook	78
A Appendix	85
A.1 Interstrip method	85
A.2 Petal Mapping	86
A.3 Elastic cross section data	88
Bibliography	93
Danksagung	97

Chapter 1

Introduction and Motivation

As apparent from the origin of the word "atom" from the Greek atomon (indivisible), the makeup of matter was already theorized about in the ancient times. The first mentioning of the atomic hypothesis by Leucippus and Democritus dates back to the fifth century BC. In India several schools also developed similar theories in the fourth century BC[1]. Of course at this time it was impossible to verify the existence of atoms, making this only theoretical considerations. A first "verification" of the atomic hypothesis was done by Ernest Rutherford 1911 by his famous scattering experiment of α -particles on a sheet of gold. This experiment laid the foundations of the modern atomic model as we know it today. Only a few years later it was found that the atomic nucleus is not indivisible, but in itself is made up of protons and neutrons. Further studies of the properties of the nucleus yielded certain proton and neutron numbers with increased stability. Following the Bohr Model of the electron shell, these states are associated with atomic shell closures for protons and neutrons (so called **Magic Numbers**), leading to the modern shell model of the nucleus[2].

In exotic nuclei with extreme proton-neutron ratios some observations are not explainable with the initial shell model's parameters and interaction models. For example some classical magic numbers vanish while new ones are discovered. In particular near the neutron drip line the nuclear structure has a huge impact on the creation of heavy elements in the *r*-process. The development of new theoretical models and their verification for the most neutron rich nuclei is therefore important for a deeper understanding of the atomic nucleus' structure and extrapolate to the r-process region which currently cannot be reached experimentally, especially in the very heavy region.

Investigating heavier elements the existing research institutes reach their limits regarding the creation of neutron rich isotopes and only a small portion of the suspected isotopes could already be studied. With the new research facility FAIR, currently under construction in Darmstadt, the region of experimentally accessible neutron rich isotopes will be expanded significantly. The most exotic secondary beams will be studied by the R³B experiment. It is a versatile high efficiency, acceptance, and resolution fixed target experiment with the aim of performing kinematic complete measurements to gain a full set of information for the reaction channels to study. This concept involves the detection and characterization of all particles emitted with high resolution. This effort involves many highly specialized detection systems and a superconducting dipole magnet with the electromagnetic CALIFA calorimeter playing a central role in the detection of γ rays and light charged particles. Regarding the experimental situation, the calorimeter has to meet challenging requirements in its data acquisition and analysis. A specially developed firmware for the front end electronics enabling dead time free signal processing of 3186 channels in real time. A special feature of this firmware is the QPID, enabling a on-line particle identification coupled with the capability of suppressing background induced by nuclear reactions and the energy reconstruction of particles punching through the detector material using the iPhos technique (see more in [3] and [4]).

The following thesis will start with a introduction to the nuclear shell model and their mod-

ifications for exotic nuclei. A short overview on FAIR, R³B and the CALIFA calorimeter will give an introduction to the requirements.

1.1 Models of the Atomic Nucleus

As first part of the introduction to the shell model, it is important to understand the historic evolution of nuclear theories. After a very successful description of the nuclear binding energy already in 1935 by Weizäcker([5]) and Bohr([6]) with the liquid drop model, the Fermi gas model was the first approach to describe also the internal structure of the nucleus.

Fermi Gas Model The Fermi gas model describes the nucleons as spin $\frac{1}{2}$ particles, moving independent and non-interacting in a potential well while obeying the Pauli exclusion principle. This well approximates the nuclear potential created by the overlap of the potentials of the particles inside the nucleus. If one now solves the Schrödinger equation for a single nucleon in this potential, the result is a ladder of discrete energy states. The occupation of these states is limited to two nucleons of one kind due to the Pauli exclusion principle, as shown in figure 1.1. Following the Fermi-Dirac statistics the available states are occupied starting with the energetically lowest one up to full occupation. Nucleons in the highest occupied state have the Fermi energy E_F and the Fermi momentum. The Fermi momentum depends on the density of the nuclear matter and thus is for heavy nuclei, whose density is nearly constant, $p_F = \frac{\hbar}{R_0} \left(\frac{9\pi}{8}\right)^{1/3} \approx 250 \text{ MeV}$ [7].

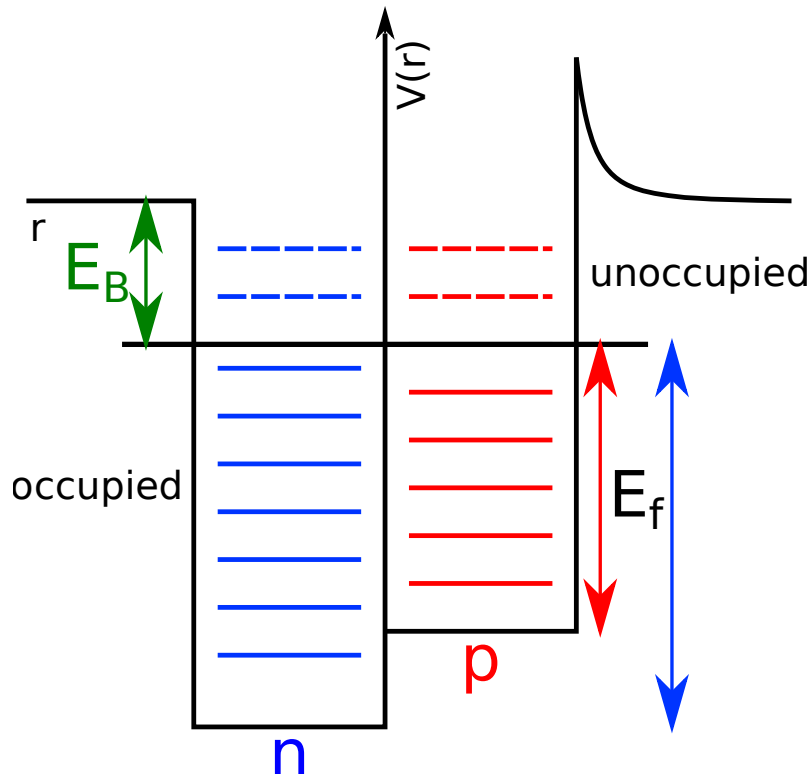


Figure 1.1: Potential well with energy states of protons and neutrons in the Fermi gas model. Due to the Coulomb repulsion the potential for the protons is lower than for neutrons. The Fermi energy E_f are thus different for the two different types of nucleons. Above the Fermi energy the states are unoccupied. To remove a nucleon from the potential well the binding energy E_B needs to be expanded (based on [2, p. 42])

Shell Model The Fermi gas model fails in explaining the observed magic numbers due to its rather simplistic assumptions concerning nuclear matter. Mainly two corrections on the Fermi gas model have to be taken into consideration to predict the magic numbers correctly thus taking the step towards the shell model.

The first correction consists of a more realistic nuclear potential that considers also the density distribution within the nucleus as the effective nuclear potential depends on the short-ranged inter nucleon interaction. As the density distribution follows a Fermi distribution, one can approximate the potential with the radial symmetric Woods-Saxon potential:

$$V_{Woods}(r) = \frac{-V_0}{1 + \exp\left(\frac{r-R}{a}\right)} \quad (1.1)$$

with the potential amplitude V_0 , the nuclear radius R and the "a" parameter describing the density distribution at the nuclear boundary. This leads to a removal of the degeneration of the nl states with the principal quantum number $n \in \mathbb{N}$ and the azimuthal quantum number $l \in \mathbb{N}_0$ and adds a dependency on the magnetic quantum number $m = -l, \dots, 0, \dots, l$. In this way the magic numbers 2, 8 and 20 are reproduced by shell closures for this values. For the rest of the magic numbers an additional potential term is needed.

The spin-orbit coupling adds such a term to the nuclear potential and is described by an additional ls -term in the potential[8]:

$$V_{tot}(r) = V_{Woods}(r) + V_{ls}(r) \frac{\langle ls \rangle}{\hbar^2} \quad (1.2)$$

Coupling spin and angular momentum leads to a total angular momentum $j = l \pm 1/2$ and a strong splitting of the energy states depending of spin orientation. States with anti-parallel spin-orbit coupling lie energetically above ones with parallel orientation. Looking at a energy level scheme with calculated single particle states in a nucleus using the shell model (figure 1.2), the magic numbers up to 126 are clearly visible as large gaps for neutron and proton shells both.

Explanation of the magic numbers being successful the shell model with spin-orbit interaction still does not account for all aspects of the interactions between the nucleons. This residual interaction influences especially the excitation spectrum of nuclei away from magic shells. As the nuclear potential is created by the nucleons themselves, a shift in it and the energy levels beyond closed shell configurations is probable for exotic nuclei. The tensor force between protons and neutrons is an expression of the nucleon's residual interaction indicating an angular dependency of the potential in addition to the radial dependency. Considering an orbital with a certain spin-orbit coupling $j_< = l - 1/2$ or $j_> = l + 1/2$, the $j_>$ states have a lower energy than the $j_<$ states, which is unlike the ordering in the atomic electron shells. Theoretical and experimental investigations indicate, that the tensor force arises from the pion-exchange part of the nuclear force[9]. These tensor forces are repulsive, if the spin of the neutron and proton couple to $S = 0$ and perpendicular to the radial distance between them, and attractive if their spins couple to $S = 1$ and parallel to their radial distance[10], as depicted in 1.3 a. This behavior modifies the single particle energies of an nucleon orbit depending on the orbital configuration of another kind of nucleon. In 1.3 b this is illustrated. By populating the neutron orbit $j_>$ the single particle energy of the proton $j_<$ orbital decreases while the one of $j_>$ increases due to tensor force interactions between neutrons and protons[10].

Thus single particle energies can be shifted in a way for classical shell closures to disappear and new ones to appear. Another important contribution to the residual interaction is the quadrupol moment deforming the nuclei's shape, which in turn leads to shifts in the energy levels[11, 12].

Predictions of the shell model concern also the so called "spectroscopic factor", which

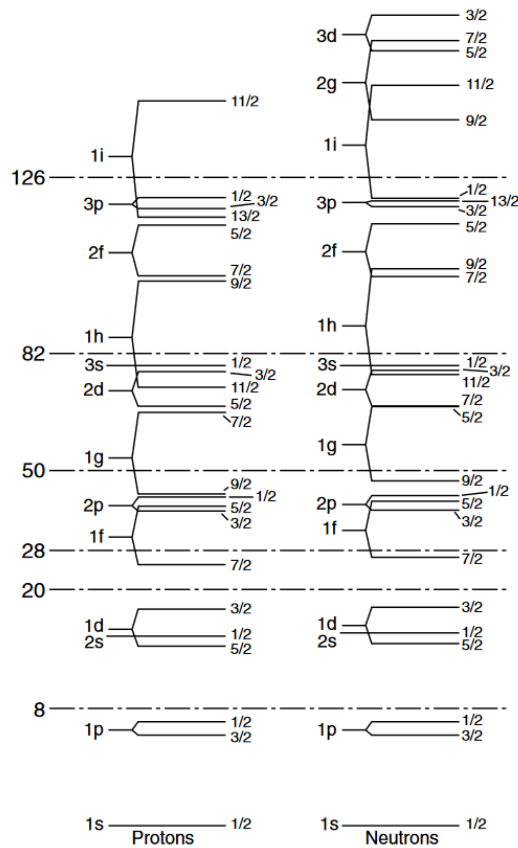


Figure 1.2: Single particle energy levels for nucleons using shell model calculations and their splitting due to the spin-orbit interaction introduced by Mayer-Goeppert and Jensen[8]. The shell closures and magic numbers appear at particularly large gaps between successive energy levels[7, p. 257]

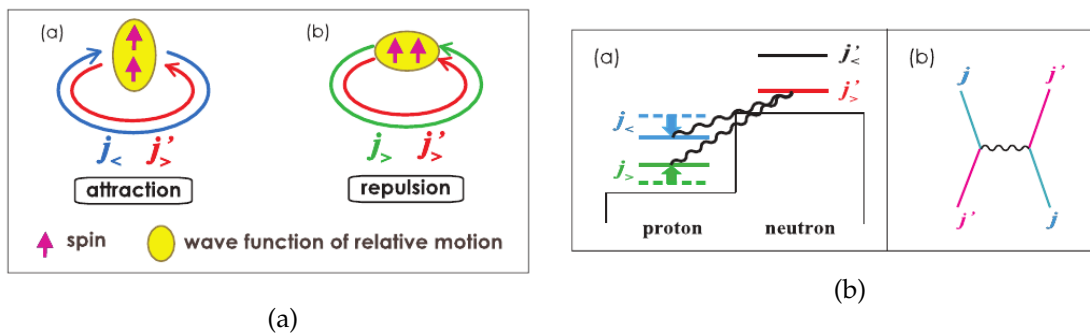


Figure 1.3: Illustration of the tensor forces in the interacting shell model. Figure a) illustrates the tensor force between a proton in the $j_>$ or $j_<$ orbit and an neutron in the $j_>'$ or $j_<'$ orbit. If the spins of the proton and the neutron couple constructively to a total spin of $S = 1$ and parallel to the radial distance between them, the force is attractive. In the opposed case of a coupling of the proton's and neutron's spin to $S = 0$ and perpendicular to the radial distance between the particles, the tensor force is repulsive. Figure b) illustrates the shifting of the orbitals energy due to the tensor forces between protons and neutrons interaction with pion exchange[10].

implies to what extent a removed single particle can be interpreted as an independent particle or a correlated state[13]. Effectively this expresses the fraction of the removed-nucleon's wave function in the initial state wave function of the nucleus of interest[14].

The theoretical partial cross section for a core state nI^π in a single-nucleon knockout reaction can be written as

$$\sigma_{theo}(nI^\pi) = \sum_j S_{c.m.}(nI^\pi, lj) \cdot \sigma_{s.p.}(B_N, lj) \quad (1.3)$$

where $S_{c.m.}(nI^\pi, lj)$ is the spectroscopic factor with a center of mass correction for the removal of a single nucleon with the quantum numbers (lj) [15]. The single particle cross section $\sigma_{s.p.}(B_N, lj)$ can be calculated using theoretical reaction models. In case of a single particle state, the spectroscopic factor should be equal to one and only the single particle cross section contributes. Using shell model calculations configuration mixing and correlations due to residual interactions causes the spectroscopic factor to be smaller than unity. Experimentally the spectroscopic factor $C^2S(exp)$ is defined as the ratio of the measured exclusive cross section σ_{exp} and the single particle cross section $\sigma_{s.p.}$ from theory. Calculating spectroscopic factors from harmonic oscillator basis requires transformation into center of mass system by multiplying them by the factor $(\frac{A}{A-1})^N$

$$C^2S_{c.m.}(theo) = C^2S(theo) * \left(\frac{A}{A-1}\right)^N = \frac{\sigma_{exp}}{\sigma_{s.p.}} * \left(\frac{A}{A-1}\right)^N \quad (1.4)$$

with the major oscillator quantum number N . The usual observable used is the so-called reaction factor R defined as the ratio of calculated and measured spectroscopic factors

$$R = \frac{C^2S_{exp}}{C^2S_{theo}} \quad (1.5)$$

An example of using the reduction factor in measurements is shown in figure 1.4 as a compilation of recent measurements for electron induced proton knockout and nucleon knockout reactions[16]. Here the reduction factor R is plotted as a function of the difference in separation energies of protons and neutrons ΔS . According to the figure, a one nucleon

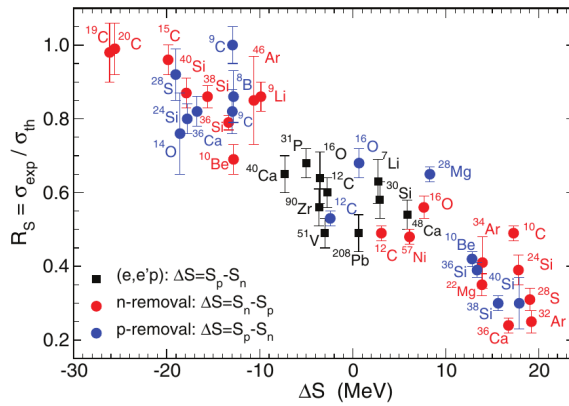


Figure 1.4: The dependence of the reduction factors R on the difference in separation energies of protons and neutrons ΔS [16].

knockout reaction exhibits a large reduction of the single-particle strength for the deeply-bound valence nucleons compared to shell model predictions. These calculations take the residual interactions into account, spreading the single particle strength over a large range of excitation energies. In spite of that, the observed tendency in figure 1.4 suggests a strong isospin asymmetry of nuclei and reflects the nucleon-nucleon correlations not included in the shell model calculations.

Another important impact of shell model calculation shows in the nucleosynthesis of

heavy elements in the early universe. As element creation beyond iron is energetically unfavorable by fusion, other effects are responsible. Through neutron capture with subsequent β -decay at intermediate neutron densities $10^7 - 10^{11} \text{ cm}^3$ during the carbon and helium burning in stars, heavier elements are created by the slow s process. It is dominated by the β -decay and thus follows the valley of stability[17]. At high neutron densities and temperatures ($T > 10^9 \text{ K}$) the speed of the neutron capture increases far beyond the β -decay, the process is called r process[11]. From the equilibrium between photo dissociation and neutron capture the natural abundance of isotopes is created. Due to the high neutron capture rate the equilibrium is shifted to low binding energies and high neutron to proton ratios. These low binding energies restrict the subsequent β -decay's phase space, which would create $Z+1$ isotopes, and so the β -decay is far slower than the neutron capture. Predicting the r process path and so the isotope abundance depend strongly on the nuclear properties, like neutron separation energies and life time. To describe the process a precise knowledge of modifications introduced in exotic nuclei's shell structure is essential.

The in this section discussed models represent two established theories on the atomic nucleus. To increase and proof the accuracy of predictions made using these models, many beam facilities and experiments exists around the globe. One facility dedicated to investigation of exotic heavy ions is discussed in the following section.

1.2 R³B and CALIFA

One possibility for performing experiments with exotic nuclei is using the so called "In Flight" production. A light elements production target is irradiated by a high intensity stable heavy ion beam, producing a cocktail of different nuclei through fission or fragmentation reactions. To choose a single isotope, the composition of this mixture is characterized by a fragment separator. The "Facility for Antiproton and Ion Research" (FAIR, cf. figure 1.5), which is currently under construction in Darmstadt, Germany, utilizes this method for creation of exotic, ultra relativistic secondary beams with the highest intensities [18]. Already in the first stage, FAIR will use the SIS 100 synchrotron for accelerating even the heaviest ions up to 35 AGeV with an intensity of up to $5 \cdot 10^{11} \text{ s}^{-1}$ [18]. Due to this high primary beam intensity coupled with a large phase space acceptance ($40\pi \text{ mm mrad}$ in x- and y- direction) the multi stage fragment separator Super-FRS will supply exotic secondary beam with up to 1 AGeV and an intensity increased by 10^5 compared to the existing FRS [19]. One experiment of particular interest being supplied by the Super-FRS will be the R³B experiment discussed here.

1.2.1 R³B Setup

The R³B experiment (Reactions with Relativistic Radioactive Beams, figure 1.6) is located in the high energy branch of the Super-FRS and will conduct experiments with exotic nuclei in inverse kinematics. Essentially R³B is a fixed target dipole spectrometer with a large opening superconducting magnet GLAD [21] with a field integral of 4.8 Tm. Together with a sophisticated detector arrangement this allows for kinematically complete measurements to select individual reaction channel in a complicated heavy ion collision. This new concept requires the detection of all target- and projectile-like reaction products thus a large acceptance of all detectors is mandatory. In inverse kinematics the exotic and radioactive beam nuclei are accelerated to ultra relativistic velocities ($\beta > 0.7$). The resulting Lorentz boost of the emitted reaction products leads to a preferred emission into the forward direction in the laboratory frame. This focussing of the beam like reaction products through the large opening of the GLAD magnet allows for a large acceptance

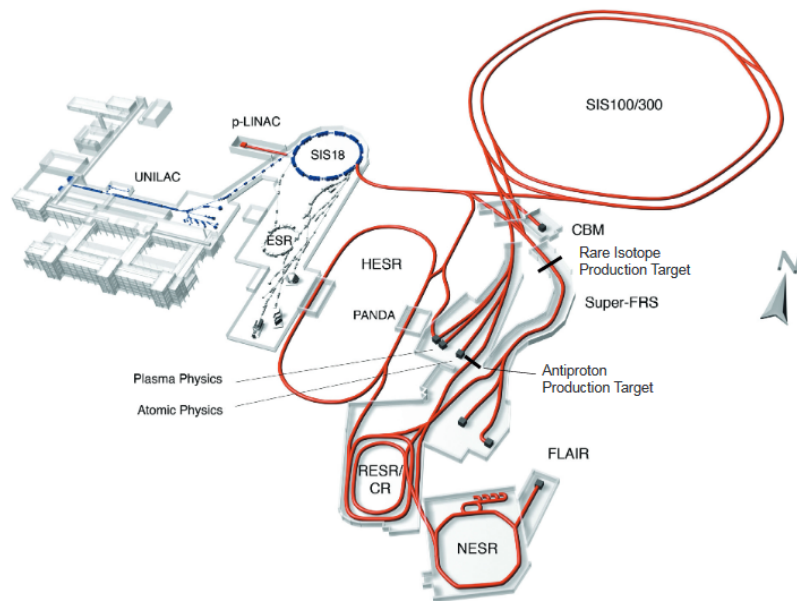


Figure 1.5: The Facility for Antiproton and Ion Research (FAIR) extends the existing GSI Facility in Darmstadt.[18]

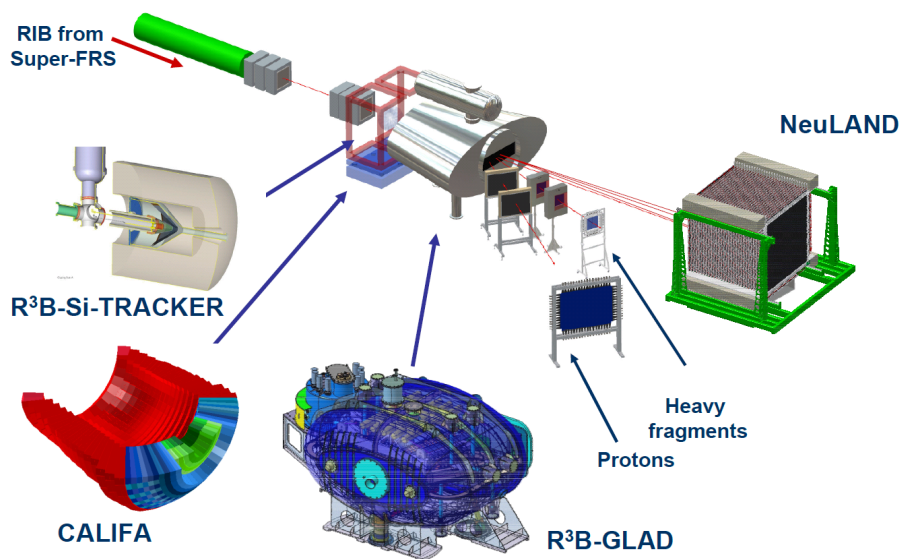


Figure 1.6: Overview over the individual detectors of the R^3B experiment. The radioactive ion beam supplied to the experiment by the Super-FRS irradiates the target area. Projectile-like charged particles and heavy fragments are analyzed by the GLAD dipole magnet and subsequent detectors. Neutrons are detected by the NeuLAND detector. Target-like charged particles and γ -rays are detected by the CALIFA calorimeter. Additionally the L^3T silicon tracker is used for vertex reconstruction.[20]

in the center of mass system even using detectors covering just small solid angles in the laboratory frame. Therefore the R^3B experiment's detectors are positioned mainly downstream of the target, maximizing the acceptance. The individual detection units used to achieve the goal of kinematically complete measurements are introduced in the following (cf. figure 1.6).

The exotic beam is created by irradiation of a production target. This secondary beam consists of multiple isotopes being separated by the Super-FRS[19]. Measuring the mo-

momentum of the incoming secondary beam is done by Time-of-Flight (ToF) measurements using plastic scintillators at the Super-FRS and the R³B experiment site. For in beam tracking of the incoming exotic beams position sensitive silicon detectors (PSP) are used. Using the beam's position on PSP and the energy loss ΔE , the ion's charge Z and the reaction's vertex position can be reconstructed [22]. The exotic irradiates the target just 1 m before the superconducting dipole magnet GLAD (GSI Large Acceptance Dipole) entrance window [21]. From there in forward direction emitted ($\Theta_{\text{lab}} < 7^\circ$) reaction products are analyzed using GLAD's high magnetic field integral of 4.8 Tm. The charged particles are deflected by their momentum to charge ratio with position sensitive detector's fiber detectors before and after GLAD measuring the bending radius. In addition ToF detectors positioned before and after GLAD measure the reaction product's momentum. To determine the momentum of emitted neutrons, the high resolution NeuLAND detector is used. NeuLAND, a highly segmented plastic scintillator array of 2.5 m long bars with PMT readout and a total detector volume (2.5 x 2.5 x 3.0) m³. The target region is surrounded by a multi layer silicon tracking detector for vertex reconstruction. Around this tracker the electromagnetic calorimeter CALIFA (cf. 1.2.4) is positioned, for detection of γ -rays and light charged particles emitted at large polar angles.

This complex detector setup enables a kinematically complete measurement of heavy ion reactions and allows for research on their nuclear structure. In this concept enables the usage of the following experimental methods.

1.2.2 Experimental Tools

Coulomb excitation Through the high electromagnetic field of high Z nuclei, the study of collective excitation modes or photo disintegration reactions are possible. In peripheral heavy ion collisions energy is transferred in the frame of the moving ion through the electromagnetic field to the target nucleus in a inelastic scattering reaction. Due to the Lorentz contraction at high beam energies, the mutual electromagnetic field contains high frequencies up to several MeV/ \hbar . These high frequencies enable the studies of surface vibrations and particular giant resonances like the giant dipole resonance. Direct, non-resonant transitions to the continuum for weakly bound nuclei can also occur. Determining the energy threshold of these reactions gives information on the single-particle structure, particular on the spacial distribution of the valence nucleons [23, 24].

Fission reactions By electromagnetic excitation or inelastic scattering of a exotic beam nucleus in the target, fission fragments are created. Fission is one of the most promising tools of deducing information on nuclear viscosity, shell effects and collective excitations at extreme deformation. The full isotopic distribution of the fission fragments is a sensitive signature of the excitation energy at which fission occurs[24, 25].

Knockout/Quasi free scattering To study single particle properties of the exotic nuclei, the scattering of protons on nucleons can be used. At high beam energies of up to 700 AMeV the nucleus is mainly transparent for the reaction products enabling not only study of the tails of the nucleons wave function (knockout) but also of deeper bound states (quasi free scattering). This reaction type is discussed in more detail in section 1.2.3.

An exceptional tool for investigating the properties of well-known and exotic nuclei is using Missing Mass Spectroscopy in analyzing quasi-elastic (p,2p) knock-out reactions. In this case the two emitted protons contain all of the kinematic information on the excitation of the heavy residual nucleus. Combined with the exclusive kinematics of this quasi-free scattering (QFS) process, it is unique in comparison with any and all other reactions. As future experiments aim on investigating exotic and unstable nuclei, they are created

through a production target. These nuclei impinge on a hydrogen containing target (pure or organic compound), scattering one of the projectile's protons off the hydrogen nucleus. In contrast to the inverse kinematics, this reaction can be investigated in normal kinematics as well. Here the nucleus of interest is used as target, irradiating it with a proton beam. Using normal kinematics in a QFS reaction is especially of interest if a stable isotope is investigated, for example as part of a demonstrator test analysis. In the following the systematics of Missing Mass Spectroscopy in QFS reactions are shortly explained in normal kinematics.

1.2.3 Quasi-free scattering

The quasi-free scattering (QFS) describes the reaction process between two nucleons, whereas one is bound within the potential of a nucleus while the other is not. At relativistic energies the sudden approximation applies. This states, that when the Hamiltonian of the nucleus is changed suddenly, it cannot catch up with the change and basically remains in spectator status. Thus the two nucleons collide directly with each other making the reaction "quasi-free". If the energy transfer exceeds the bound nucleons separation energy, it is knocked out of the nucleus. After the reaction takes place, the nucleons leaving the A-1 nucleus' potential can interact again with it (final state interaction). These result in the best case only in a low rescattering changing the kinematics of the reaction only slightly (eikonal ansatz). After the knock-out reaction, the remaining ones populate in most cases a set of excited states. For low excitation energies E^* emission of γ radiation is the only possible deexcitation mode. For E^* larger than the separation energy S_N the probability is high to reduce the excess energy by a particle emission first with successive γ -ray emission to reach the ground state. Different excitation modes can be generated depending on the reaction type and beam energy, making it possible to measure all parts of the nuclear wave function. To investigate single particle states of exotic nuclei knock-out and QFS reactions are suited ideally due to their relatively large cross section. Generally speaking ((p,2p)) scattering is an inelastic process between a free proton and a nucleus with high probability of residual excitation. In analogy the reaction corresponds to an elastic process between two protons, providing detailed insight into the intrinsic momentum distribution of the nucleus [26].

In free scattering, the collision of two objects with equal mass in a non-relativistic laboratory frame is described by a polar opening angle $\vartheta = 90^\circ$ and a azimuthal opening angle $\varphi = 180^\circ$. The overall momentum is conserved and distributes between the two scattered objects (\vec{p}_1 and \vec{p}_2) proportionally to their respective polar angles θ_1 and θ_2 .

$$|\vec{p}_1| \propto \frac{1}{\cos \theta_1 + \frac{\sin \theta_1}{\cos \theta_2}} \quad (1.6)$$

As this equation holds even under relativistic circumstances and the Lorentz boost, for a well known incident momentum of both particles, reduces the polar opening angle. If now a proton scatters on another free proton, measuring the emission angles determines also the protons momenta in the system. Looking at a proton bound in the nucleus' potential V caused by the neighboring nuclei and its excitation E^* , we find, that the whole scattering is actually a three-body interaction between two proton and a heavy residue with A-1. Figure 1.7 shows the reaction in normal kinematics in the lab frame. One proton scatters on a bound one inside the heavy target nucleus while the residual is a spectator to the reaction. To remove the target proton from inside the nucleus, the energy transfer from the incoming proton needs to exceed the binding energy E_B . The reaction is considered quasi-free, if $E_{\text{beam}} \gg E_B$. Additionally the possibility of final state interactions (FSI) needs to be considered, especially for energetically asymmetric scattering of the protons, as

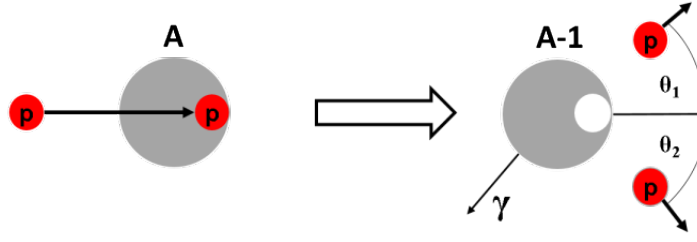


Figure 1.7: Sketch of a (p,2p) reaction in normal kinematics. The beam proton scatters on a bound one in the A nucleus at rest and knocks it out. After the reaction the two protons are emitted with polar angles $\theta_{1,2}$. The residual A-1 nucleus is left at the target position as spectator. If the reaction populates an excited state of the A-1 nucleus, emission of γ radiation becomes possible.

the cross section of proton-nucleon scattering increases with decreasing energy[27]. This can be seen in figure 1.8 showing the cross section of proton-proton and proton-neutron scattering below 200 MeV. Note the increase in cross section for proton energies below

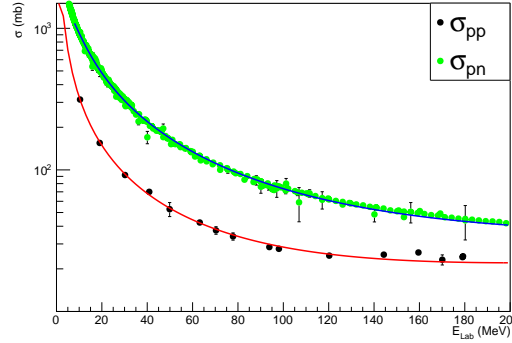


Figure 1.8: Cross section for proton-proton and proton-neutron scattering at energies below 200 MeV[28]. Both cross sections increases strongly for decreasing proton energy. In case of the (p,2p) reaction at low beam energy leads to an increasing probability of final state interactions in the shape of re-scattering of protons with energies below 60 MeV off the nucleons.

60 MeV leading to a increased opacity of the target nucleus for protons passing through it as in turn the probability of FSIs in shape of re-scattering of the low energy proton off the residual nucleus' constituents. This should be noticeable especially in the case of asymmetric polar angle emission, where the proton emitted at high polar angle only carries a small amount of kinetic energy and thus the probability of re-scattering increases. Recognizing the effects of FSIs is especially of concern for the proper reconstruction of the residual nucleus' excitation energy which will be discussed in the following.

Through application of the energy conservation the relation is true for the binding energy:

$$E_B = S_N + E^* = T_{p1} - (T'_{p1} + T'_{p2} + T'_{A-1}) \quad (1.7)$$

with T being the kinetic energy before and T' after the collision. As four momentum conservation holds true, we gain from the separation energy S_N and the excitation energy E^* an insight into the localization of the knocked-out proton inside the residual nucleus. This binding energy leads to a reduced rest mass of the proton, which in turn means, the correlation in 1.6 smears out, breaking the conservation.

The reduced mass of the proton can be translated into the invariant mass Q of the residual

nucleus can be derived from the 4-momentum conservation:

$$\begin{pmatrix} m_A \\ 0 \\ 0 \\ 0 \end{pmatrix} + \begin{pmatrix} E_{p1} \\ 0 \\ 0 \\ p_{zp1} \end{pmatrix} = \begin{pmatrix} E'_{p1} \\ p'_{xp1} \\ p'_{yp1} \\ p'_{zp1} \end{pmatrix} + \begin{pmatrix} E'_{p2} \\ p'_{xp2} \\ p'_{yp2} \\ p'_{zp2} \end{pmatrix} + \begin{pmatrix} E'_{A-1} \\ p'_{xA-1} \\ p'_{yA-1} \\ p'_{zA-1} \end{pmatrix} \quad (1.8)$$

assuming the beam proton is directed in z-direction and the target nucleus is at rest. Equation 1.8 delivers four relations for the unknown quantities of the A-1 nucleus. Using the energy-momentum relation $m = Q = \sqrt{E^2 - |\vec{p}|^2}$, Q can be expressed by the following equation:

$$Q = \sqrt{(m_A + E_{p1} - (E'_{p1} + E'_{p2}))^2 - ((p'_{xp1} + p'_{xp2}))^2 - ((p'_{yp1} + p'_{yp2}))^2} \quad (1.9)$$

$$- (\sqrt{E_{p1}^2 - m_{p1}^2} - (p'_{zp1} + p'_{zp2}))^2 \quad (1.10)$$

To get to the excitation energy E^* one has to remember it being just the difference from the systems missing mass Q and the residuals rest mass m_{A-1} .

$$E^* = Q - m_{A-1} \quad (1.11)$$

where E^* is the equated with equation 1.7, since even though the binding energy is distributed among both protons, in the repulsion the momentum transfer to the residual reflects the internal momentum of the knocked out proton.

In summary this shows the simplicity and beauty of missing mass spectroscopy in normal kinematics. Measuring only the two outgoing protons energy, we can directly derive the excitation spectra of the residual A-1 nucleus. In the following the CALIFA calorimeter is introduced as the R³B's central instrument for proton and γ -rays detection.

1.2.4 The CALIFA Calorimeter

The "CALorimeter for In Flight detection of γ -rays and light charged particles" (CALIFA, figure 1.9) is a highly segmented (2560 detectors) 4π calorimeter and a major component of the R³B experiment. CALIFA is optimized for detection of γ -rays in an energy range of $100 \text{ keV} \leq E_\gamma \leq 30 \text{ MeV}$ and light charged particles with energies up to 700 MeV. CALIFA is the result of an intense and long R&D program performed within a large international consortium of the R³B collaboration. Major requirements for the instrument are defined in the TDR for the Barrel [29] and the Endcap [30]. These requirements are for energy resolution of γ -rays should not be worse than 6% at 1 MeV as well as the resolution of the protons' total energy should not be below 1% at 100 MeV. Due to the high demands on CALIFA, the calorimeter is separated into three part, each specifically designed for different requirements, the Barrel, the iPhos and CALIFA Endcap Phoswich Array (CEPA):

Barrel The Barrel part covers a polar angular range of $43^\circ \leq \theta \leq 140^\circ$. Here the lowest energies and intensities of reaction products are expected. Due to the Doppler shift of the emitted γ -rays a high segmentation is still needed for the reconstruction of γ -ray energies in the emission system. Thus the Barrel consists of 1952 CsI(Tl) scintillator crystals distributed over several sizes. The crystal length and segmentation is highest starting at $\Theta = 43^\circ$, with 22 cm length, corresponding to a maximum proton energy $E_p \leq 319 \text{ MeV}$. The length of the crystals decreases with increasing polar angle.[20]

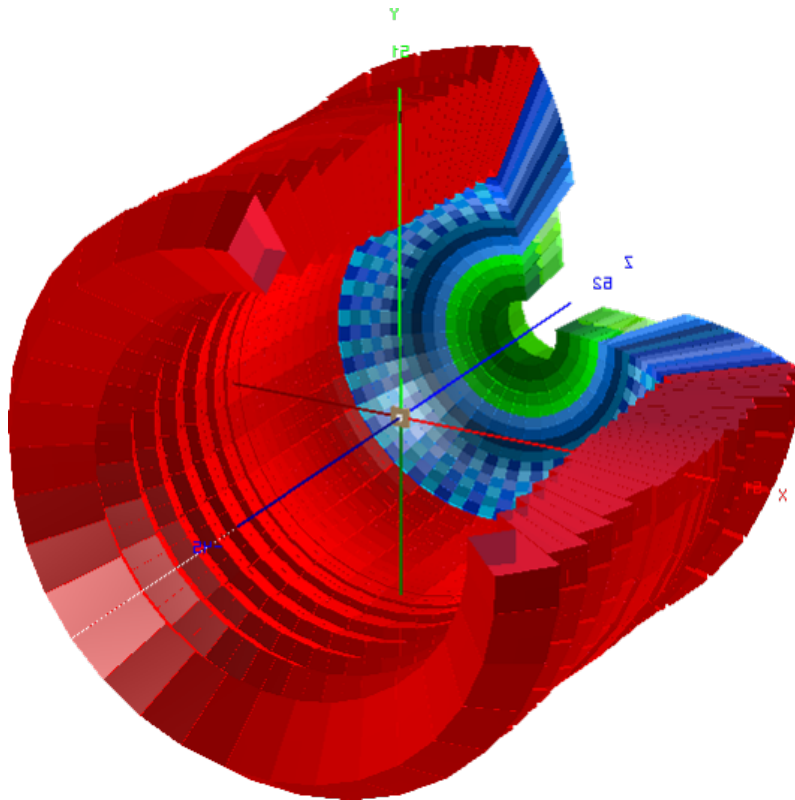


Figure 1.9: Schematic picture of the CALIFA calorimeter with its three parts. This highly segmented calorimeter is made up of 2560 detector units, which are divided into the Barrel (red, 1952 CsI(Tl) crystals), the iPhos Endcap (blue, 512 CsI(Tl) crystals) and the CEPA (green, 96 LaBr₃(Ce)/LaCl₃(Ce) phoswich detectors) part[20]

iPhos Endcap The iPhos (intrinsic Phoswich) endcap region covers polar angles $19^\circ \leq \theta \leq 43^\circ$. Here the expected proton energies reach up to 700 MeV, which could only be stopped within 74 cm long CsI(Tl) crystals. Such a crystal length would for once worsen the resolution of γ -ray detection due to the inhomogeneous light collection, and secondly increase the probability of nuclear reactions inside the active detector material, losing full energy peak efficiency in the process.

To avoid these issues 512 CsI(Tl) crystals of 22 cm length are used in the iPhos mode part[31]. As the crystals cannot stop most protons with the expected energies a method of energy reconstruction is required. Through pulse shape analysis (PSA) of the CsI(Tl) signals a powerful method to identify particle species with the additional benefit of identifying punch-through events is available in real time. Punch-through identification enables a $\Delta E/E$ separation of the detected events in the endcap, selecting the ones where energy reconstruction is necessary. This technique was specially developed for CsI(Tl) and is additionally used for suppressing nuclear reactions. More details can be found in [32].

CALIFA Endcap Phoswich Array (CEPA) In the most forward section ($7^\circ \leq \theta \leq 19^\circ$) the highest energies and intensities for γ -rays and charged particles are expected due to the Lorentz boost. As previously described in the iPhos section fully stopping the particles emitted into this region is not viable. A better solution in this case is using 96 Phoswich detectors consisting of a 7 cm long LaBr₃(Ce) and a 8 cm long LaCl₃(Ce) crystal each, which are optically coupled and then read out with single photo multiplier tube. Using pulse shape analysis the energy deposited in each crystal can be separated, allowing a $\Delta E-\Delta E$ measurement for reconstruction of the full energy for particles punching through the detector. Compared to CsI(Tl), the response of the CEPA detectors is much faster,

giving it an edge concerning the higher rates in the region this close to the beam line. In addition the Doppler broadening in this region being the smallest, CALIFA profits most from the better intrinsic γ -resolution of 4% at 662 keV in this expensive material used in the CEPA. Additionally near the beam line, the reconstruction of Compton scattering using the phoswich configuration, as here an opening exists where loss of γ -rays is relevant[31].

Chapter 2

CsI(Tl) and Pulse Shape Analysis

As described in the introduction, the main component of the CALIFA calorimeter is thallium-doped Cesium Iodide (CsI(Tl)). This crystalline scintillator has various interesting properties that will be discussed in the following section as well its use in pulse shape analysis.

2.1 Features of CsI(Tl)

2.1.1 Basic properties

Due to its elemental composition and its large light output, the inorganic scintillator CsI(Tl) has a rather good detection efficiency for a large range of γ energies ($0.1 \text{ MeV} < E_\gamma < 15 \text{ MeV}$), which fits the requirements of the CALIFA calorimeter. An intrinsic energy resolution of $\frac{\Delta E}{E} \leq 4.9\%$ for 662 keV γ s was achieved on small samples and with an APD readout system [33]. With a density of $4.5 \frac{\text{g}}{\text{cm}^3}$, it provides a high stopping power for charged particles ($-\frac{dE}{dX} \propto \frac{Z \cdot q}{A}$). The light yield of about $65000 \frac{\text{ph}}{\text{MeV}}$ and the easy handling, due to the only slight hygroscopic property, are furthermore good arguments for CsI(Tl). For the work discussed here the most important property are the two decay time constants $\tau_f = 600 \text{ ns}$ and $\tau_s = 3.25 \mu\text{s}$ in the scintillation light. There is also a rapid decay component $< 0.5 \text{ ns}$, that covers only a small fraction of the light output and is neglected thereafter. A table with a listing of those properties in comparison to other inorganic scintillators can be found in [34].

2.1.2 Scintillation properties

The exact scintillation process in CsI(Tl) is rather complex and even though CsI(Tl) is already in use as a scintillator since the 1950's [35], the mechanism it utilizes to produce the luminescence signal is still discussed. Inorganic scintillators have generally the property to produce Electron Hole Pairs or Excitons under irradiation with charged particles or γ radiation. In any of those cases, the hole can ionize an activator atom, that in turn captures an electron from the conduction band. The energy the electron carries, activates the former ionized atom, producing the scintillation light by the relaxation to the ground state [34]. More specific in the CsI(Tl) scintillator, Self Trapped Holes (STH) or V_k -centers play a central role in the production of the scintillation light [36]. If an I^- ion is perturbed by a neighboring Tl^+ ion, an electron from the I^- ions 5p orbital can be transferred to the Tl^+ vacant 6p orbital. This process creates a Tl^0 center and a hole in the valence band. This hole leads to the creation of a V_k center near the Tl^0 , a $\{\text{Tl}^0, V_k\}$ -pair. The 6p electron then is able to tunnel from Tl^0 to the V_k center due to their overlapping wave functions. This is called Fast Tunneling recombination. The resulting state is known as a Self Trapped Exciton (STE). The decay of the STE leads then to the visible scintillation light of CsI(Tl) [37]. The STE has a singlet state with a very short life time, and three triplet states having different life times each [38]. Due to the fixed life time of each of this states the decay of

the luminescence light $L(t)$ can be described by the sum of the exponential decays of each state:

$$L(t) = \sum_i \frac{N_i}{\tau_i} e^{-\frac{t}{\tau_i}} \quad (2.1)$$

The index i runs over all scintillation components, τ_i are the decay times of each component and N_i are the amplitudes of each scintillation process. The sum over the amplitudes N_i is proportional to the event energy E [39]. The whole scintillation process is strongly dependent on temperature. At room temperature a direct transition between the states is possible. The two dominant decay time constants result from the different composition of those excited states.

2.1.3 Particle identification with CsI(Tl)

When the scintillation properties of CsI(Tl) were first researched in the 1960's, it was found, that the scintillation characteristic depends on the ionization density, and hence is dependent on the particle type, making it possible to use CsI(Tl) for particle identification by the luminescence function $L(t)$ [35]. At room temperature, there are three dominant decay modes for STE described in section 2.1.2 [39]. Thus the luminescence function from equation 2.1 takes the following form [40]:

$$L(t) = \frac{N_f}{\tau_f - \tau_r} \cdot e^{-\frac{t}{\tau_f}} + \frac{N_s}{\tau_s - \tau_r} \cdot e^{-\frac{t}{\tau_s}} + \underbrace{\left(\frac{N_f}{\tau_f - \tau_r} + \frac{N_s}{\tau_s - \tau_r} \right)}_{\equiv \frac{N_r}{\tau_r}} \cdot e^{-\frac{t}{\tau_r}} \quad (2.2)$$

In the limit, that $\tau_r \ll \tau_s, \tau_f$ the formula can be simplified to:

$$L(t) = \frac{N_f}{\tau_f} \cdot e^{-\frac{t}{\tau_f}} + \frac{N_s}{\tau_s} \cdot e^{-\frac{t}{\tau_s}} \quad (2.3)$$

The decay times τ_s and τ_f describe the decay of the fast and slow scintillation component of CsI(Tl) with $\tau_f \approx 600$ ns and $\tau_s \approx 3.25$ μ s. The rapid component $\tau_r \approx 30$ ns can be neglected as instantaneous due to $\tau_r \ll \tau_s, \tau_f$.

As already mentioned before the scintillation characteristic of CsI(Tl) and thus the scintillation function, representing the scintillation characteristic in its multiple components (cf. equation 2.3) is depending on the ionization density / particle type. Being a material property, only dependent on the temperature and the compound mixture of CsI(Tl), the decay time constants τ_i cannot be responsible for the variation in the scintillation signal. That leaves only the amplitudes N_f and N_s to be influenced by the incident particle [35]. The mechanism due to which the energy loss process influences the ratio of the individual components in the scintillation light is not yet unanimously agreed upon. A possible model are thermally induced transitions between the triplet and singlet states [38].

Bottom line is, that it is imperative for the particle identification to separate the light amplitudes N_f and N_s out of the luminescence function. To achieve the separation a pulse shape analysis (psa) is performed as will be described in the following section.

2.2 Pulse shape analysis

The scintillation signal generated by the CsI(Tl) crystals is digitized using the FEBEX data acquisition system (DAQ) described in chapter 3.2.3. These readout cards contain an online PSA firmware developed by Max Winkel using the Quick Particle Identification (QPID) algorithm[41] for particle identification by separation of the amplitudes N_i of different decay time constants τ_i in the light output of scintillating particle detectors. The

individual algorithms necessary for the preparation of the raw trace signals created by the CsI(Tl) detectors are introduced in the following as well as the QPID algorithm.

2.2.1 Baseline reconstruction

Low frequency noise from the read out electronics leads to a baseline offset. Calculating a moving average before and after an event and subtracting this average from each trace value of the event is used for base line reconstruction. At low event rates, it is possible to recalculate this for each event. For this, not only the size of the averaging window is selectable in the algorithm, but also a window allowing time for the event, during which the baseline averaging is paused, is set. This window is at least several preamplifier decay times τ_{preamp} in length as not to miss the end of the event. For high event rates, the baseline reconstruction cannot be done for each event, but is instead the baseline is reconstructed at the beginning of the measurement once, under the assumption, that the variation of the baseline during the measurement is negligible.

2.2.2 Moving Averaging Unit

The Moving Averaging Unit (MAU) is used for smoothing any high frequency noise out of the raw trace. The algorithm works by moving a window of a specific length T in samples over the raw trace. Inside this window the amplitude A_i of each sample is summed over and divided by the window size.

$$m_{MAU} = \frac{1}{T} \sum_{i=0}^{T-1} A_i \quad (2.4)$$

For high frequency noise the average over a long enough amount of time is small so the moving average removes it nicely. It is taken care of the window size being not too long, which leads to unwanted alterations of the trace's shape.

2.2.3 Moving Window Deconvolution

The CsI(Tl) light signal is not directly usable for analysis, but is amplified using a charge sensitive preamplifier(cf. chapter 3.2.3). These preamplifiers have a decay time constant $\tau_{preamp} = 50 \mu\text{s}$. If another event occurs during this time, it overlaps with the exponential decay, and is then called a pileup. This pileup leads to an overestimation of the measured energy. The exponential decay of the preamplifier also leads to an effect called ballistic deficit. The continuous discharge of the capacitor in the preamplifier translates to an underestimation of the signal's amplitude. To counteract those two effects the Moving Window Deconvolution (MWD) algorithm is used. It removes the convolution the preamplifier enacts on the signal by moving a window with a fixed length L over the raw detector signal. The MWD follows for a signal convoluted with one exponential this equation[42]:

$$Q(t) = U(t) - U(t - L) + \frac{1}{\tau_{preamp}} \sum_{t'=t-L}^t U(t') \quad (2.5)$$

U is defined as the raw signal, Q the deconvoluted signal and L the MWD window size. Equation 2.5 integrates the whole charge inside the MWD window, thus correcting for the ballistic deficit. If the window just overlaps with the raw signal completely, all charge is collected. Beyond that point, the signal decays strongly (cf. figure 2.1). The red curve depicts a signal after the MWD. The rising edge of the signal represents the integrated charge function $Q(t)$, rising up until it reaches the MWD window size $t = L = 100 \mu\text{s}$. Then the signal decays steeply to 0. This means after the MWD, the signal's length is no longer

defined by preamplifier decay, but by the window size chosen in the MWD. However it has to be kept in mind, to choose L large enough to collect most of the charge, but still small enough to keep the signal short. For comparison, the raw signal, that the red MWD signal is based on, was also plotted in figure 2.1 (green curve). The ballistic deficit is removed and the faster decay of the MWD signal is shown, reducing the probability of a pileup to occur.

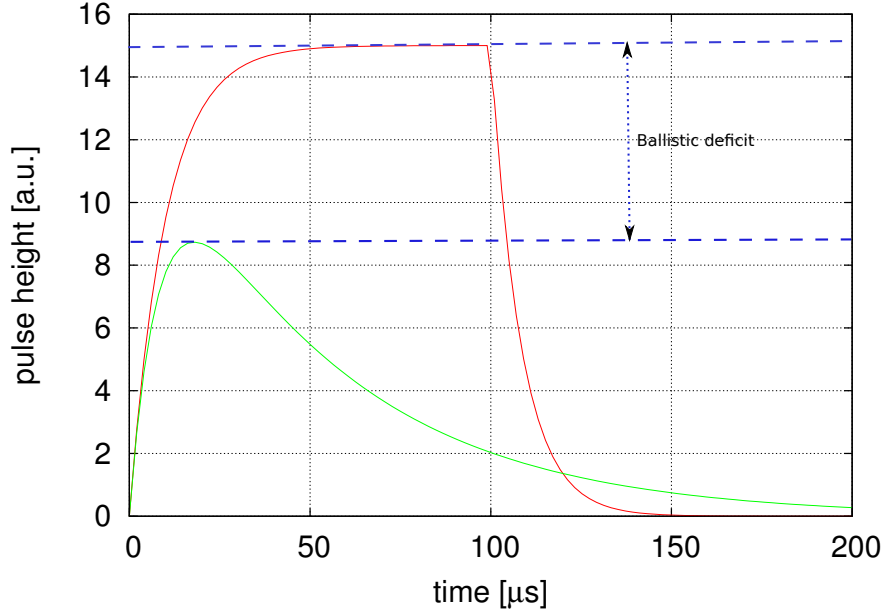


Figure 2.1: The figure shows the comparison between the raw signal after the preamplifier (green) and the signal after the MWD (red). As can be seen, the ballistic deficit (blue) has been corrected in the MWD signal. Also the MWD signal decays faster than the raw signal, reducing pileup effects. As MWD window size $L = 100 \mu\text{s}$ was chosen.

For figure 2.1 arbitrary functions were used for easier plotting. A detailed calculation for CsI and the used preamplifier is described in [41].

2.2.4 Quick Particle Identification

As described in chapter 2.1.3, the separation of the scintillation light into the fast light component N_f and the slow light component N_s of CsI(Tl) can be used for particle identification. An established method for separation is integration of the photo current within two time windows, one directly after triggering and a second delayed one. The windows length and positions are chosen such that the charge contained within the first window Q_f is dominated by N_f and the charge contained within the second window Q_s is dominated by N_s . The QPID algorithm was developed based upon this paradigm by Max Winkel [41]. The output signal of the MWD as described in chapter 2.2.3 is already the integrated charge signal, which is described by the following functions.

$$F_1(t) = \frac{1}{T} \int_0^t Q(t') dt' = \frac{N_f}{T} \left(t + \tau_f \left(e^{-\frac{t}{\tau_f}} - 1 \right) \right) + \frac{N_s}{T} \left(t + \tau_s \left(e^{-\frac{t}{\tau_s}} - 1 \right) \right) \quad (2.6)$$

$$F_2(t) = \frac{1}{T} \int_{t-T}^t Q(t') dt' = N_f \left(1 - \frac{\tau_f}{T} \left(e^{\frac{T}{\tau_f}} - 1 \right) e^{-\frac{t}{\tau_f}} \right) - N_s \left(\frac{\tau_s}{T} \left(e^{\frac{T}{\tau_s}} - 1 \right) e^{-\frac{t}{\tau_s}} \right) \quad (2.7)$$

$Q(t)$ describes the integrated charge within the window $[0,t]$ and T the window size of the MAU filter. The shaped and deconvoluted charge function $F(t)$ is divided into two integrals defined by the windows $[t_0,t_1]$ and $[t_2,t_3]$ as illustrated in figure 2.2.

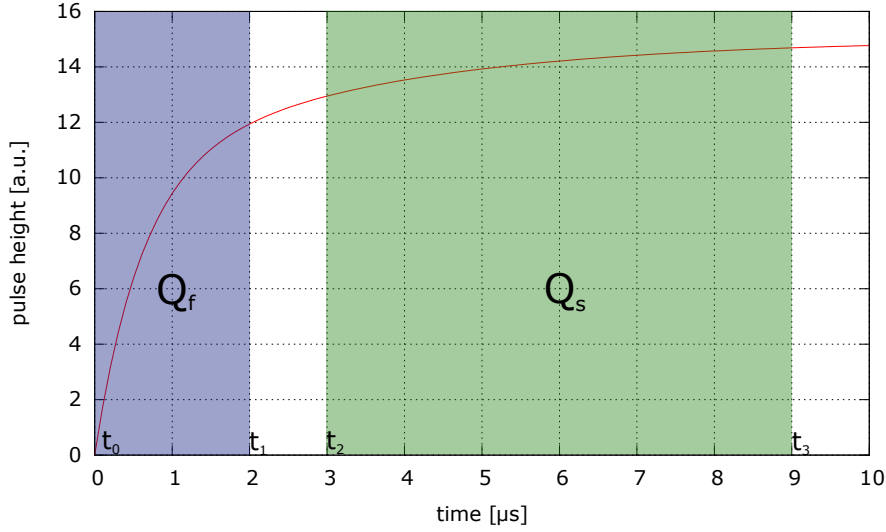


Figure 2.2: The figure shows a calculated charge function $Q(t)$ with arbitrary ratio of the light components N_f and N_s and the corresponding windows for Q_f (blue) and Q_s (green). The values for t_0 to t_3 are selected based on [40].

Calculation of the charges Q_f and Q_s together with their relation to the light components N_f and N_s created a linear system of equations that can be represented using a matrix as shown in the following equation.

$$\begin{pmatrix} Q_f \\ Q_s \end{pmatrix} = \begin{pmatrix} F(t_1) - F(t_0) \\ F(t_3) - F(t_2) \end{pmatrix} = \begin{pmatrix} A & B \\ C & D \end{pmatrix} \begin{pmatrix} N_f \\ N_s \end{pmatrix} \quad (2.8)$$

whereas A, B, C and D only depend on the window size T and chosen t_0 to t_3 . By inverting the matrix the equation is solvable for the light amplitudes N_f and N_s .

$$\begin{pmatrix} N_f \\ N_s \end{pmatrix} = \frac{1}{AD - BC} \begin{pmatrix} D & -B \\ -C & A \end{pmatrix} \begin{pmatrix} Q_f \\ Q_s \end{pmatrix} \quad (2.9)$$

To optimize this equation, the t_i can be adjusted that the calculated N_f/N_s no longer contain contributions of Q_s/Q_f , or in other words, $A, D = 1$ and $B, C = 0$. A discussion on the optimum values can be found in [40].

Figure 2.3 shows a typical PID plot with values of the light amplitude N_f and N_s calculated using the QPID algorithm from experiment data taken at the TRIUMF facility[43] of neutrons impinging on a CsI(Tl) crystal.

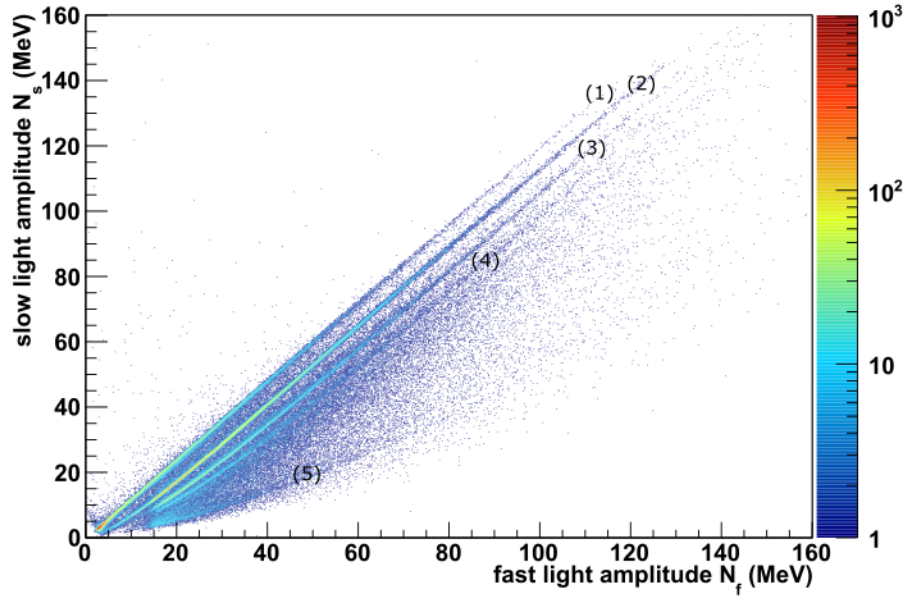


Figure 2.3: An example of a QPID plot with neutrons irradiating a CsI(Tl) crystal. A total of 5 branches is visible in the plot. (1) the γ and punch through proton branch, (2) the proton branch, (3) the deuteron branch, (4) the triton branch and (5) a branch with helium nuclei.

The neutrons themselves are not directly detected, but their reaction products e.g. from nuclear reactions with Cesium or Iodine nuclei within the detector material. This results in the abundance of particle species observed in the PID plot (fig. 2.3). These reaction products are represented by different branches created by the unique N_f/N_s ratio of each particle species. A total of five branches can be separated corresponding to different particles. Branch (1) corresponds to γ -rays and punch through of light charged particles (lcp). (2) shows low energy protons stopped in the detector. In branch (3) deuterons are also identified, while in branch (4) tritons are found. In addition a weak branch (5) probably containing helium nuclei events is visible in the QPID plot. To increase the visibility of the separation power, especially in the region below 10 MeV, of the PID in CsI(Tl) a different representation of this plot is chosen. Rotating the diagonal branches onto the x-axis by using the polar rotation operation as described in the following equation:

$$\begin{pmatrix} N_{f,red} \\ N_{s,red} \end{pmatrix} = \begin{pmatrix} \cos \alpha & -\sin \alpha \\ \sin \alpha & \cos \alpha \end{pmatrix} \cdot \begin{pmatrix} N_f \\ N_s \end{pmatrix} \quad (2.10)$$

with $\alpha = \arctan m$ and m as the slope of diagonal with the smallest N_f/N_s ratio. Applying the rotation to the PID plot results in figure 2.4.

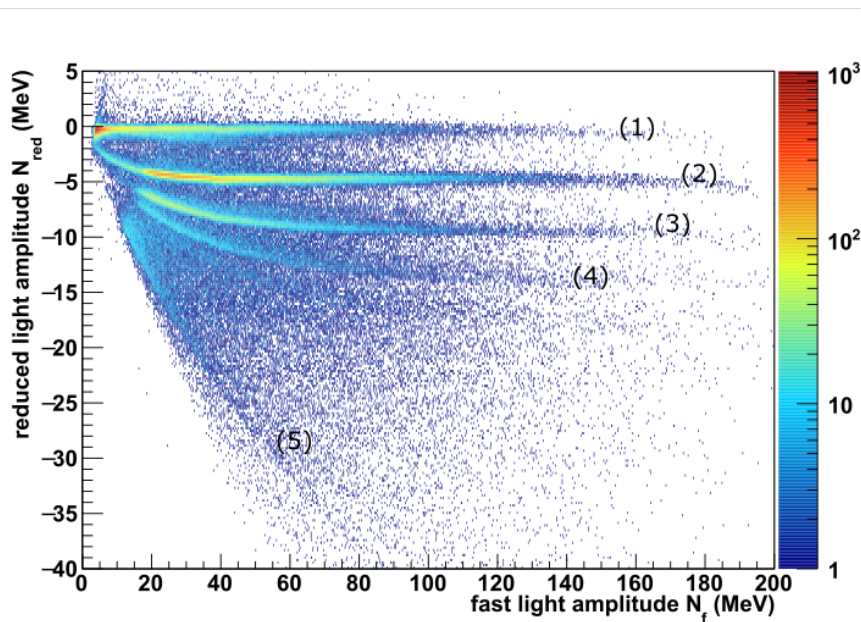


Figure 2.4: An example of a reduced QPID plot with neutrons irradiating a CsI(Tl) crystal by rotating the standard plot (cf. figure 2.3) onto the x-axis. The separation of the 5 branches is now much better represented. The branches are labeled the same as in the standard representation: (1) the γ and punch through proton branch, (2) the proton branch, (3) the deuteron branch, (4) the triton branch and (5) a branch with helium nuclei.

The advantage of the reduced representation is an increased optical separation of the five branches making it easier to interpret the plot and identify the separate isotope branches. The reduced representation is used for the continued analysis in this thesis.

Chapter 3

Krakow experiment

For a systematic test of the existing and future petal demonstrator detectors the Cyclotron Center Bronowice of the Henryk Niewodniczański Institute of Nuclear Physics of the Polish Academy of Sciences in Krakow was chosen. The facility features a proton cyclotron of type “Proteus C-235” which can be used for material science, medical and nuclear physics purposes as well as for radio-therapy of cancer patients. As the accelerator facility is designed for medical application, the beam energy can be changed quickly within a range of $70 \text{ MeV} < E_{\text{Beam}} < 230 \text{ MeV}$. This is due to a degrader wheel which introduces the proper material and thickness to precisely downscale the primary beam energy of the cyclotron. To compensate for the energy loss straggling in the degrader material an additional magnetic energy filter is also adjusted to the chosen beam energy guaranteeing a beam resolution $\Delta E_{\text{Beam}} < 0.7 \%$ (FWHM). This beam is shared by two experimental halls, two rotating gantrys and an separate eye cancer treatment facility. Drawback of the medical use of the facility is a limitation in the available beam intensity in a range of $1 \text{ nA} < I_{\text{Beam}} < 600 \text{ nA}$. As we did not irradiate the detectors directly but on a target

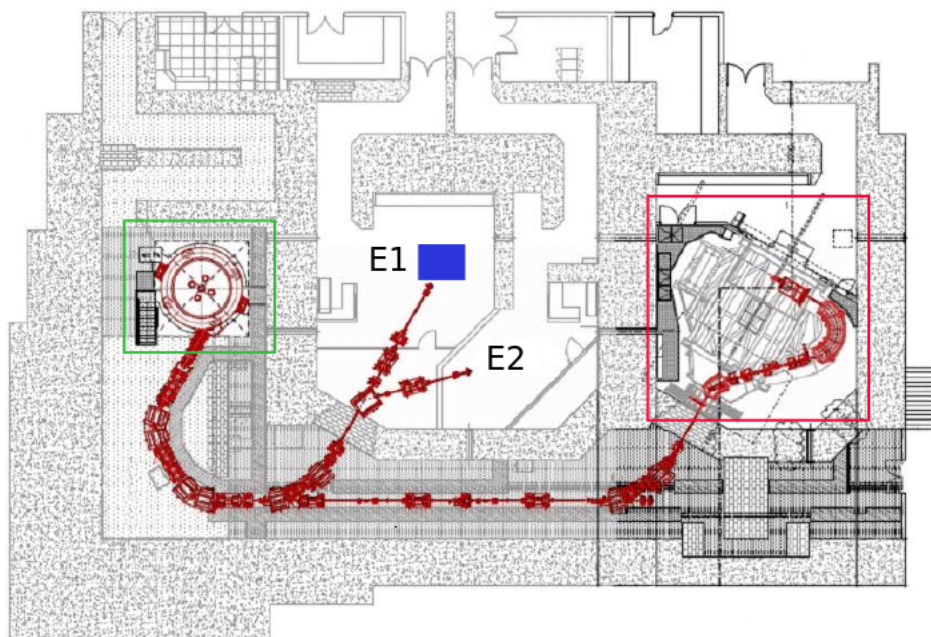


Figure 3.1: Overview of the Bronowice Cyclotron Center. In green the Proteus C-235 cyclotron is visible, as are the beamlines leading to the different medical and experiment sites. The gantry setup (red) with a revolving beam line is used for medical applications and two experimental halls (E1 and E2) are available for physics experiments. The location within hall E1 used for the experiment is indicated in blue[44].

only detecting secondary particles, the available intensities are more than sufficient for the proposed test experiment. In addition the detectors are not designed for withstanding

rates much higher than 1 kHz due to the already mentioned slow scintillation response of the CsI(Tl) used in the petals. This chapter contains next to the detector and experiment setup also details on the used electronics and target. Results from the experiment are presented in the next chapter. An important decision concerning every experiment is choosing a suitable target nucleus or compound. As in this case the experiment's main goal is to evaluate the CALIFA demonstrator performance, a well known system needs to be chosen, as comparable results for detection efficiency and cross sections should be available. The following illustrates the reasons for choosing an ^{16}O target.

3.1 Excitation of ^{15}N

Excited states of nuclei with closed shells (such as ^{16}O) lying close to the Fermi surface exhibit single particle behavior[45]. The shell model description assumes a mean field approach, where the single particle moves through an average potential generated by the rest of the nuclei. Considering the ground state configuration of the target nucleus ^{16}O (cf. figure 3.2) with neutron and proton shells filled up to the $1p_{1/2}$ shell (doubly magic $N = Z = 8$). The beam proton knocks out one proton from either of the $l=1$ orbits shells, leaving the residual ^{15}N nucleus excited ($1p_{3/2}$ knock-out) or in the ground state ($1p_{1/2}$ knock-out). Figure 3.3 illustrates a level scheme of ^{15}N reduced to the here relevant transitions below

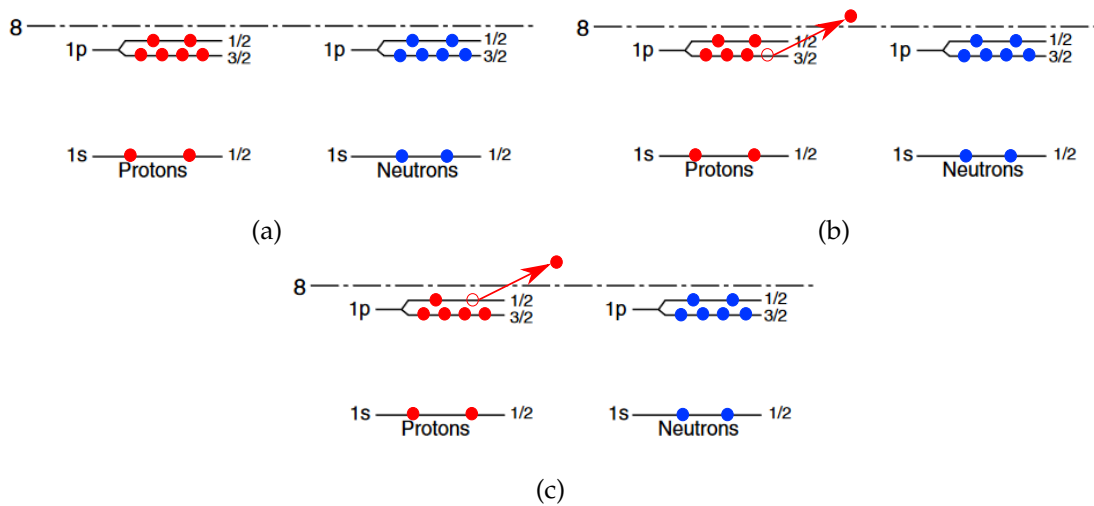


Figure 3.2: A figure illustrating shell model configuration of the ^{16}O target before the $(p,2p)$ reaction and residual ^{15}N afterwards[34]. In figure a) the ^{16}O target nucleus configuration before the reaction with its closed proton and neutron shells (double magic) is shown. After the knockout of one proton from the $1p_{3/2}$ shell the residual ^{15}N is left in an excited state (figure (b)). The removal of a $1p_{1/2}$ shell proton results in the ground state of ^{15}N as shown in figure c).

the separation energies $S_n = 10.83 \text{ MeV}$ and $S_p = 10.21 \text{ MeV}$ [46]. Populating the positive parity states $2s_{1/2}$ and $1d_{5/2}$ directly is due to the spin conservation, as the outgoing proton needs to carry away the necessary spin for a spin flip of the residual nucleus. This leaves the negative parity states to be populated. The residual can on one hand directly be in the ground state ($1/2^-$) or in the first excited state ($3/2^-$) being fragmented into four states. Strongest of the four is at the same time the energetically lowest one at 6324 keV and far weaker ones at 9925 keV, 10702 keV and 12920 keV created by couplings of particle-hole states with the continuum states at the Fermi surface and can so even occupy states above the separation energy. It is worth to notice that the 6324 keV state deexcites with 100% probability directly to the ground state, making it a perfect source for high energy γ -rays.

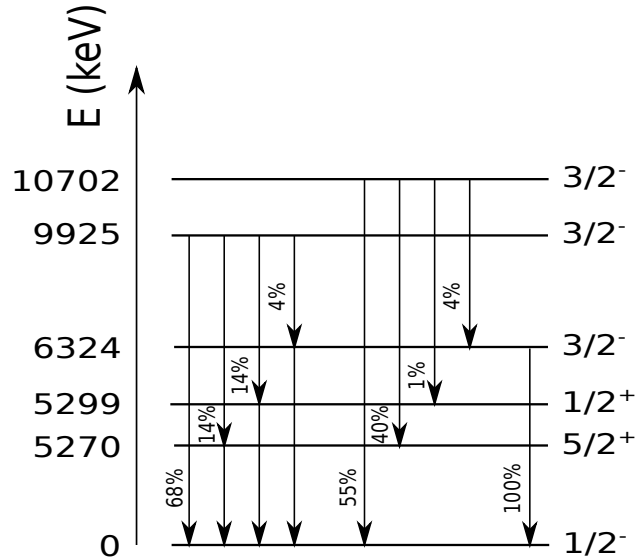


Figure 3.3: Level scheme of ^{15}N reduced to emission radiation created by excitation of ^{15}N from $1p_{3/2}$ shell proton knockout using data taken from [46]. The three relevant $3/2^-$ states with 6324 keV, 9925 keV and 10702 keV level energy cascade with the indicated branching ratios to the ground state. Note that the 6324 keV level decays only decays directly to the ground state, while the other two lines populate three intermediate states as well.

A detailed spectrum of the excitation energy from the ^{15}N nucleus is shown in figure 3.4. These figures were created by a 392 MeV proton beam impinging on a $\text{H}_2\text{O}(\text{s})$ target

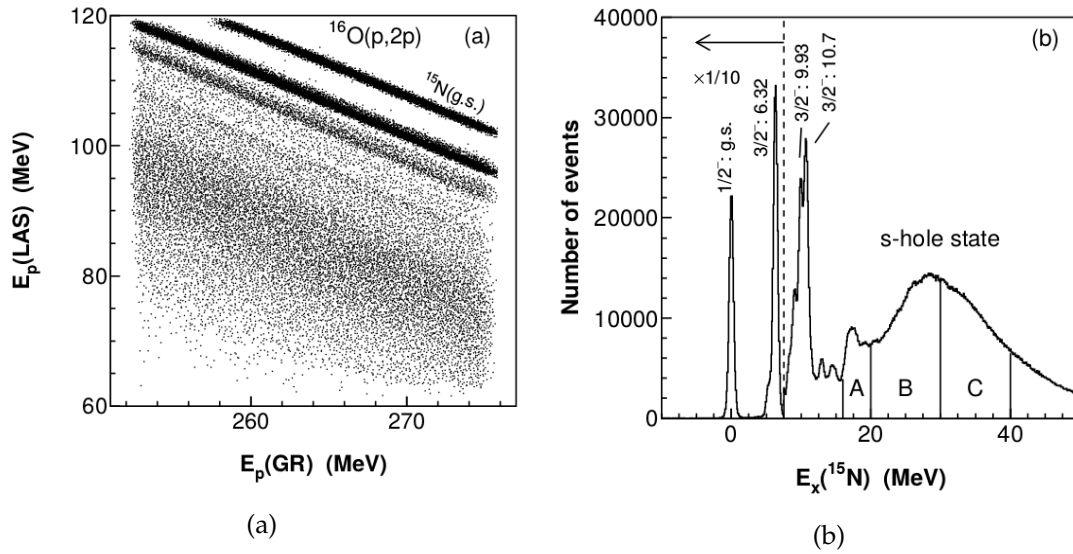


Figure 3.4: Excitation energy spectra of ^{15}N resulting from $^{16}\text{O}(p,2p)^{15}\text{N}$ in direct kinematics ($E_{\text{beam}} = 392$ MeV) measured with a two-arm spectrometer in Osaka, Japan [47]. Figure a) shows the correlation of the energy detected in both arms (GR and LAS). The ground state and two excited states of ^{15}N are observed as sharp correlation bands. Towards lower energies a broad distribution is observed. Figure b) shows the reconstructed excitation energy E_x is shown, where the ground state and three excited states with 6.32 MeV, 9.93 MeV and 10.7 MeV are observed as well as higher excitations (s-hole states). Note, that the intensity of the ground and 6.32 MeV excited state are attenuated by a factor of 10.

($^{16}\text{O}(p,2p)^{15}\text{N}$) and measured with a two-arm spectrometer at 25.5° (GR) and 51° (LAS)[47]. In figure 3.4 a) an anti correlation between the measured proton energies is visible and

the lines corresponding to the different states of ^{15}N are separated nicely. The calculated excitation energy is shown in figure 3.4 b). Ground State and 6.3 MeV lines are well separated as expected from the 2D plot in a). Note that these two lines are attenuated by a factor of 10 compared to the rest, indicating the already mentioned decrease in population of the higher excited states by this reaction. The 9.93 MeV and 10.7 MeV lines are visible as well, but the separation is lacking. Towards higher excitation energies the spectrum is dominated by a broad distribution, originating from s-hole transitions. As these are extending higher than the separation energies S_n and S_p the emission of a nucleon to deexcite becomes likely. In this experiment the ground state and 6.3 MeV excited state were used to benchmark the separation and reconstruction power of CALIFA for excitation energies in (p,2p) reactions. In addition the de-excitation of the 6.3 MeV state with only one γ -ray enables the study of absolute γ -ray efficiencies and a measurement of these γ -ray under realistic circumstances making this experiment the ideal test case for each and every CALIFA Demonstrator petal.

3.2 Experiment Setup

As the target material was fixed, several parts of the experiment setup were decided on. Building a suitable target containing ^{16}O and choosing the proper beam parameters for the setup is discussed in the first part of the following section. The second part discusses the demonstrator and tracking detectors as well as their alignment around the target and a short introduction of the data acquisition (DAQ) used in the experiment.

3.2.1 Beam and Target

For the analysis in this thesis two different target materials and geometries were used. A solid polypropylene (C_2H_4) target with $d_{\text{PP}} = 500 \mu\text{m}$ was used mainly for calibration of the CsI(Tl) detectors and general DAQ and setup tests using elastic scattered protons off the hydrogen nuclei ($^1\text{H}(p, p')^1\text{H}$). As the main target a liquid water (H_2O) fiber target with diameter $d_{\text{H}_2\text{O}} = 460 \mu\text{m}$ was used. This provides on one hand a method of creating a stable, highly localized oxygen target to investigate the $^{16}\text{O}(p, 2p)^{15}\text{N}$ reaction (cf. section 1.2.3) and on the other hand delivers through the hydrogen nuclei an intrinsic calibration capability for cross checking with the polypropylene target.

For switching targets, a universal target mount was desired. This mounting is precise, compact, easy to assemble and disassemble, and light weight. First step in design of this universal mount was to think on how to operate a liquid water target. A schematic sketch is shown in figure 3.5. To create the water fiber a medical cannula with the desired diameter (here $d = 460 \mu\text{m}$) was used. The cannula was connected by a so called Luer Lock connector to other medical equipment like tubing or syringes, which made them the first choice in constructing the water circuitry. The collection vessel was connected by a short rubber tube to a small pump. This kind of pump was designed to deliver a continuously high pressure even at a low throughput needed due to the small diameter of the cannula. Adjusting the pump's pressure is a matter of regulating it's supply voltage. After the pump the medical tubing provides a flexible way of delivering the water up to the cannula as it is available in various lengths. To prevent the water fiber to become unstable due to pressure variations from the pump, the cannula is not directly connected to the medical tubing but is connected to a three way switch with an additional 40 ccm syringe used as compensating volume. In addition a pressure gauge is used to seal the syringe for pressure monitoring. In the next step a mounting structure based on this design was developed, where the position of either the water jet or a solid target could be chosen and adjusted with high precision. As the available space at the target position was

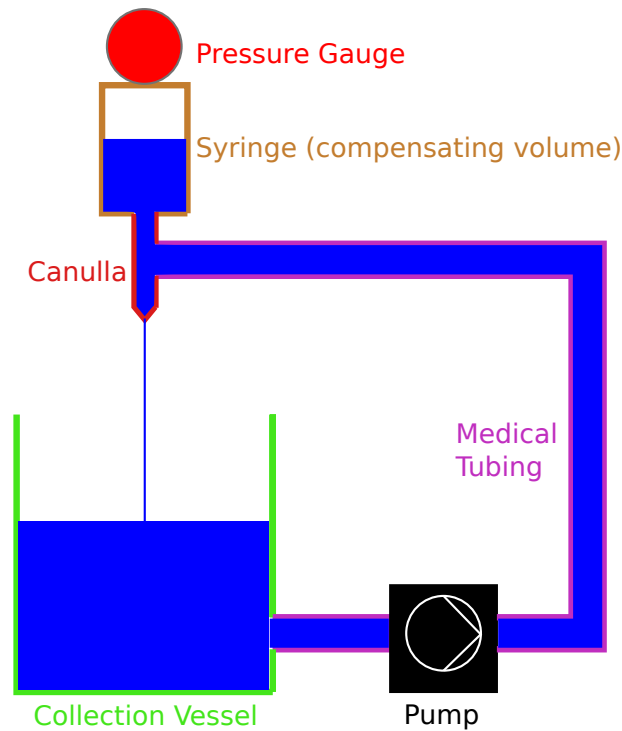


Figure 3.5: Schematic drawing of the water target. A **medical cannula** is used to create a thin water fiber. This water is collected in a **collection vessel** from which a pump is transporting the water through **medical tubing** to the cannula again. To ensure a constant water pressure a **syringe** with a **pressure gauge** is used as a compensating volume.

not precisely known, a modular approach was chosen in this case. Using several steel rods with 10 mm diameter and attached meters (precision 0.5 mm), and aluminum connector modules, a crane-like target mount was created (cf. figure 3.6). Each of the connector modules was equipped with a meter window enabling adjustments with 0.5 mm precision. Each rod is fixed into position by two screws. The figure also illustrates the two options for mounting the target either from any side or above depending on the space available. Additionally the beam profile was recorded in order to gain information on vertex accuracy. Due to the limited tracking capabilities of the setup, a photo-analytic approach by recording the beam profile on a radio-sensitive film was used. The beam spot size could be adapted in size by a set of horizontal and vertical slits moved into the beam path from the outside. As these slits were far away from the target position, reactions from them is not observed. Figure 3.7 shows a photograph of one of these radio-sensitive films irradiated with two different beam settings. The upper spot corresponds to the default 6 mm x 5 mm slit setting supplied by the facility. A homogeneous distribution was visible, although due to saturation of the film, a more sophisticated distribution cannot be distinguished. Towards the edges of the beam spot the coloring fades abruptly away, giving the impression of a sharp cut-off. Measuring the spot size gives the following values: $dx = (6.5 \pm 0.1)$ mm, $dy = (5.3 \pm 0.1)$ mm. To achieve the lower beam spot, a 3 mm x 3 mm slit configuration was chosen. Note, that the beam spot is cut asymmetric with a slight fringing towards the right side as a side effect. This effect was disregarded, as the water target jet was well located in x-direction by its small diameter. Through this small setting, the target's dimensions in the y-direction is limited. Measuring this spot size gives following values: $dx = (3.0 \pm 0.1)$ mm, $dy = (2.8 \pm 0.1)$ mm. This limits the accuracy of the vertex position to $\sigma_{beam,x} = (500 \pm 5)$ μm and $\sigma_{beam,y} = (2.8 \pm 0.1)$ mm, where a manufacturing tolerance of the cannula of 1% was assumed.

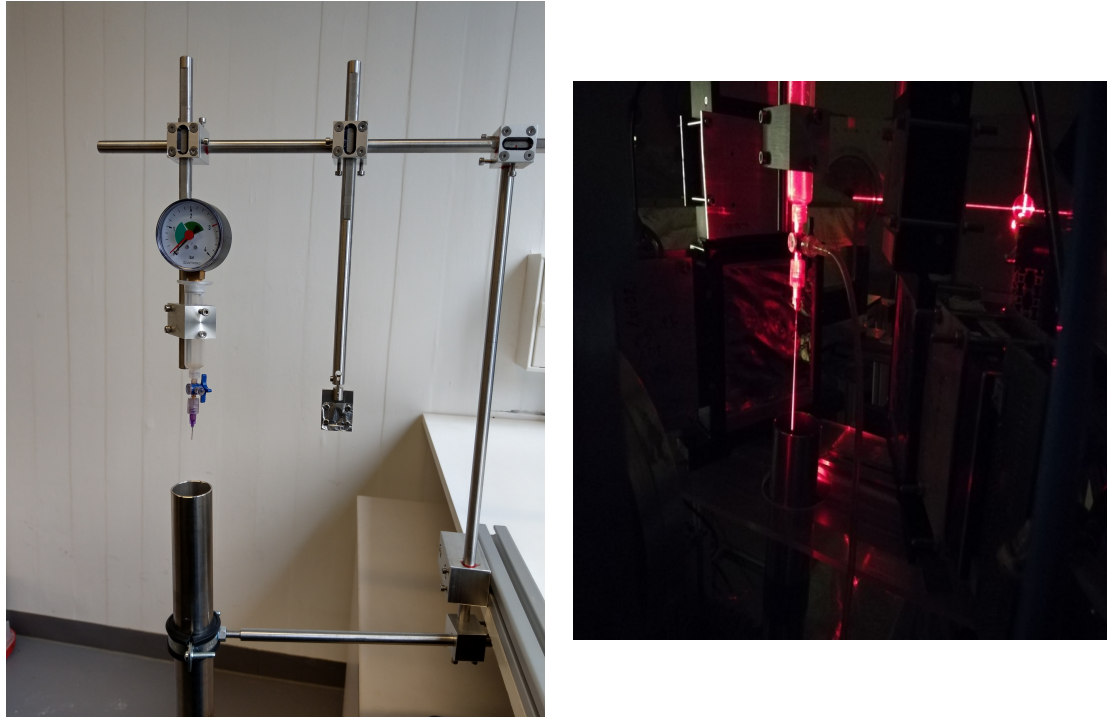


Figure 3.6: Picture of the target mount mechanics. Figure a) shows the crane like universal mounting structure with the water target mount (schematic cf. figure 3.5) on the left and a solid state target mount on the right. Below the water target mount the collection vessel is visible. To adjust the position on the target, high precision measures are visible at the top with an accuracy of 0.5 mm. Figure b) shows the 0.46 mm water jet illuminated by a laser beam.

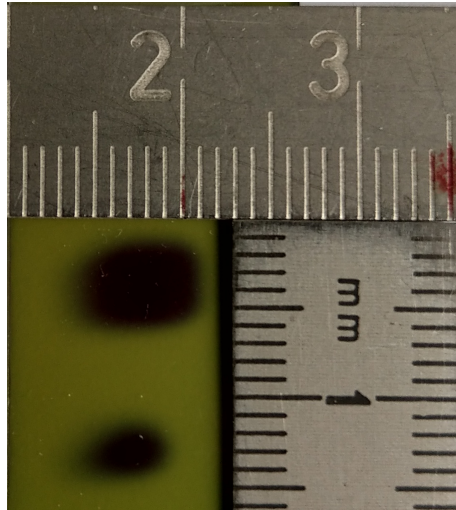


Figure 3.7: Beam profile recorded on radio-sensitive film. Upper spot represents the default 6 mm x 5 mm slit setting (measures: $dx = (6.5 \pm 0.1)$ mm, $dy = (5.3 \pm 0.1)$ mm) while the lower spot represents a 5 mm x 2 mm slit setting (measures: $dx = (3.0 \pm 0.1)$ mm, $dy = (2.8 \pm 0.1)$ mm). The lower one was used for the water target.

3.2.2 Detectors

The experiment consisted mainly of three so called Petal demonstrator detector units. These Petals are part of the final CALIFA detector and represent subunits of the forward half of the Barrel part. Made up of 64 CsI(Tl) crystals, which in crystal type and size correspond to 4 rows of 16 detectors covering a polar angle range of $43^\circ \leq \Theta \leq 93^\circ$ (see

figure 3.8). All crystals are four-sided asymmetric truncated pyramids with differing length. The most forward 6 detectors have a length $z = 22$ cm, the next 6 are $z = 18$ cm long and the last 4 have $z = 17$ cm. All of these crystals are individually wrapped in a single layer of highly reflective VM 2000 foil with a thickness of $65 \mu\text{m}$ and a reflectivity $R \geq 98\%$ for visible light. For mechanical stability 4 crystal are collected in so called Alveolus bringing one Petal to a total of 16 Alveoli (cf. figure 3.8). To minimize the material budget each Alveolus consists of Carbon fiber with a wall thickness of just $250 \mu\text{m}$ minimizing the interaction probability for particles and γ -rays in this dead layer tremendously. For readout each of the crystals is equipped with a Hamamatsu S8664-1020 LAAPD [48] with a capacitance of $C = 2 \times 300 \text{ pF}$. The scintillation light is collected on an active area of 2 times 10 mm by 10 mm . Two of the three petals used were manufactured at the Lund University and the third one at the TU Darmstadt. Aim of the experiment was a detailed test of the performance of the petals, as well as showing CALIFAs capabilities in a first real test experiment. In addition to the three Petal units, also two double sided silicon

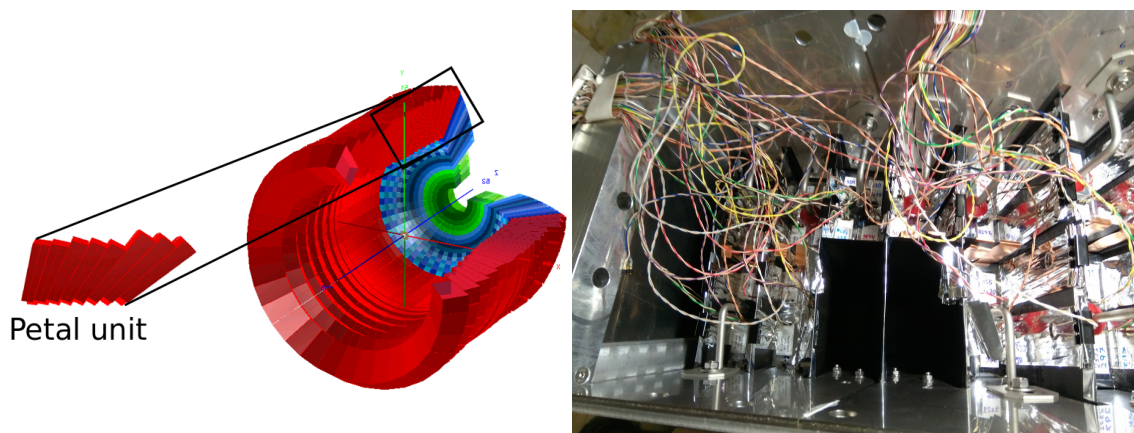


Figure 3.8: Overview over the Petal demonstrator unit. Left a schematic overview of the CALIFA Calorimeter with a Petal unit cut out of the full calorimeter. One unit represents 64 crystals of the forward part of the Barrel (red). Right side shows the interior of a Petal unit. The silvery wrapped crystals with the LAAPDs (white squares) mounted on top are clearly visible with their individual connection to a flat ribbon cable and packed into units of four crystals per Carbon fiber Alveolus. In the middle two empty alveoli are also visible.

strip detectors (DSSSDs) were used in the experiment supplied by Lund University. Each of the DSSSDs has a size of $60 \text{ mm} \times 60 \text{ mm}$ with an active area of $58 \text{ mm} \times 58 \text{ mm}$. Both sides were divided in 32 strips in x and y direction respectively leading to a strip pitch of 1.81 mm on both sides. The wafers total thickness is $300 \mu\text{m}$. More detailed description to these detectors is available in LYCCA-TDR ([49]). Each detector was housed in aluminum box with $20 \mu\text{m}$ mylar windows at the front and back of the box. Figure 3.9 shows one of the silicon in its aluminum box, with the preamplifier used for the front and back sides connected (left). On the right side, the isolated PCB mounted detector is shown, where the individual strips are visible quite nicely.

3.2.3 Electronics and Data Acquisition

For the spectroscopic readout of the CALIFA detector array a specially developed electronics is used. The first step in the electronics chain was the preamplification of the detector signals. For the Petals, the charge sensitive preamplifier MPRB-32¹, which was specifically designed for CALIFA and CsI(Tl)/LAAPD readout(cf. figure 3.10a). It features two individual preamplifiers with 16 channels each, integrated HV supply to the LAAPDs,

¹Mesytec MPRB-32 cf. <https://www.mesytec.com/products/datasheets/MPRB-16.pdf>

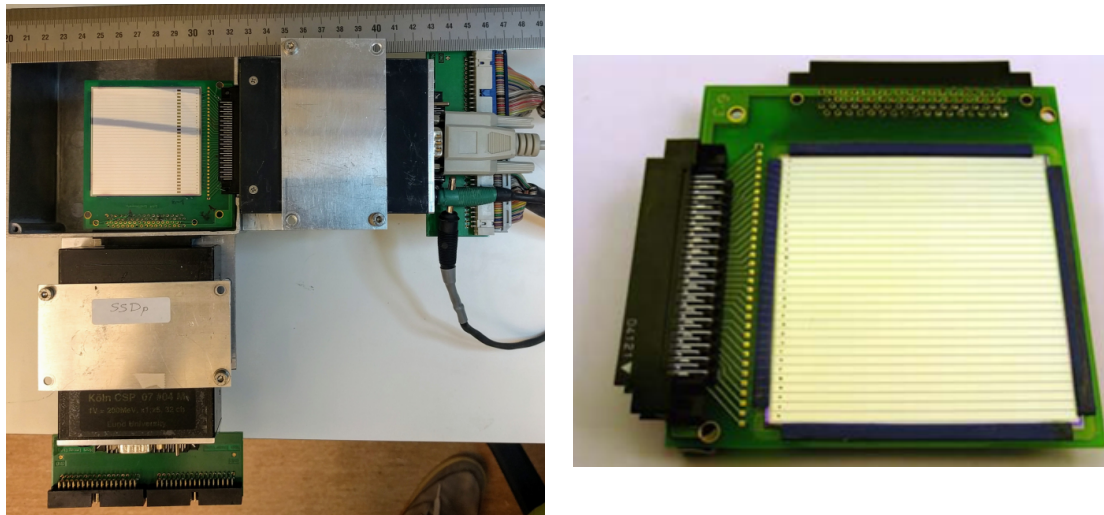


Figure 3.9: Overview of the DSSSD detector. On the left side the full detector is shown, with the detector mounted on the back plate of the aluminum housing already connected to the 32 channel preamplifiers. The front cover was removed here. On the right the DSSSD is shown mounted onto a PCB with readout connectors for preamplifier. The individual strips on the front side are clearly visible here.

temperature dependent gain compensation for LAAPD, switchable gain stages (30 MeV and 300 MeV) and many other useful commodities.

In case of the silicon detectors charge sensitive preamplifiers custom made by GSI were used. These provide 32 channels each with switchable gain by a factor of five to achieve a range up to 50 MeV and a decay time $\tau_{decay} = 15 \mu\text{s}$ [50]. As the expected energy loss for a proton with $E_p = 100 \text{ MeV}$ in silicon with a thickness of $300 \mu\text{m}$ is $E_{loss} = 0.407 \text{ MeV}^2$ the 10 MeV range is used.

The output of both preamplifiers is differential to prevent noise pickup from the signal being transferred to the next stage in the data acquisition. The analogue and preamplified detector signal was digitized by the FEBEX3B board developed by GSI[51]. The FEBEX3B board features two 50 MHz sampling ADCs and a Lattice LFE3-150 FPGA for the usage of custom online analysis firmware. For the in total available 16 readout channels per board, the ADCs supply a 14-bit resolution with a input range $-1 \text{ V} < U_{signal} < 1 \text{ V}$. In addition an FEBEX Add-on Board (FAB) with Nyquist filtering and baseline adjustment features was attached to the FEBEX3Bs add-on connector. More detailed information on the FAB and the online analysis firmware can be found in the thesis of Max Winkel([41]) and a short summary in chapter 2.2. Figure 3.10b shows the electronics necessary to read out the 320 detector channels of silicon and CsI(Tl) detectors using FEBEX and the Multi Branch System(MBS)[52]. A total of 20 FEBEX3b cards with FAB boards were used, separated in two FEBEX crates each with a separate fiber readout and trigger bus. The challenge here was the synchronous readout of two crates for the first time under experiment circumstances with different detector types. Online results of the readout are illustrated in figures 3.11 and 3.12. These show raw signal traces of first measurements with $E_{beam} = 200 \text{ MeV}$ on a polypropylene target. Looking at the x-axis the time samples of 40 ns show, that the sampling frequency $f = 50 \text{ MHz}$ was decimated by a factor of two. The resulting sampling is still sufficient for the slow signals of the charge integrating preamplifiers, but saves FPGA resources, which in turn are used to increase the number of effective bits. This decimation is not used for triggering to have a precise as possible timing. On the y-axis the pulse height in arbitrary units is shown. In figure 3.11 traces of a p-side strip of

²Calculated with Lise++

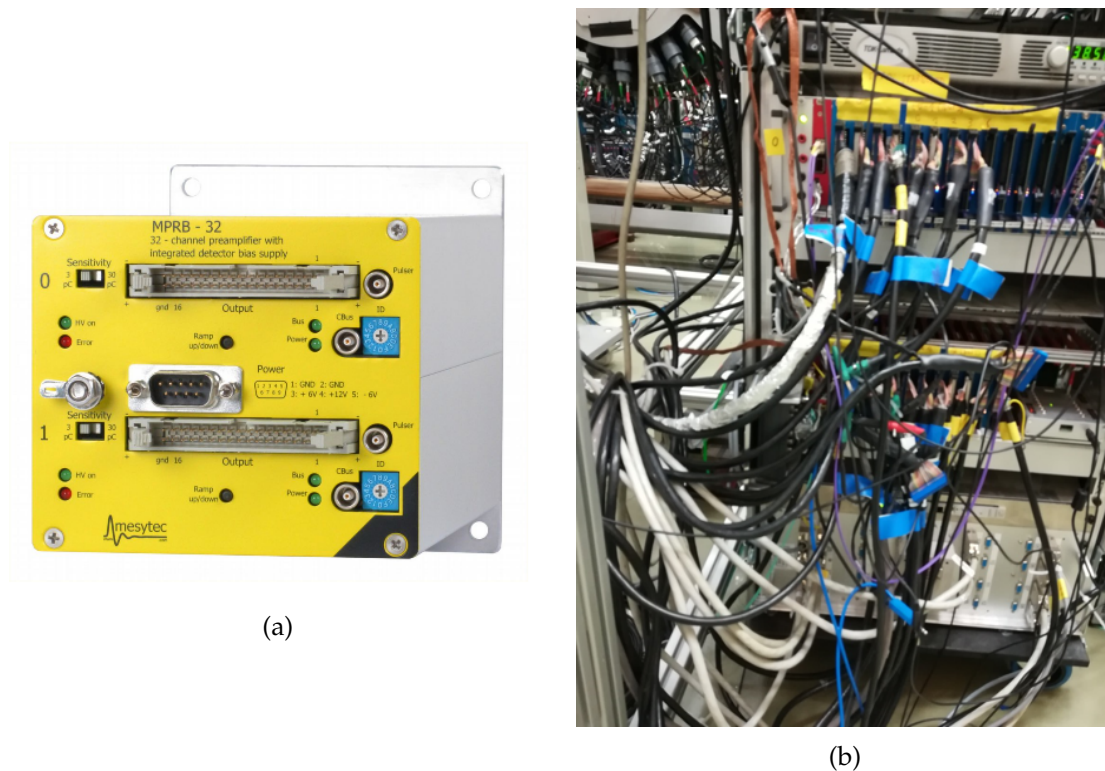


Figure 3.10: Figure a) shows the MPRB-32 preamplifier specifically designed for the readout of the CsI(Tl) detectors. It contains two independent 16 channel preamplifier modules with a common power supply and individual pulser and slow control connectors. In figure b) the rack containing 20 FEBEX3 digitizer cards complete with FAB boards to read out the total 320 detector channels. The cards are separated in two FEBEX crates for power supply, trigger bus and fiber readout.

one silicon detector are plotted. The characteristic fast rising edge of the silicon signal is clearly visible, as is the preamplifier's exponential decay $\tau=15\ \mu\text{s}$. In figure 3.12 traces of one CsI(Tl) detector are plotted. These traces show the characteristic slow rising edge of the CsI(Tl) scintillator as well as the preamplifier's decay $\tau=35\ \mu\text{s}$. The rise time of silicon and CsI(Tl) signal are significantly different as figures 3.11 and 3.12 show. This created an additional challenge for the readout firmware to handle in terms of energy measurement and trigger setup. Through proper adjustment of digital parameters of the signal analysis in the FPGA for the silicon readout channels a proper energy measurement was achieved. Using the standard single event trigger mode, where each trigger initiates a full readout of all ADC modules, severely restricts the event rate manageable by the setup. Due to this restriction, the trigger condition needs to be optimized to the desired particle signature. In case of the QFS reaction, the ideal trigger condition would be a coincidence of two protons in opposite detector arms. To cover all event channels a "single proton" trigger condition was used. The condition was set as a 10 MeV trigger threshold in the Lund petals used for proton detection. This way each energy deposition above 10 MeV in one of the petals initiates the readout of the whole setup to retain all coincident particles such as the second proton and excitation γ -rays in the case of a QFS reaction.

3.2.4 Setup

Testing the CALIFA petals for γ -ray and proton detection capabilities in unison with a quasi-free scattering reaction, the kinematics (see kinematic simulations in chapter 1.2.3)

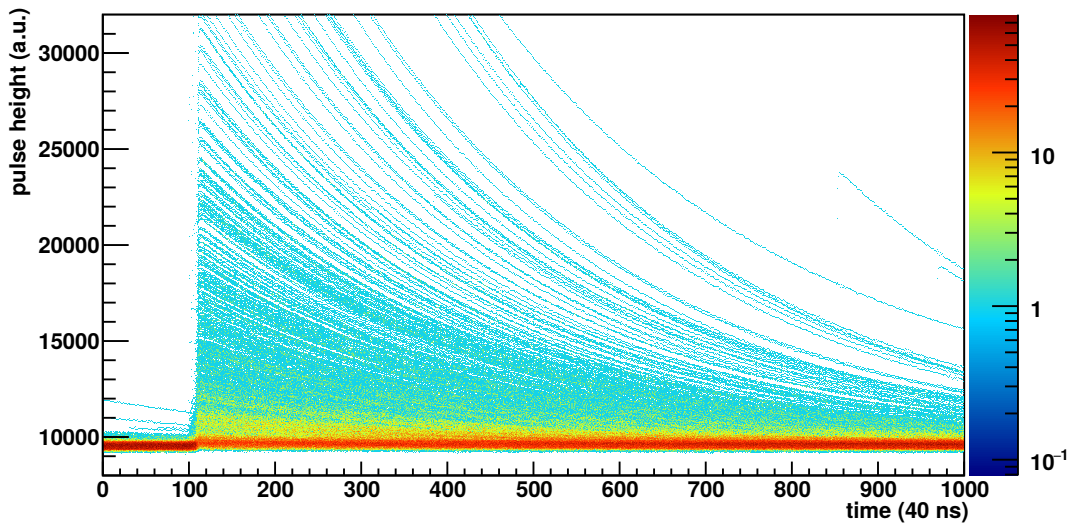


Figure 3.11: Raw signal traces of one strip of a silicon detector sampled with the FEBEX3 ADC at 50 MHz decimated by a factor of 2. On the y-axis the pulse height in arbitrary units is plotted versus the time in 40 ns samples on the x-axis. The characteristic fast rising edge of the silicon signal is clearly visible. The data was taken with $E_{\text{beam}} = 200$ MeV on a polypropylene target.

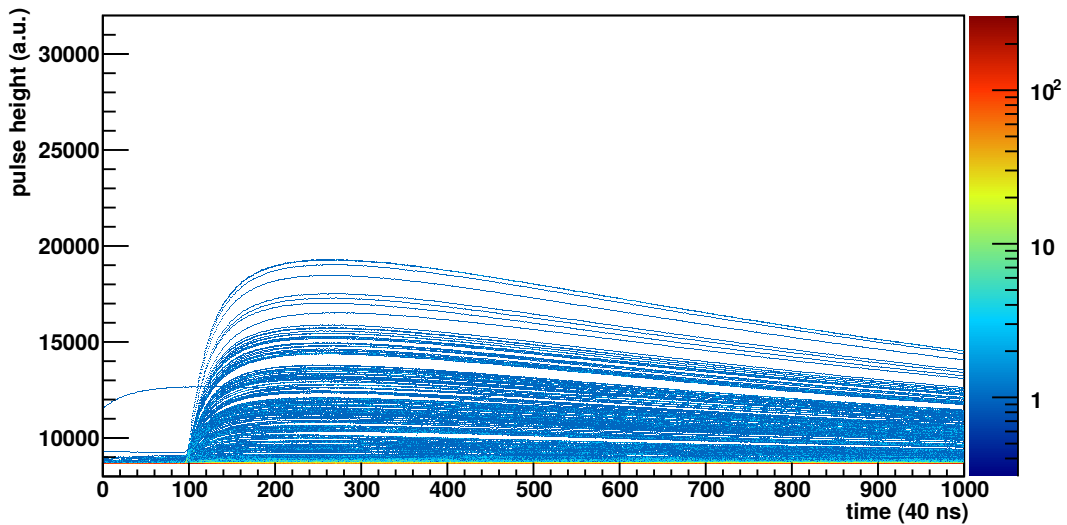


Figure 3.12: Raw signal traces of a CALIFA Petal detector in 300 MeV range sampled with FEBEX3 ADC at 50 MHz decimated by a factor of 2. On the y-axis the pulse height in arbitrary units is plotted versus the time in 40 ns samples on the x-axis. The traces show the characteristic slow rising edge of the CsI(Tl) scintillator as well as the preamplifier decay with $\tau=35$ μs . The data was taken with $E_{\text{beam}} = 200$ MeV on a polypropylene target.

already defined the setup of the detectors. Figure 3.13 shows a schematic overview of the setup. On the left the setup is drawn schematically looking from the top.

The setup configuration displayed in figure 3.13 concept is based on a two-arm spectrometer, with the combination of one DSSSD and a demonstrator petal being used as one arm of the spectrometer. The third petal was used mainly to increase solid angle coverage for γ -ray detection. In normal kinematics the average opening angle ϑ of the free scattered protons was 86° in the lab system due to the Lorentz boost. So positioning of the Petals 0 and 1 was optimized in this way, placing them on opposite sides of the

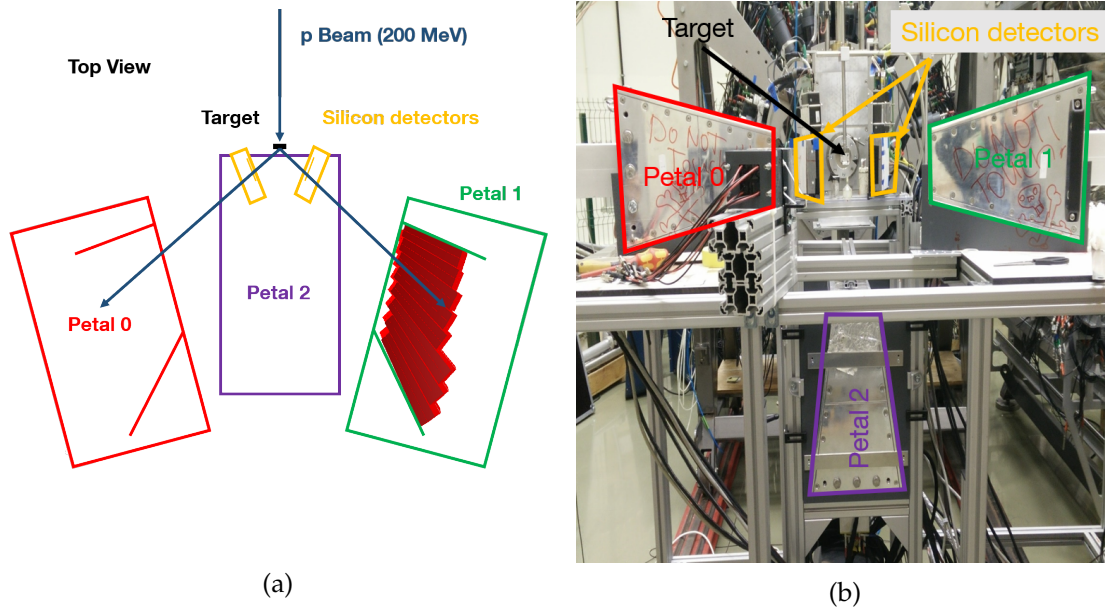


Figure 3.13: Overview of the experiment's setup. Figure a) shows a schematic view from the top of the setup. The **proton beam** comes in from the top hitting the target. The setup is separated into two detector arms right at the target, each containing one **silicon strip detectors** and one demonstrator detector (**petal 0** and **petal 1**). Below the target area, another demonstrator (**petal 2**) is positioned. Figure b) shows the setup as an illustrated picture viewing the experiment from the back. The color code used is analogue to the one used in figure a).

beam axis. To point the tapered crystals to the target each petal was tilted 15° with respect to the beam axis and placed at a distance of 42 cm from the target (respective to the center of the petal) in a CALIFA Endcap-like position. The angular coverage of the petals is then $40^\circ < \vartheta < 58^\circ$ and $-9^\circ < \varphi < 9^\circ$. This way compromises reasonable solid angular coverage while getting protons mostly stopped in a single crystal. Both DSSSDs are positioned at 10 cm distance to the target, to cover Petal 0 and 1 respectively. Important characteristic is also the angular resolution in both polar and azimuthal angle. As the detectors were tilted by 23° , the resolution depends on the hit angle onto the DSSSD. The average of the resolution is calculated to $\bar{\sigma}_{\theta,\phi} = 5.2$ mrad. The angular straggling in air a proton with energy 100 MeV will undergo in 10 cm is $\sigma_{sim} = 2.4$ mrad, so the angular measurement is dominated by the DSSSDs angular resolution. Note, that in the final R³B experiment, the target region is in vacuum, so angular straggling in air is of no concern in CALIFA. To test the CALIFA Barrel configuration of the Petals as well, the remaining Petal 2 was placed in its nominal configuration, meaning distance to the target 30 cm and angular coverage $42^\circ < \vartheta < 90^\circ$. As the setup is introduced, in the next part simulation and first results are presented.

Chapter 4

Full scale (p,2p) simulation

To understand effects due to setup geometry and do qualitative test for future benchmark test with a similar setup, a Geant4 simulation was performed. A (p,2p) event generator to create suitable events was implemented as well. Besides the full implementation of the special experimental geometry a set of different event generators for the QFS reaction have been evaluated.

4.1 Simulation models for QFS

Important for a successful experiment is a substantial understanding of the detector response based on an accurate simulation. For QFS a simulation code first developed by V. Panin and Chulkov[53] used in this thesis is the ideal tool. It is a kinematic simulation, assuming a fixed Gaussian distributed Fermi momentum and different models for angular distribution of the emitted particles. This simulation is widely used as event generator for (p,2p) simulations with experiment specific toolkits like R³Broot. In the following the performance of the event generator is illustrated at the example of the ¹⁶O(p,2p)¹⁵N reaction. If we assume a Gaussian distributed Fermi momentum in the nucleus with $\sigma_{pF} = 100 \text{ MeV}/c$ and a proton beam energy $E_{beam} = 200 \text{ MeV}$, the kinematic characteristics are shown in figure 4.1 in normal kinematics. The individual proton energies are anti-correlated with a weak tail to lower energies (cf. figure 4.1 a). Due to the residuals recoil momentum, the sum energy (cf. figure 4.1 b) is Landau shaped with a peak at $E_1 + E_2 = 187.8 \text{ MeV}$. From the peak's width $\Delta E/E \approx 1.0\%$ (FWHM), the residuals recoil contribution to the energy resolution were estimated. From the difference to E_{beam} we can deduce a proton separation energy $S_p = 12.2 \text{ MeV}$. After reaching the maximum it drops sharply down to 0. Figure 4.1 shows the correlation of the protons' polar emission angle. From equation 1.6 a sharp correlation between the angles is expected. Due to the Fermi momentum distribution of the knocked-out proton, the correlation is smeared out with a maximum of the emission angle of one proton at $\theta = 35.2^\circ$. The opening angle between the protons has its peak position at $\theta_{opang} = 86.3^\circ$ and a width $\Delta\theta = 51^\circ$ (FWHM). Note, that the energy measurement as shown in 4.1 a does not correct for the residual's recoil momentum.

Usually the assumption of an isotropic cross section for particle emission was used as it is sufficiently accurate and increases the speed of the simulation significantly. This assumption was evaluated and in comparison with nuclear transport models showed the performance of the event generator used. In figure 4.2 the polar angle distribution was compared between the "Panin" generator in direct kinematics with it's two cross section options (pp and isotropic) and the Ultra relativistic Quantum Molecular Dynamics (UrQMD) simulation package[54]. The distributions shown in the plots are simulated for the experiment's beam energy $E_{beam} = 200 \text{ MeV}$ and a typical GSI beam energy $E_{beam} = 1000 \text{ MeV}$ in the ¹⁶O((p,2p))¹⁵N reaction. Taking a look at figures 4.2a and 4.2b, both show the normalized polar angular distribution $\frac{dN}{d\theta}$ is plotted versus the polar emission angle of (p,2p) protons for the three different event generation approaches. In figure 4.2a

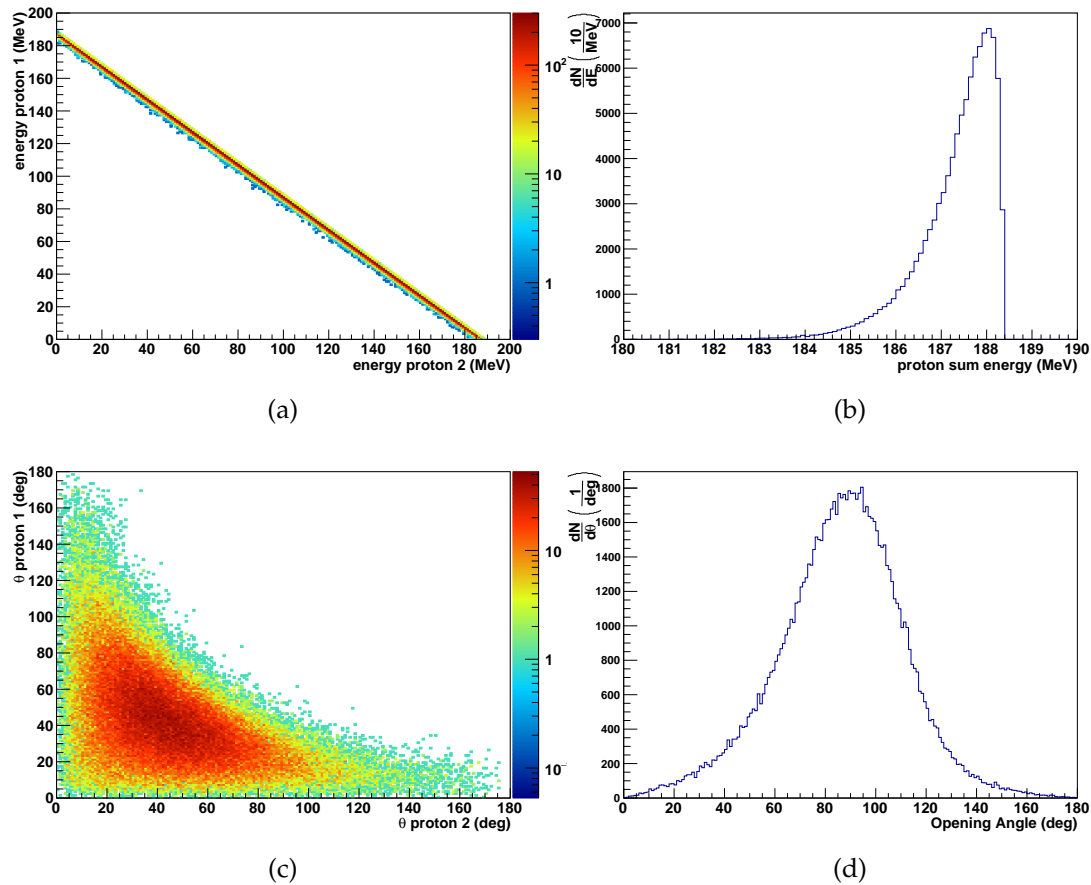


Figure 4.1: Figures show the kinematic features of a (p,2p) reaction in normal kinematics in this case with a ^{16}O nucleus as target and ^{15}N in the ground state after the reaction. Figure a) shows the emitted proton's energy anti correlation with a constant total sum as should be expected (cf. figure b). The shape of the sum energy peak in figure b) is created by the residual nucleus' recoil momentum leading to a $\Delta E/E \approx 1.0\%$ (FWHM). The polar emission angle of both protons is shown in figure c) which is broadened by the intrinsic momentum distribution of the knocked-out proton. Figure d) shows the sum of the polar emission angle of both protons.

shows data simulated with beam energy $E_{beam} = 200$ MeV. The plot created by using the isotropic cross section has a Boltzmann-like shape with tail towards larger emission angles. The data from the UrQMD and the pp cross section simulation are both comparable to the isotropic case and only varies in the peak position (26 to 30 degree). But as the variations are only small, the isotropic cross section is still a good approximation while allowing for a much higher ($\times 10$) computing speed. In figure 4.2b the isotropic cross section data shows a comparable distribution to figure 4.2a and differs strongly from the output of the pp cross section and UrQMD, both showing a double hump structure. Using the isotropic cross section assumption would miss-judge the preferred proton emission angles right in a local minimum of the other two simulation models. On the other hand, UrQMD and the pp cross section create similar distributions only slightly differing in the peak positions. While UrQMD creates a sharper peak at 7 degree and shallower one at around 55 degree, in the pp cross section plot, the peak is broader at 11 degree and more pronounced at 60 degree. Both models agree for the local minimum position at 34 degree emission angle. Additional advantage of using the Panin code, is the possibility to include nuclear excitations of the residual nucleus. To get an idea in which energy regime the isotropic is a good approximation, figure 4.3 shows a superposition of data simulated using the pp cross section in the Panin QFS code for $E_{beam} = 50 - 950$ MeV. Up to

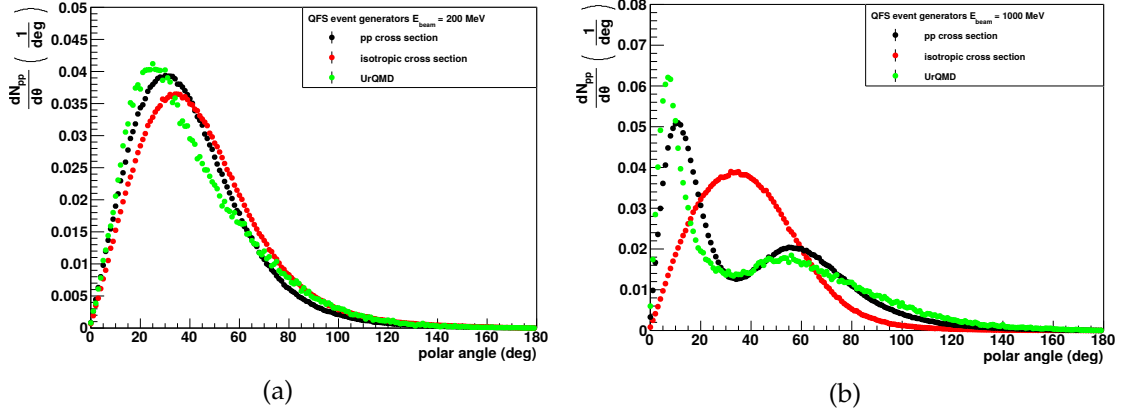


Figure 4.2: Comparison between polar emission angles of the $^{16}\text{O}((p,2p))^{15}\text{N}$ simulated with different simulation packages. Both figures show the normalized polar angular distribution $\frac{dN}{d\theta}$ is plotted versus the polar angle for the three different event generation approaches. The black dots represent the distribution created by using the Panin generator with the pp cross section, while the distribution in red is created by using the isotropic one. Data from the UrQMD simulation is shown in green. While the distributions created by all three generators vary in figure 4.2b ($E_{beam} = 1000$ MeV), they agree nicely in figure 4.2a ($E_{beam} = 200$ MeV).

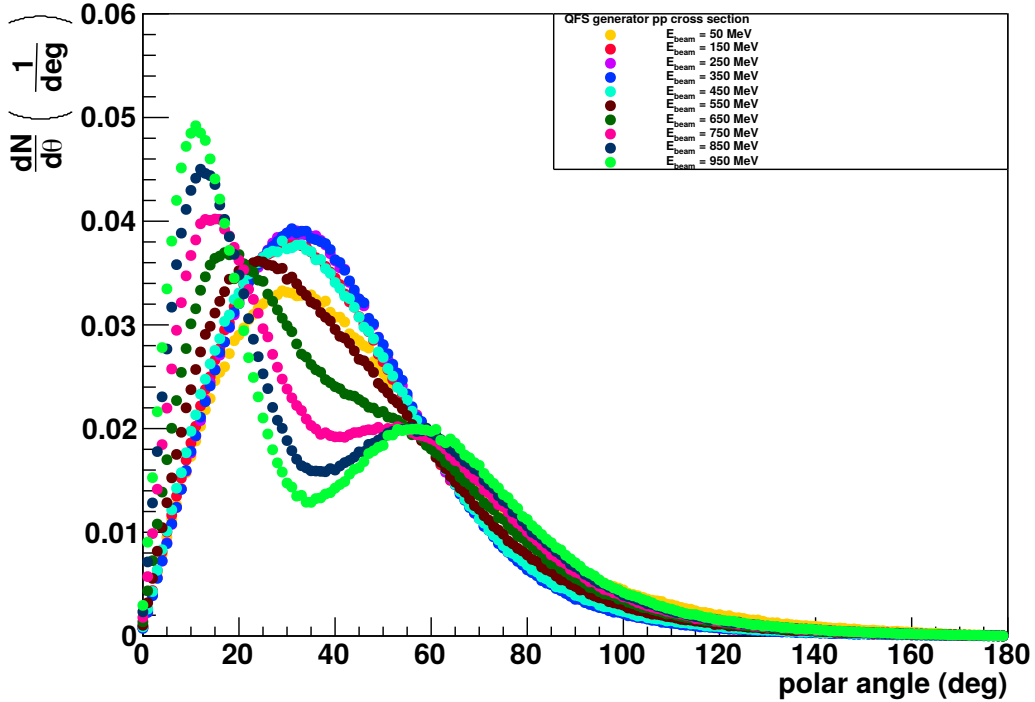


Figure 4.3: Comparison of simulated data using the Panin QFS generator with the pp cross section for $E_{beam} = 50 - 950$ MeV. The data up to $E_{beam} = 450$ MeV shows a similar distribution as expected using the isotropic approximation, but starts to deform towards smaller emission angles starting from 550 MeV, making the isotropic cross section approach invalid with increasing beam energy.

an energy of 450 MeV the distribution still stays Boltzmann-like while the next data set using 550 MeV beam energy starts to show first signs of deformation that continues on with increasing beam energy. From this we propose the use of the isotropic approximation up to 450 MeV. At higher energy it is recommended to use the pp cross section. In the following the isotropic approximation was used to generate the primary events used in the simulation as the differences between the three models compared at 200 MeV are small.

4.2 Simulation of Quasi-free scattering in Geant4

As the aim of the simulation was to mimic the experiment in detail, its complete geometry was introduced into a GEANT4¹ simulation. Using figure 3.13 as a reference, the geometry shown in figure 4.4 was implemented into the simulation framework.

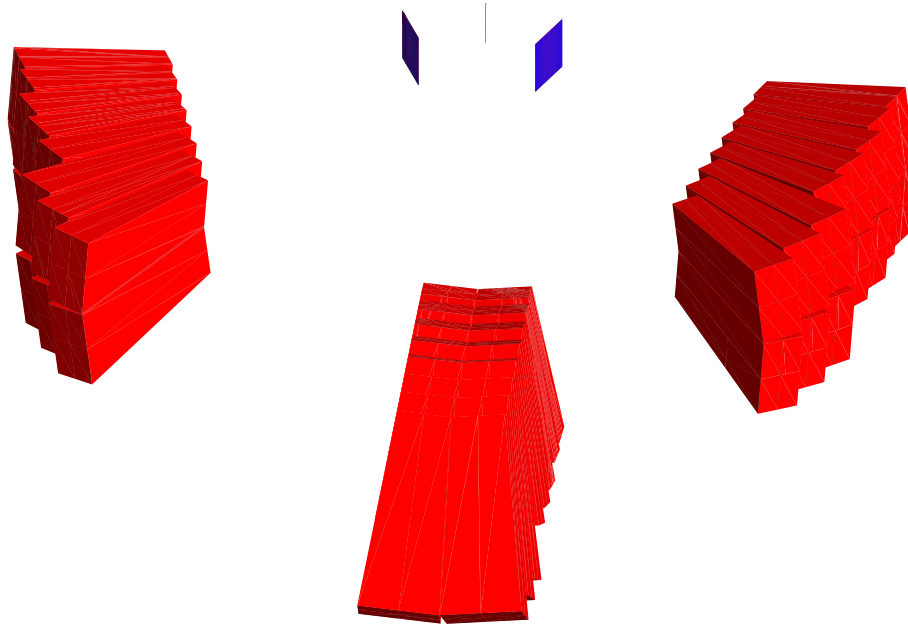


Figure 4.4: Setup converted into Geant4 geometry. Only the detectors and the water fiber are displayed here to avoid confusion. Red represent the wrapped crystals within the alveoli, the backside of the silicon detectors is shown in blue. In the simulation, all detector housings are considered to ensure an exact representation of the experiment.

To make the positioning as easy as possible, the full petal geometry of a single petal is imported through a root-file (developed in cooperation with Jason Park, Lund University). This allowed for changing the petal configuration from single to double and enabled a flexible placement inside the environment. In addition the silicon strip detector was implemented as well into the simulation. Note, that in figure 4.4 the detector housing was not displayed to illustrate the individual crystal placement. The (p,2p)-events were produced based on code created by Valerii Panin([26]), but was rewritten into normal kinematics and imported into the Geant primary generator class to create (p,2p)-events in real-time. The simulation generated two different reaction channels at a fixed ratio (ground state and 6.3 MeV state, 2:1), with coincident single γ -ray de-excitation in case of the excited state. Vertex creation was done by simulating the beam profile in x and y direction and Gauss distributing the vertex over the whole target area. The following simulation results were created using a beam energy $E_{beam} = 200$ MeV.

Figure 4.5 gives an overview of the hit pattern on all five detectors. In the center, the hit pattern upon the DSSSD detectors regarding x-strips vs y-strips is depicted indicating a particle emission focused into forward direction. From figure 4.1 d, on which the event generator was based, an average opening angle of 86.3° is expected. On the left and right of the DSSSD hit pattern, the hit pattern of the corresponding petal is illustrated. Similar to the DSSSDs the hits are concentrated in the forward part of both petals. The bottom petal shown in figure 4.5 below the DSSSD hit pattern, covered a different polar angular range. This leads to the hit distribution to vary, with the most hits registered away from the target. Efficiency for (p,2p) protons however was of no concern for this

¹Cern GEANT4, <https://geant4.web.cern.ch/>

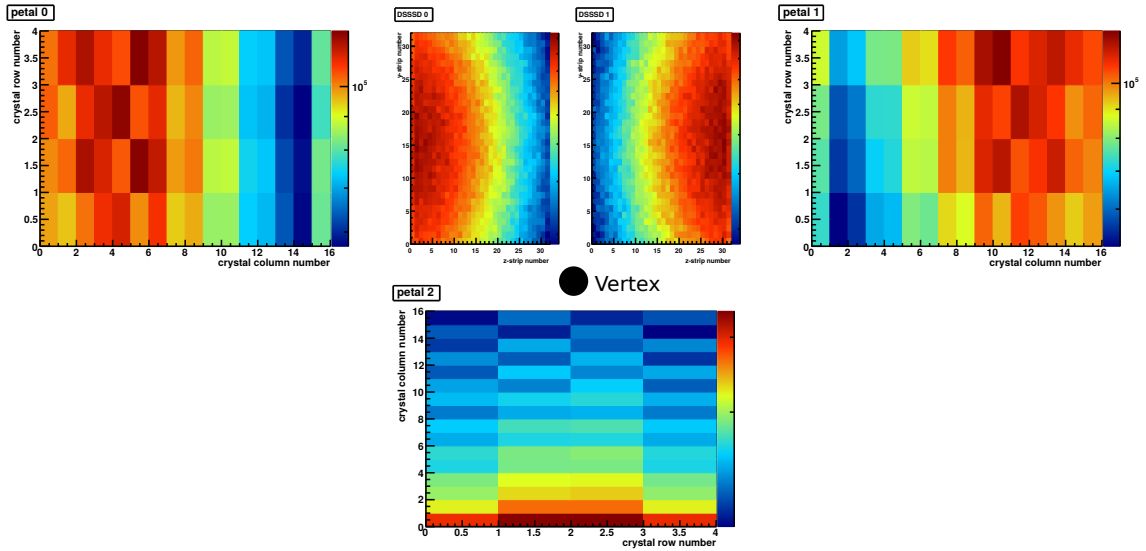


Figure 4.5: Hit distribution of raw data in all detectors with the forward pointing detector arms in the upper row and the third petal below. As expected the majority of quasi free scattered (QFS) protons is emitted in forward direction, but missing each of the arms slightly. Third petal's event distribution starts at the forward facing end, increasing away from the target.

petal, as it is mainly used to increase γ efficiency. The simulation's aim was to give a benchmark value to compare the experiment to. To extract the desired values, a clean signature had to be defined, with the same cuts applying for simulation and experiment. The $^{16}\text{O}(p,2p)^{15}\text{N}$ and the (p,p) elastic scattering reactions have been chosen because of their unique kinematical signature. The well defined polar and azimuth opening angle due to the effective two-body kinematics (low recoil) create correlations, that were used for a clean event identification.

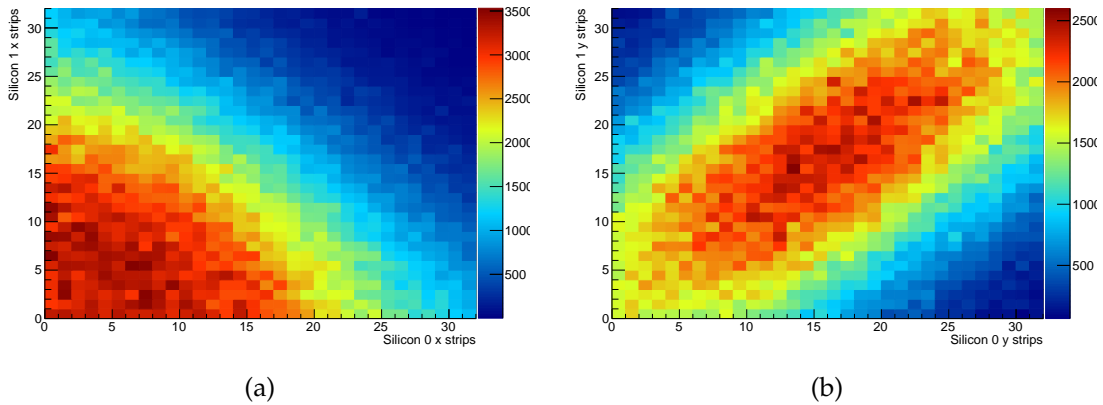


Figure 4.6: Response of simulated DSSSD with $(p,2p)$ events at $E_{beam} = 200\text{ MeV}$. Figure a) shows the correlation of DSSSD x strips corresponding to the polar opening angle of the QFS protons. The plot shows the expected smearing from the intrinsic momentum distribution of nuclei in the target nucleus. Figure b) shows the correlation of DSSSD y strips corresponding to the azimuthal opening angle of the QFS proton emission. The expected back-to-back emission of the QFS protons can be observed.

Figure 4.6 shows the correlations of the polar (figure 4.6a) and azimuthal angle (figure 4.6b) respectively. In polar angle the broad distribution of the protons is peaking towards forward particle emission. As no sharp signature is visible, applying a cut here is neglected.

Looking at the azimuthal angular correlations, the expected average azimuth opening angle of 180° is visible by a broad band covering most of the DSSSDs acceptance. In both cases the sharp two body kinematical correlation is smeared by the Fermi motion.

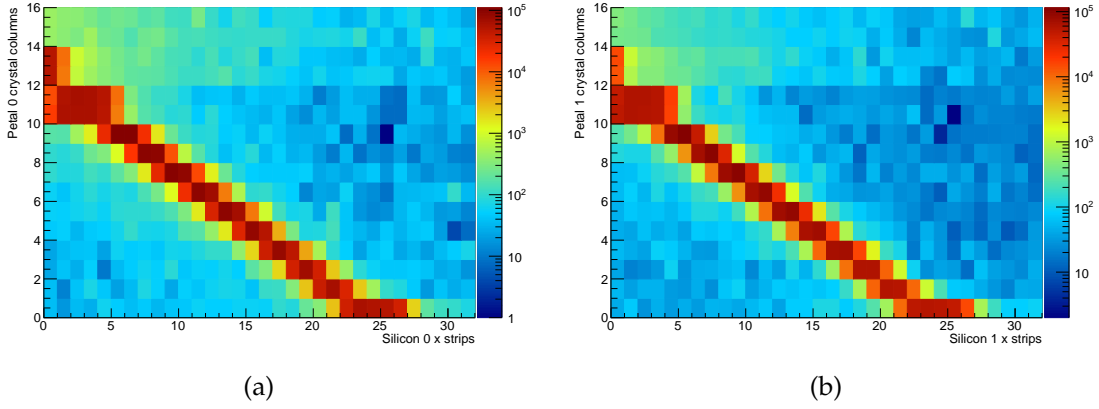


Figure 4.7: Vertex reconstruction simulation with (p,2p) events at $E_{beam} = 200$ MeV. The correlation between the DSSSD's x-strips and the crystals's vertical columns show a clear track stemming from the target reactions.

For the identification of proton tracks originating from the target the petal-DSSSD correlations in both arms, shown in figure 4.7, were used. Both plots look almost exactly the same due to the perfect detector positioning in the simulation. In both an anti correlation was observed between the petal's crystal columns and the DSSSD strips. From this line two things were immediately learned. As the line ends at column 14, the DSSSD did not cover the whole petal in this configuration. For future experiments the position of the DSSSD needs to be optimized with respect to the petal. Also the correlation between those two detectors were used as a vertex reconstruction method. A selection on this correlation on both sides reduced uncorrelated background from reactions happening outside the target. To show the importance of this selection, figure 4.8 shows the correlation between the energy deposition in the petals 0 and 1. Here clear anti correlations were observed. As known from the purely kinematic simulation in figure 4.1a, only two lines corresponding to the ground state and excited state of the ^{15}N nucleus should be observed as this is used as event input. To separate these two lines from the background a further event selection was necessary. Applying the vertex cut (cf. figure 4.7 correlation) on both arms of the setup results in the plot shown in figure 4.9a. Here only the two lines corresponding to the ground and excited state remained with reduced background. Both lines in figure 4.9a show a slight bending, where the energy distribution of the scattered protons was asymmetric. This bending was due to the higher energy loss in air and other materials between the vertex point and the full absorption in the detector for the lower velocity proton according to the Bethe-Bloch equation. For non-relativistic protons this in first order is expressed by

$$\Delta E \approx \frac{1}{\beta^2} \approx \frac{1}{E} \quad (4.1)$$

So based on this, the energy loss difference was modeled by the following semi-empirical function:

$$E_{0,1}(E_{1,0}) = \frac{A}{B \cdot E_{1,0} + C} + D \quad (4.2)$$

with appropriate values for the parameters A,B,C and D gained from fitting the energy anti correlation lines in figure 4.9a. The energy loss correction ΔE was calculated as illustrated

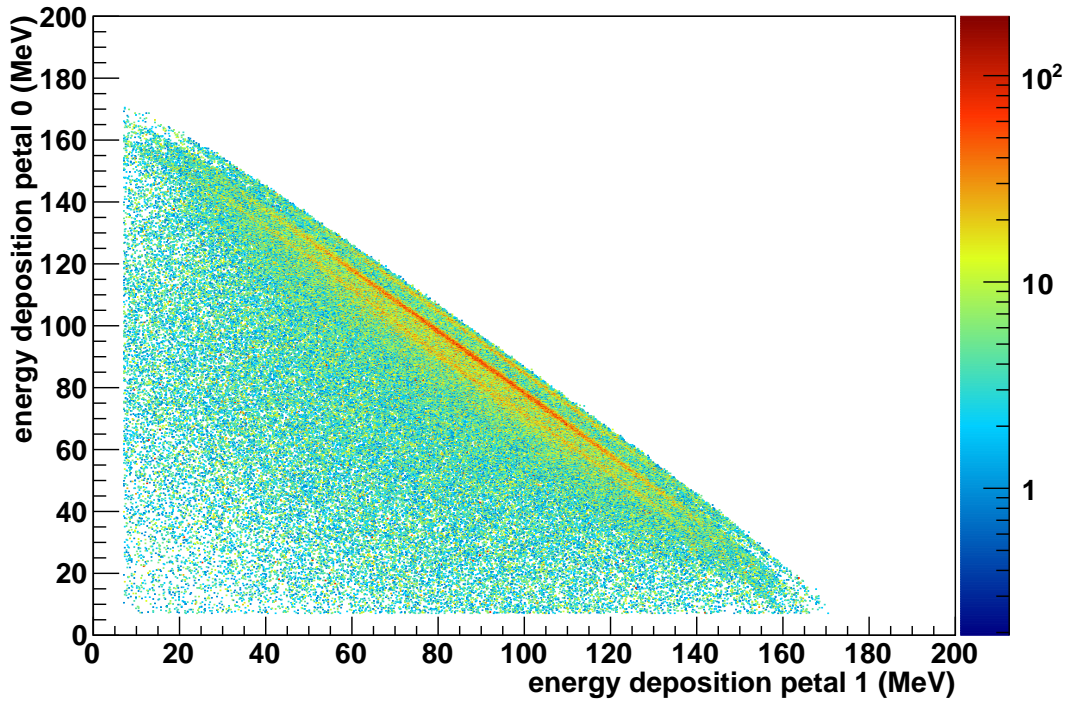


Figure 4.8: Correlation between the energy deposited in petal 0 and petal 1 for raw simulation data of (p,2p) events at $E_{beam} = 200$ MeV. Two anti correlation lines are already distinguishable from the background. These two correlations are associated to the ground state and excited state event data used as input. The additional third line observed in the histogram is due to energy loss in the DSSSD housing box.

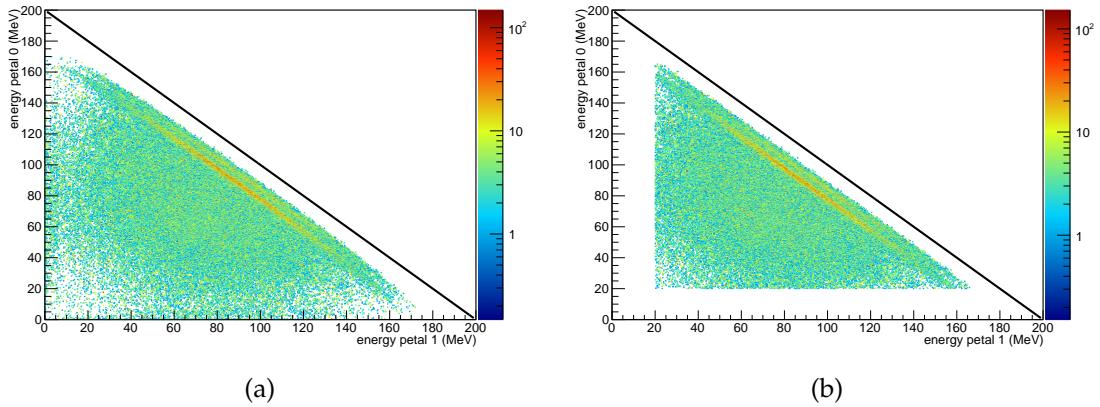


Figure 4.9: Correlation between the energy deposited in petal 0 and petal 1 after QFS selection cuts. Both plots show two anti correlation lines corresponding to the states used as input for the simulation. In plot a) the lines are bent slightly towards lower energy deposition, especially notable for low energy protons as indicated by comparison with the black diagonal. Figure b) shows the same plot with this effect corrected for by using the empiric function 4.1.

in figure 4.10. The energetic difference to the expected linear anti correlation $\Delta E_{0,1}$ is trigonometrically related to the ΔE by

$$\Delta E = 0.5 \cdot \sqrt{\Delta E_0^2 + \Delta E_1^2} \quad (4.3)$$

with $\Delta E_{0,1}$ calculated using equation 4.2. Applying the correction by $E' = E + \Delta E$ results in

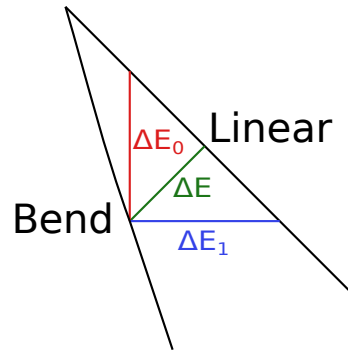


Figure 4.10: Illustration of the asymmetric energy loss correction ΔE of (p,2p) protons in petals 0 and 1. This correction was calculated by calculating the variation from the expected linear correlation for petal 0 (ΔE_0) and petal 1 (ΔE_1) individually using 4.2. These create a triangle, its hypotenuses being twice the sought energy loss correction ΔE .

the plot shown in figure 4.9b. The lines are now completely straight after correction of the small variation in energy loss. As this occurred in the experiment as well, the function used here can be used for the experimental data.

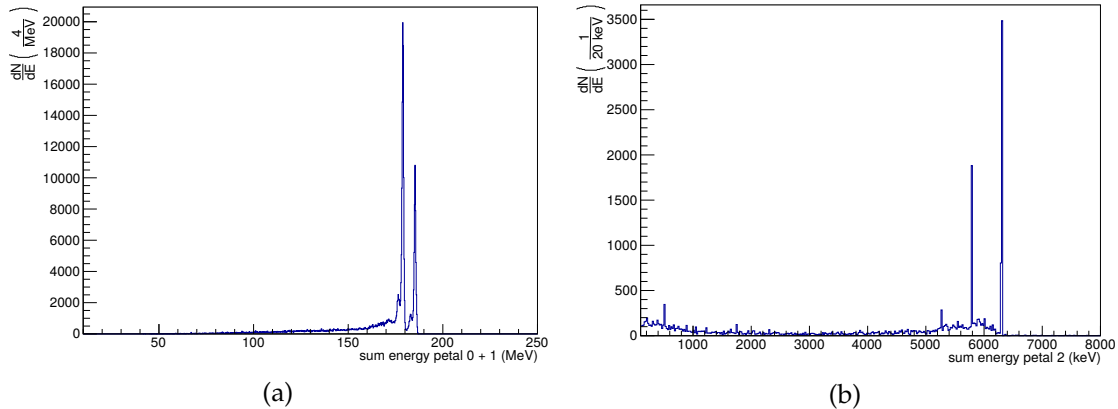


Figure 4.11: Sum of the kinetic energy for both protons (a) and coincident γ -rays in petal 2 (b) spectra after the vertex cut in simulation. The energy sum shows peaks for the two simulated states of ^{15}N with a tail towards lower energy deposition. These events stem from reaction in some passive material or the detector itself. In plot b) the full energy peak in petal 2 at 6.3 MeV as well as the single escape peak and a very weak double escape peak can be observed. Note that no finite detector resolution was used in this simulation. Clearly the smearing through Bremsstrahlungs-effects in the high energy regime is observable in the missing Compton edges for the photo peaks detected.

Figure 4.11a shows the energy sum of both protons after the correction. As no detector resolution was included in the simulation at this point, the line broadening due to the residual nucleus' recoil contributing $\frac{\Delta E}{E}(\text{FWHM}) = 1.0\%$ is observed in the two peaks corresponding to the ground and excited state. Figure 4.11b shows the energy sum of coincidence events in petal 2. The 6.3 MeV full energy peak was observed with the single and double escape peaks present as well. Due to Bremsstrahlung of the secondary electrons with kinetic energy above 40 keV[55] created by γ -radiation detection, the Compton edges of the three photo peaks observed were no longer visible as the energy deposition is smeared by Bremsstrahlungs losses. Due to this effect, all detected γ -ray events beyond the double escape peak were considered as detected excitation γ -rays in the efficiency calculation. Note, that in the following figures, a realistic energy resolution of 6% at 1 MeV (petal 2) and 8% at 1 MeV (petal 0/1) was implemented in the simulation. To extract the efficiency, a cut on the two proton correlation line associated with the excited state in

figure 4.12a. This defined the total number of detected excited states N_{exe} resulting in exactly one γ emitted from the target. With the number of γ -rays detected in coincidence with the two-proton correlation N_{γ} the absolute efficiency was defined as

$$\epsilon = \frac{N_{\gamma}}{N_{\text{exe}}} \quad (4.4)$$

This contained also the geometrical acceptance of the setup. Petal 2 was configured in the nominal CALIFA position, covering 9.6% of the solid angle in the lab. Calculating the photo peak efficiency of petal 2 for γ -rays at 6.3 MeV using figure 4.12b results in $\epsilon_{FE,p2} = 1.8\%$. If additionally the events with $E_{\gamma} > 5$ MeV were considered the efficiency increases to $\epsilon_{p2} = 2.6\%$. This value sets a benchmark for the efficiency expected to be extracted from the experiment data. As the proton events were limited to a few crystals in petal 0 and 1 only, the rest of each petal was used to increase the γ -ray detection efficiency. A simple separation was done by identifying the crystals with proton energy deposition by particle identification, then summing up the energy deposition in the rest of the detectors.

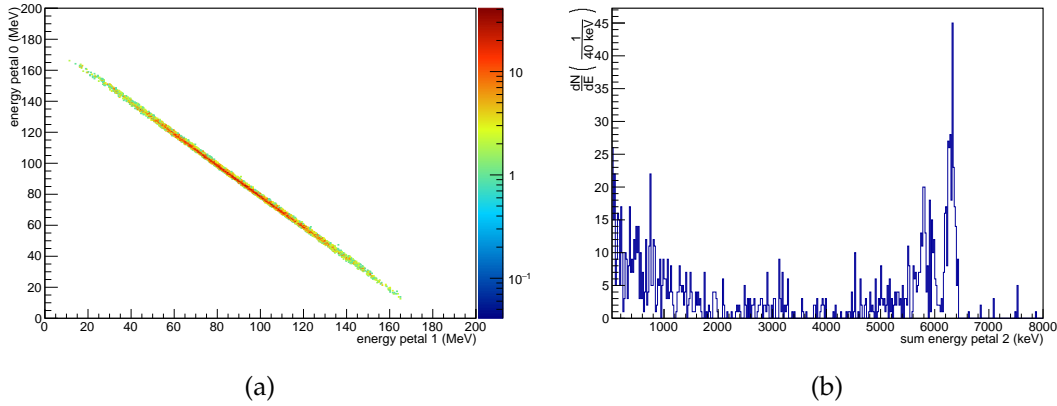


Figure 4.12: Cut on the two proton correlation line associated with the excited state (a) with corresponding coincident γ -ray spectrum (b). The 6.3 MeV excitation γ -ray full energy peak was observed with additional some single and double escape peak structure recognizable. The total detection efficiency using events with $E_{\gamma} > 5$ MeV is $\epsilon = 2.6\%$. Note, that for this simulation a realistic energy resolution of 6% at 1 MeV was implemented.

The crystals containing the proton hits first are isolated by looking for the largest energy deposition and removing the surrounding eight direct neighbor crystals. Doing so in simulation was a first indication if this technique is also viable in the experiment. More important in CALIFA γ and proton events need to be treated the same way to use the solid angle coverage of CALIFA to its full potential. Figure 4.13 shows a comparison of all detected γ -rays from (p,2p) reactions compared between petal 0 (red) and petal 2 (blue) on the left and on the right a comparison of both petals after applying cuts on vertex, proton energy and PID. In both petals a full energy peak at 6.3 MeV is observed as well as the corresponding single escape peak. Due to the compact shape of the petals, the double escape peak is strongly suppressed. The expected 511 keV line is also visible weakly above the Compton background dominating the rest of the spectrum. After selecting the excited state, the full energy and single escape peak are still observable. Note, that the signal to background in petal 0 is worse than petal 2 due to residual effects of the proton detected there. But both peaks are observed above the background, though of course less than in petal 2 due to the cut out of the proton event and the reduced geometrical acceptance. Adding the detected γ -rays in petal 0 and 1, the setups γ -ray detection efficiency increases to $\epsilon_{\text{total}} = 5\%$ at 6,3 MeV. This value set the expectation for the total γ -ray detection efficiency from the experiment. In figure 4.13 the low number of

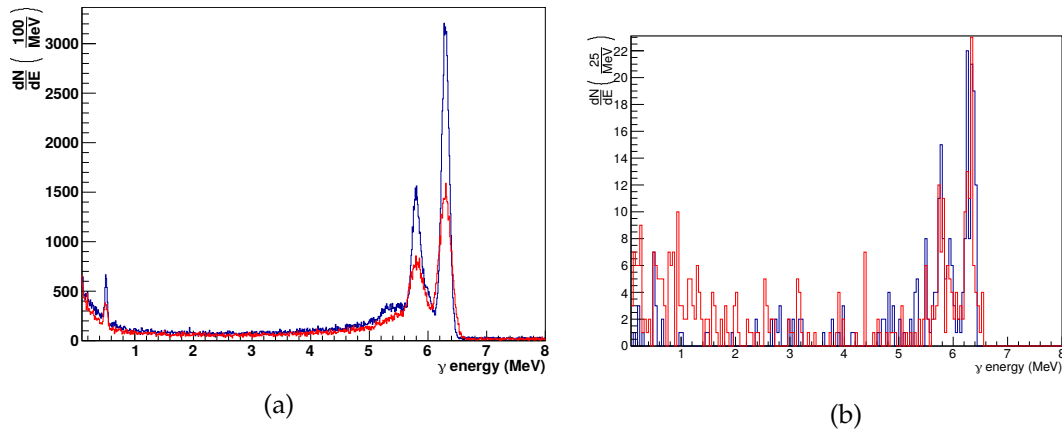


Figure 4.13: Comparison of γ -ray detection in petal 0 (red) and petal 2 (blue). In figure a) all detected γ -rays are plotted with the full energy and single escape peak clearly observable. The petal 2 (blue) also shows a broad double escape peak, which is strongly suppressed, while petal 0 (red) this seems to vanish within the Compton continuum, as peak statistics are much smaller here. Figure b) shows the remaining γ -ray events after applying a 2 proton cut and a cut on the excitation energy on the simulation data. In both histograms the full energy peak at 6.3 MeV is observed as well as the single escape peak with strongly reduced statistics. Using all three petals combined for proton and γ detection increases the efficiency to $\epsilon_{\text{total}} = 5\%$.

coincident γ -ray events bear witness to the small angular coverage especially considering the probability of both protons and one γ hitting the corresponding detector units. To show the improvement of using the whole CALIFA calorimeter the same number of events was simulated with with it. The resulting proton and γ spectra are shown in figure 4.14.

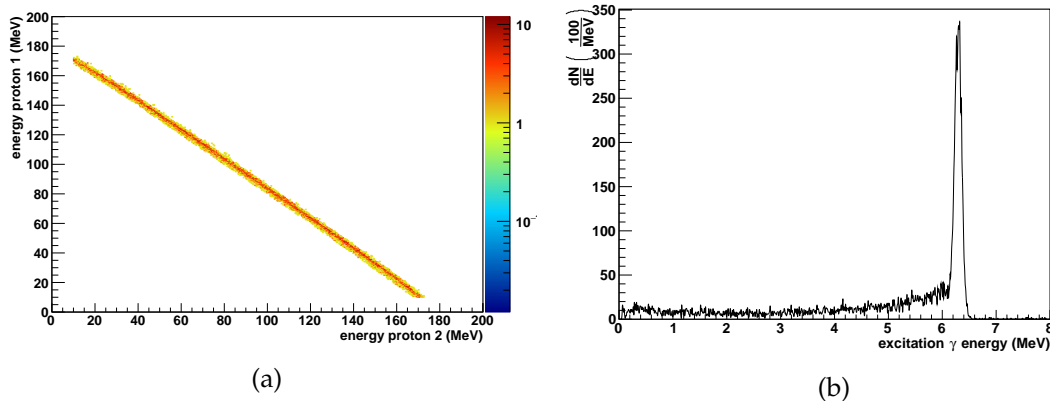


Figure 4.14: Coincident two proton correlations (a) and γ (b) detection using the whole CALIFA calorimeter with the same number of events as used in figure 4.13. The effect of increasing the angular coverage is drastic in terms of the γ spectrum showing a single full energy peak far above the background opposed to figure 4.13. Using CALIFA an efficiency of $\epsilon_{\gamma, \text{simCALIFA}} = 40.8\%$ is expected.

Selecting the protons detected as originating from the excited state of ^{15}N in figure 4.14a yields the coincident γ -ray spectrum 4.14b. In contrast to figure 4.13, only the full energy peak remains, as in CALIFA the angular coverage of over 80% ensures almost no single or double escape γ s to be observed. Using this a the photo peak efficiency $\epsilon_{\gamma, \text{simCALIFA}} = (40.8 \pm 0.4)\%$ at 6.3 MeV was calculated.

As the Missing Mass formula in first order collapses to a missing energy measurement at this energies in normal kinematics, the excitation energy spectrum was extracted

from the simulation by direct energy measurement. The ground state and 6.3 MeV used

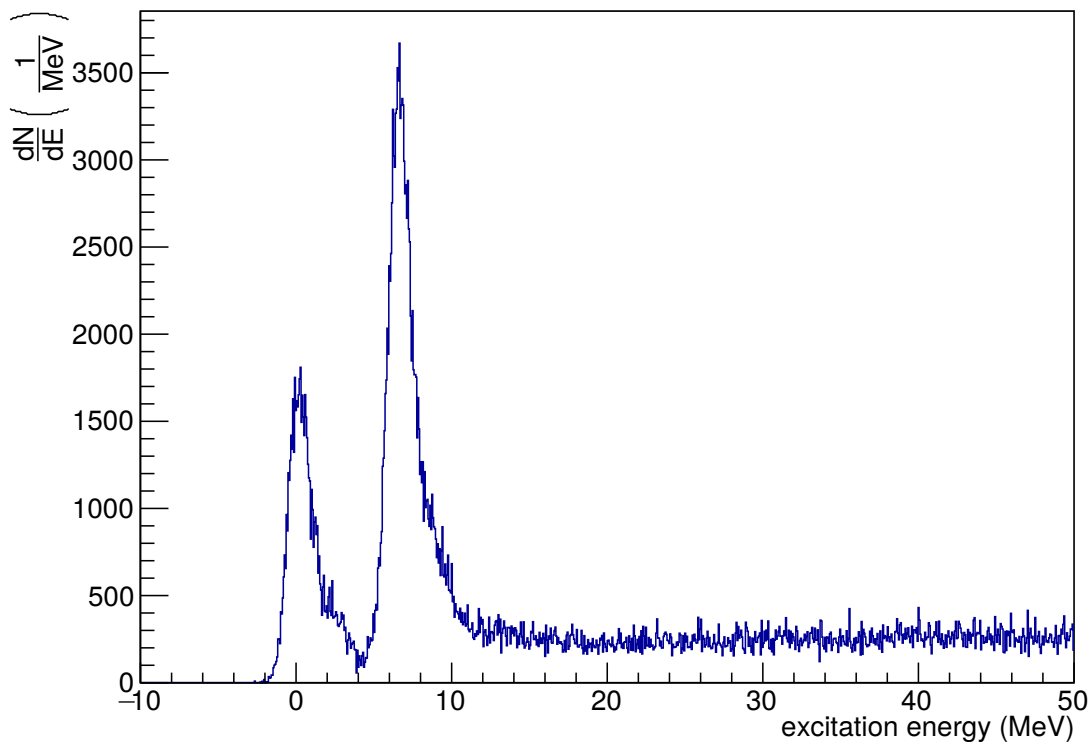


Figure 4.15: Figure shows the simulated excitation energy spectrum from direct energy measurement. The ground state and 6.3 MeV used as simulation input are observed as well as a background tail towards higher excitation energies. Their width is 2.0 MeV(GS) and 2.1 MeV(6.3 MeV) in FWHM.

as simulation input were observed at the appropriate energy. Both peaks have a tail toward higher excitation energies from the recoil of the residual nucleus. Their width is 1.0 MeV(GS) and 1.1 MeV(6.3 MeV) in FWHM, setting a benchmark for the expected resolution of the excitation energy measurement in the experiment. The FWHM was measured by taking the full width of the peak at half its height. This concludes the simulations proper performance of the desired event data in a full scale setup.

Chapter 5

Data analysis

The analysis of the data set taken with the monoenergetic proton beam $E_{beam} = 200$ MeV is a multi step procedure outlined in the following sections. First a calibration using a γ source was done to have a first estimation for the coefficient transforming energy deposit into digital amplitudes. This includes all effective transfer coefficients like number of predicted photons per MeV energy deposit, reductive light collection, APD quantum efficiency, APD gain, preamplification gain and the electronics in the FEBEX modules itself. Second step was then using elastic proton-proton scattering on a CH_2 target to improve this calibration to the actual measured proton energies in the petals. This was a small factor to take into account the quantum factor for protons in CsI(Tl). In addition it provided a calibration point close to the energies important for the later analysis. As the calibration was done, we searched for the event pattern in the petals as well as in the silicon detectors. Understanding these patterns was essential to the event selection of proper (p,2p) events. This selection was then compared with a simulation containing only the desired (p,2p) events, to verify the efficiency of geometrical constraints. After the selection, the excitation energy as well as proton and γ detection efficiencies and the (p,2p) cross section were extracted from the data.

5.1 Calibration

For the high granularity setup as described in section 3.2.4 a calibration procedure is essential to measure all observables on an absolute scale. For the CsI(Tl) crystals both energy ranges γ -rays and protons had to be calibrated respectively. Such a procedure is presented in the following sections.

5.1.1 γ calibration

Calibrating the individual crystals in each petal is usually the first step when commissioning. In this case a ^{60}Co source was placed at the target position. With a probability of 99.88% ^{60}Co decays to the 4^+ state of ^{60}Ni which cascades through the 2^+ state down to the ground state by emitting two γ -rays with $E_\gamma^1 = 1.173$ MeV and $E_\gamma^2 = 1.333$ MeV. These being 160 keV apart giving an excellent benchmark for the expected γ -ray separation and resolution at 1 MeV and setting a first mark for the overall performance of the petal in γ radiation detection. A special challenge for CALIFA is detection of γ -rays and charged particles at the same time and in a very high dynamic range ranging from 100 keV to 700 MeV, for which the previously mentioned preamplifier has different ranges, to optimize the used ADC range and thus the digital signal resolution. In figure 5.1 two single crystals were selected one from a petal tuned for particle detection (figure a), petal 0) the other for γ -ray detection (figure b), petal 2) both irradiated with the ^{60}Co source. Petal 1, not shown here, was tuned for particle detection as well and performed within the same range as petal 0 does. After calibration using both γ -rays, the energy resolution was measured. This yields $\frac{\Delta E}{E} = 5.6\%$ (FWHM) at 1.173 MeV for petal 0 and $\frac{\Delta E}{E} = 4.6\%$ (FWHM) at 1.173 MeV for petal 2. These values are in excellent agreement with the resolution

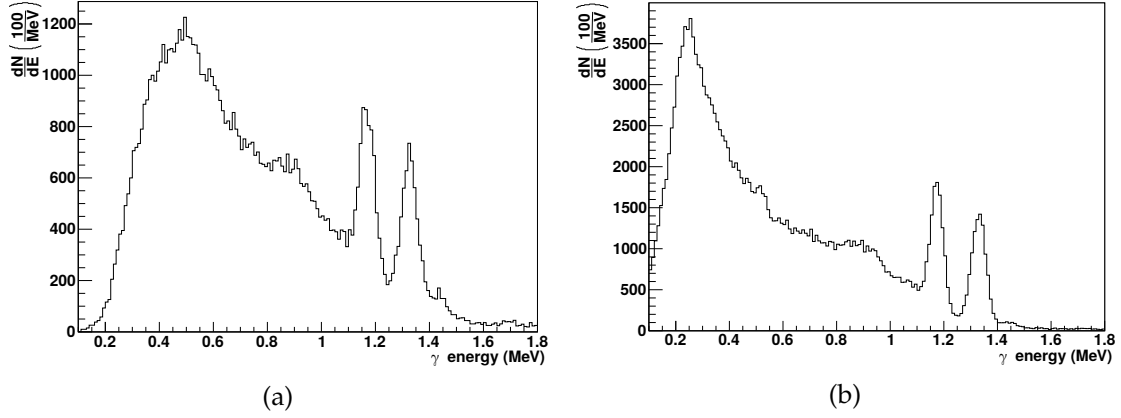


Figure 5.1: Energy spectra of γ -rays emitted by a ^{60}Co source. Figure a) shows a single crystal spectrum from petal 0 in low gain mode. The 1.173 MeV and 1.333 MeV lines can be clearly distinguished from the Compton background and are nicely separated. Their resolution is $\frac{\Delta E}{E}$ (FWHM) = 5.6%. Figure b) shows a single crystal spectrum from petal 2 in high gain mode. Apart from the higher statistics due to a lower distance to the target, the two peaks are even better separated than in figure a). Their resolution is $\frac{\Delta E}{E}$ (FWHM) = 4.6%.

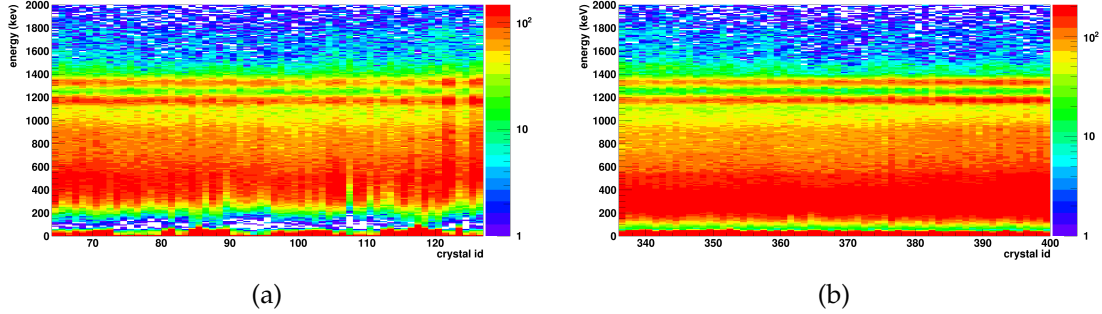


Figure 5.2: Figure a) shows the calibrated ^{60}Co spectra of each crystal in petal 0 identified by its crystal id. The calibration of the two peaks was successful as they can be found at their associated energy. Some detectors differ concerning their energy threshold setting as the resolution of the lines seems to vary between the detectors. Figure b) shows the calibrated ^{60}Co spectra of each crystal in petal 2 identified by its crystal id. The calibration of the two peaks was successful as they can be found at their associated energy. The thresholds and individual resolutions look more homogeneous in figure b) compared to a).

requirements for CALIFA. Figure 5.2 shows histograms of crystal ids plotted versus γ energy after calibration for petal 0 (a) and petal 2 (b). Both figures show nicely aligned the two full energy peaks for all the 64 channels of each petal. The thresholds and individual resolutions look more homogeneous in figure b) compared to a). This was partly due to the difference in preamplifier gain used in petal 0 and 2. As petal 0 was operated in the low gain mode, the output signals were a factor 11 smaller than the ones from petal 2. This lowers the effective sampling resolution of the ADCs by the same value. If the energy range of petal was chosen to be 20 MeV per 14-bit the ADC supplied, 0.7 bit/MeV were available for γ -detection. On the other hand, the petals tuned for particle detection would only have 0.06 bit/MeV. This effect influenced the resolution achievable for the petals. Looking into the overall petal sum for all three petals, the following energy resolutions were achieved for each petal respectively.

$$\left(\frac{\Delta E}{E}\right)_{\text{total,petal0}} = 6.6\% \quad \left(\frac{\Delta E}{E}\right)_{\text{total,petal1}} = 6.4\% \quad \left(\frac{\Delta E}{E}\right)_{\text{total,petal2}} = 5.5\% \quad (5.1)$$

These values show the operation of both all three petals within the expected parameters, though petal 2 performed better than the other two. To check if this effect is corresponding to the chosen detection range in the preamplifier, the energy resolution is also measured for petal 2 in particle detection mode. This measurement yields a resolution $\frac{\Delta E}{E} = 5.9\%$ (FWHM) at 1.173 MeV for the total petal sum. Even though this showed the effect of the preamplifier range on the energy resolution, it did not completely close the gap concerning energy resolution between petal 0,1 and 2. An explanation for the discrepancy could be the usage of different optical glues in petal 0/1 and petal 2, as they were produced at different locations (Lund, Sweden and Darmstadt, Germany) following different production procedures.

A calibration using γ -rays is sufficient for petal 2, as this is planned for γ -ray detection only, it was needed to verify the quality of the calibration up to $E_\gamma = 10$ MeV to see if γ -ray sources with higher energy emission need to be used in the future. The procedure used is explained in the following.

5.1.2 Proton calibration with polypropylene target

Petal 0 and 1 were calibrated in addition with protons, as the scintillation produced by charged particles in CsI(Tl) experiences negative quenching[41]. Elastic scattered protons using a monoenergetic proton beam $E_{beam} = 200$ MeV and a 500 μm thick polypropylene target served as a very precise proton source. Through elastic scattering ${}^1\text{H}(p,p'){}^1\text{H}$ we achieved a relatively homogeneous irradiation of both petals at the same time with well defined particle energies. Drawback in this case was the angular dependence of the scattered proton's energy which made it difficult to know the exact energy the proton had upon entering the detector. A more precise way was using the constant sum energy of each pair of scattered protons. Figure 5.3 shows a 2D histogram with both energy depositions of petal 0 and 1 plotted against each other. A clear anti-correlation line between the energies

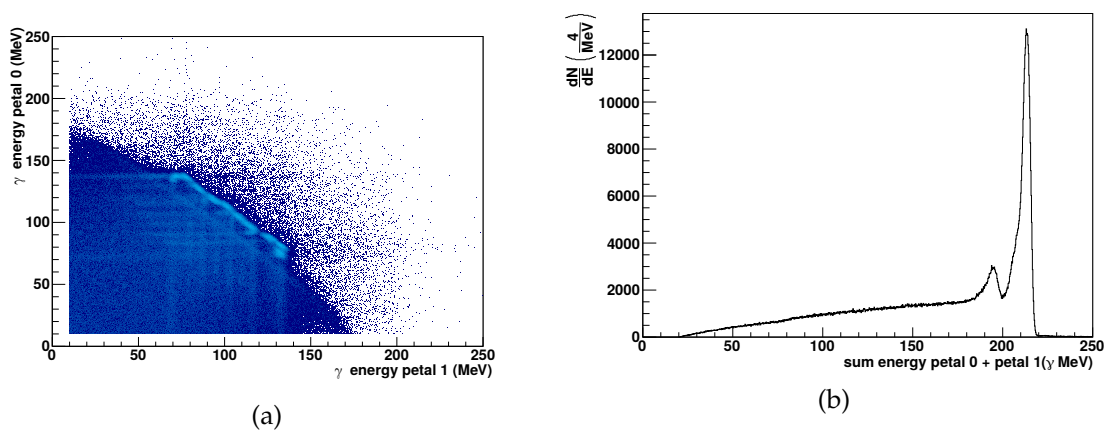


Figure 5.3: Figure a) shows the energy correlation between petal 0 and 1 from raw data taken with a polypropylene target and a 200 MeV proton beam. The anti correlation line of the elastic scattered protons is observed next to background created by reactions in the air. The anti correlation line is not straight but made up of several individual peaks with varying energy sum. Figure b) shows the energy sum of petal 0 and 1 for the same data. A large peak with a tail toward smaller energies at 213.5 MeV is identified as the sum peak of the elastic scattered protons ($\frac{\Delta E}{E}$ (FWHM) = 2%). The tail is associated with the scattered composition of the anti correlation line in figure a). The secondary peak is associated with background reactions in the air.

deposited in petal 0 and 1 were observed. The line was not straight and seems to be made up of several individual peaks, each corresponding to a crystal combination hit by the

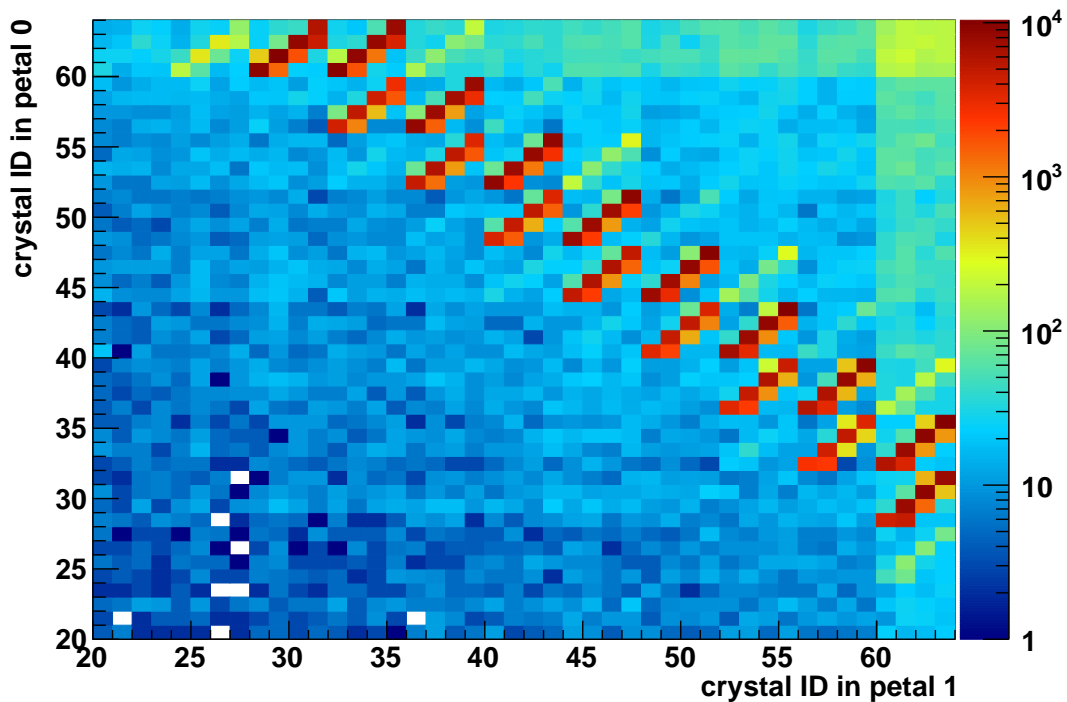


Figure 5.4: Correlation plot between the crystals in petal 0 and petal 1 for data taken with a polypropylene target and a 200 MeV proton beam. The stair like structure in the plot indicates correlated events in a crystal pair from elastic scattering exhibiting a constant energy sum to calibrate on. The square shaped area in the upper right corner, and the two bands protruding from it, are due to reactions of beam protons in the air after the target preferably hitting the forward detector elements.

pair of elastic scattered protons. The fact, that a line was actually visible and not only individual peaks scattered within the range of the plot shows that the calibration using the ^{60}Co source was already a very good approximation also for high energy deposit of the protons. If we take a look at the sum energy of petal 0 and 1 (cf. figure 5.3b), the full energy peak had a tail towards smaller energies associated with the scattered composition of the anti correlation line in figure 5.3a. Its position is at $E_{\text{sum}} = 213.5 \text{ MeV}$ with a resolution $\frac{\Delta E}{E}$ (FWHM) = 2%. Note that this picture was raw data, only using the γ calibration without any additional event selection. As the beam energy was only 200 MeV, the effect of the negative quenching is visible here with a factor of 1.07. Compared to γ -ray energies, the protons now produce more scintillation light per MeV. In order to correct this effect, we used a fine tuning based on the petal correlations of the elastic scattered protons and at the same time remove the pair correlation effect by correcting on all possible crystal combinations between petal 0 and 1. These combinations are shown in figure 5.4. Each of these combinations was identified by the stair like structure in the figure as this correlates the four crystal rows of a petal for each column. That in turn identified the associated crystal columns and rows. Taking the sum of the identified crystal pair and comparing it to the beam energy, a calibration factor is calculated for this crystal pair. This way all possible combinations were considered in the calibration. Where no correlation data was available, the negative quenching was calculated out of the γ calibration. In this way, a tuning matrix was created for the petals, where each element represents a correction factor of the The result of the calibration is shown in figure 5.5a. In comparison to figure 5.3a the line is now almost completely straight. Only at both ends of the line it broadens due

to acceptance effects of the petals. Straightening the line also improved the total energy resolution $\frac{\Delta E}{E} = 1.5\%$ (FWHM). As two crystals each contribute to this value, and assuming

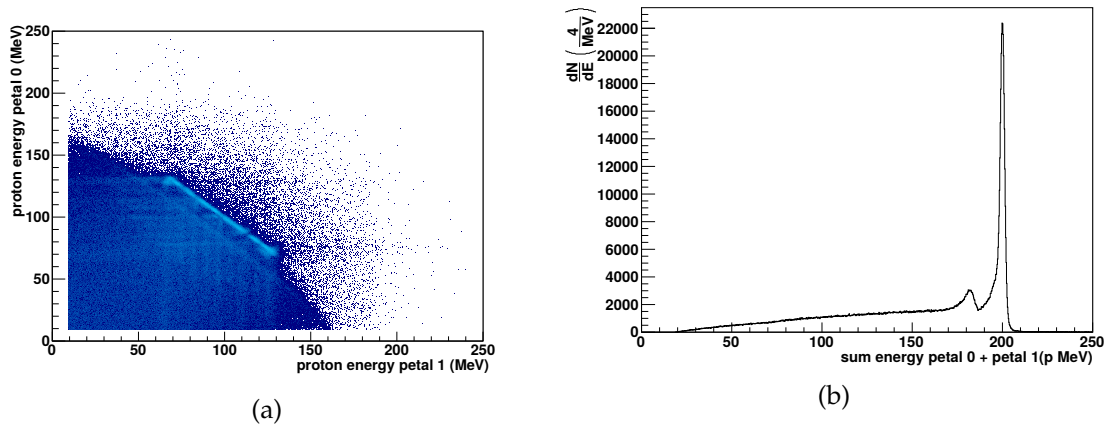


Figure 5.5: Figure a) shows the proton calibrated energy correlations for petal 0 and 1 from the raw data taken using the polypropylene target and a proton beam with 200 MeV energy. After the calibration the anti correlation line is now straight except for acceptance effects at the edges. Translated to the energy sum in figure b) the tail of the peak is reduced, increasing the resolution to $\frac{\Delta E}{E}$ (FWHM) = 1.5%

a similar error at similar energies for both of them, the individual crystal resolution was calculated by division through $\sqrt{2}$, resulting in a single crystal resolution $\frac{\Delta E}{E}_{sc} = 1.0\%$ (FWHM). This concludes the necessary energy calibration steps for the petals.

5.1.3 Position calibration

After energy calibration we also had to calibrate absolute detector position for the full setup and the calibration of the DSSSD's strips to absolute values eg. position in mm and the polar and azimuthal emission angle of the particles detected. In case of the DSSSD detectors the relative positioning of each strip was well defined by the production technique. Here the important task was to present an absolute position of the wafer with relation to the target position and the beam vector. The raw DSSSD hit pattern polts are shown in figure 5.6 for the same data set as used for the proton energy calibration. Figure 5.6a shows the pattern measured by DSSSD0. Using a event trigger in the experiment that required at least one proton in either petal (OR - trigger, cf. section 3.2.3) resulted in the observed projection of the petal's front surface onto the DSSSD's event pattern. The remaining area showed a homogeneous irradiation decreasing towards higher strip numbers indicating the side of the DSSSD being tilted towards the beam axis. Figure 5.6b shows the hit pattern of DSSSD1. It shows similar features as figure 5.6a, but the petal projection was smaller. Together with the higher overall event rate of DSSSD1, a slightly shorter distance to the beam was the reason for this effect. After conversion of the DSSSD strips into metric units (cf. figure 5.7), the features of the DSSSD detectors remain the same. The projection of the petal is 1.5 mm smaller in figure 5.7b than in figure 5.7a. From this difference and the petals front actual size, the distances between petal and DSSSD can be calculated by using the intercept theorem. The calculation yields DSSSD1 being 5 mm closer to the target than DSSSD0. This is a 5% deviation from the nominal position, so it cannot be neglected and will be considered in the following.

To calculate the angular coverage and global positioning some values about the detectors position in the experimental hall need to be known. Figure 5.8 summarizes the known position measures of all detectors in relation to the target point[56]. The measures were taken using a laser measure with 0.1 cm precision. Figure 5.8 a shows the top view with

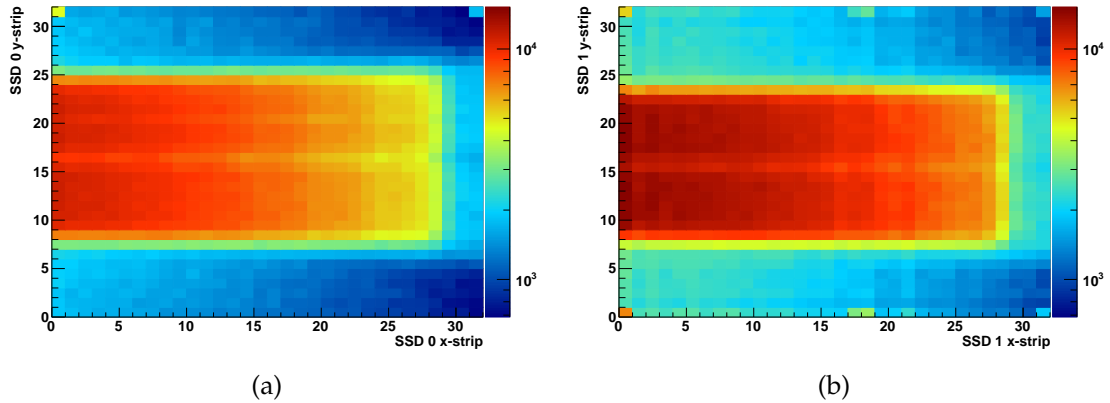


Figure 5.6: Hit pattern of the used DSSSD detectors. Figure a) shows the pattern measured by DSSSD0. Most noticeable feature of the hit pattern is the red shaded rectangle associated with the DSSSD pixel coincident with the petal detector behind it. This feature is observed due to the trigger method used (cf. chapter 3.2.3). The remaining area shows a homogeneous irradiation decreasing towards higher strip numbers indicating the side of the DSSSD being tilted towards the beam. Figure b) shows the hit pattern of DSSSD1. It shows similar features as figure a), but the petal projection is smaller. Together with the higher overall event rate of DSSSD1, a slightly lower distance to the beam could be the reason.

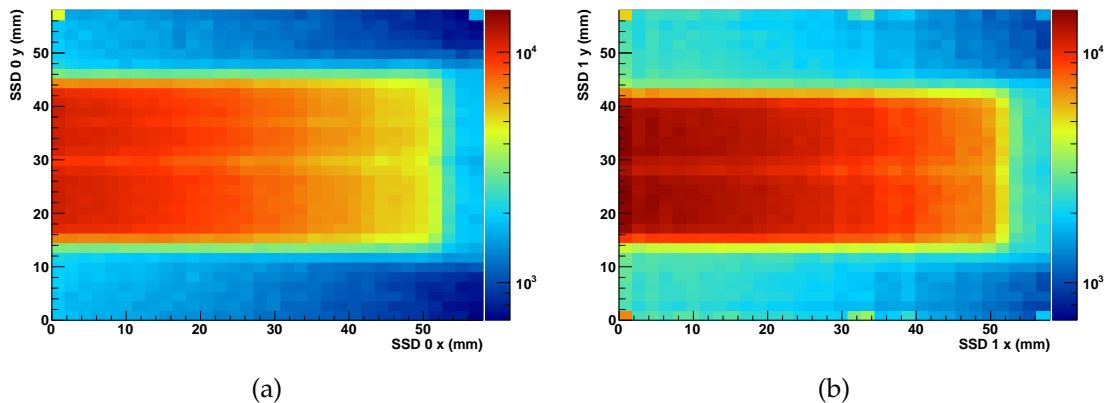


Figure 5.7: Hit pattern of the DSSSDs with the strip number converted to mm. Figure a) shows the the hit pattern of DSSSD0 and figure b) the one of DSSSD1. The features remain unchanged by the conversion as should be expected. The petal projection in figure b) is 1.5 mm smaller than the one in figure a).

all three petals in respect to the DSSSD detectors and the target. Note, that the petal detectors were tilted by 15° and the DSSSDs by 23° with respect to the beam axis. As indicated by the projection, the DSSSD detector does not completely overlap with the petal detectors. Figure 5.8 b shows the setup's front view facing in beam direction. Using trigonometry and geometric relations the distance from the target to all detector units and strips are calculated. An image showing a position reconstruction viewed from above of the strips and crystals is shown in figure 5.9. The distance to the center of the DSSSD was calculated as 9.9 cm (DSSSD0) and 9.4 cm (DSSSD1). The center of the petals was positioned 41 cm from the target. Based on the global position reconstructed here, more sophisticated calibration steps such as the DSSSD's angle calibration were done. Figure 5.10 a shows the DSSSD's x strip correlations with each other as first approach to a polar angle measurement. Most prominent feature was the anti correlation line observed between both DSSSDs. This was associated with the polar angle correlation of the elastic

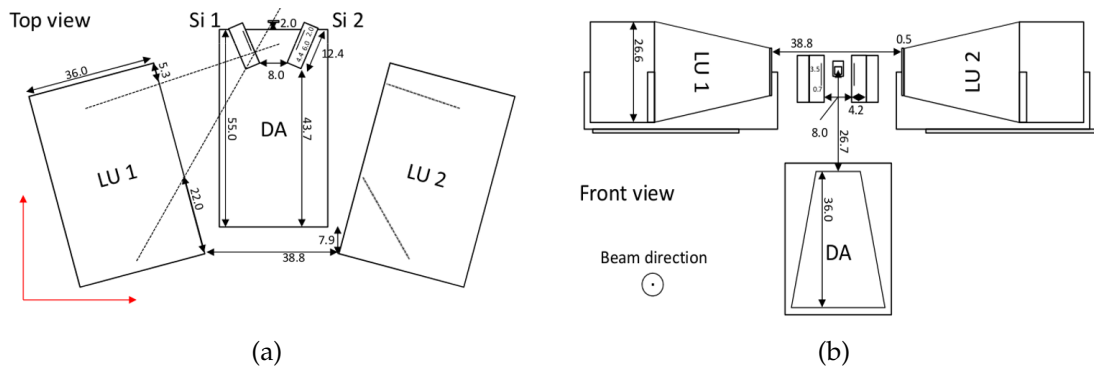


Figure 5.8: A drawing of the setup with all relevant measures in cm with 0.1 cm accuracy (source [56]). Figure a) shows the top view with all three petals in respect to the DSSSD detectors and the target. Note, that the petal detectors were tilted by 15° and the DSSSDs by 23° with respect to the beam axis. As indicated by the projection, the DSSSD detector does not completely overlap with the petal detectors. Figure b) shows the setup's front view facing in beam direction. The measurements represented in this picture are used to calculate polar and azimuthal angle, distance to the target of the detectors and so on.

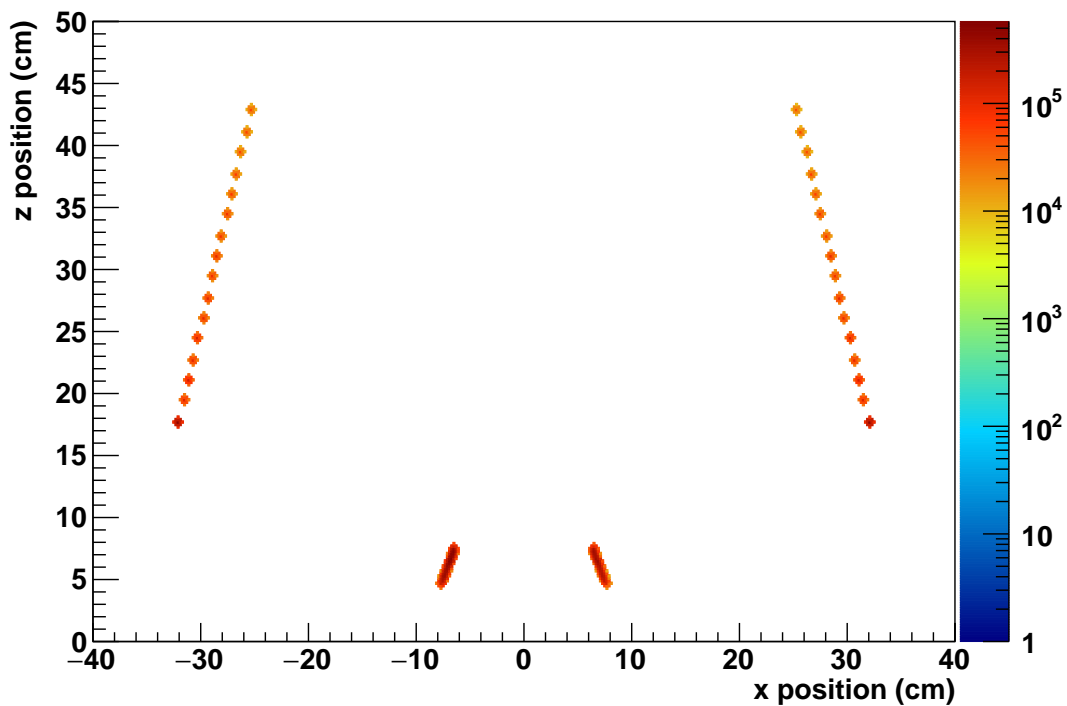


Figure 5.9: Reconstruction of the detectors position in respect to the target with the DSSSDs and petal 0 and 1 displayed in this figure. Based on these, more sophisticated calibration steps such as the DSSSD's angle calibration are done. The distance to the center of the DSSSD can be calculated as 9.9 cm (DSSSD0) and 9.4 cm (DSSSD1). The center of the petals was positioned 41 cm from the target.

scattering. The remaining plot shows a homogeneous event distribution and no further correlations. Using the position information of each DSSSD pixel, the DSSSD data was calibrated to show the detected particles polar emission angle, assuming it was emitted

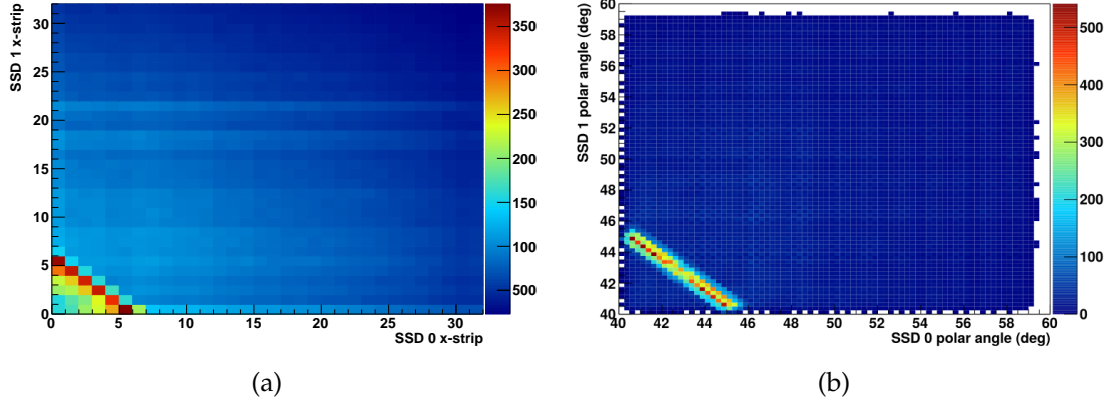


Figure 5.10: Figure a) shows the x strips of DSSSD0 plotted versus the x strips of DSSSD1 to illustrate the polar angle correlation. Between the strips an anti correlation line is observed, indicating a polar angle correlation between two emitted particles. Figure b) shows both DSSSD's coordinates calibrated to the polar emission angle with respect to the target using equation 5.2. Both DSSSD's cover a polar angle range from 40° to 58° . The opening angle of the correlated particles is $\theta_{opang} = (85.8 \pm 0.9)^\circ$.

from the target. This was done using the conversion formula for spherical coordinates:

$$\theta = \arccos \left(\frac{z}{\sqrt{x^2 + y^2 + z^2}} \right) \quad (5.2)$$

where x, y and z were reconstructed using the position information gained from figure 5.8 and the position calibration of the DSSSDs. Applying the calibration to the data results in figure 5.10 b. The anti correlation was still observable as before, so the plot's features were still the same. Both DSSSD's covered a polar angle range from 40° to 58° . The opening angle of the correlated particles was $\theta_{opang} = (85.8 \pm 0.9)^\circ$. Comparing with calculations of the expected opening angle for elastic scattered protons at $E_{beam} = 200$ MeV ($\theta_{opang, sim} = 86.4^\circ$) the results agree with each other within the errors. The same was done accordingly for the azimuthal angle. Figure 5.11 a shows the DSSSD's y strip correlations with each other as approach to a azimuthal angle correlation plot. An anti correlation line through the center of the plot was observed, indicating a symmetric particle emission from the target. Around the center of the plot, the event distribution was stronger than towards the edges as the central strips were closest to the target. The azimuthal angle calibration of the DSSSDs was done in a similar way as for the polar angle only using equation 5.3.

$$\phi = \arctan \left(\frac{y}{x} \right) \quad (5.3)$$

Note, that for implementation the "atan2" function was used to ensure the right quadrant to be used according to the sign of x and y (cf. [57] for details). Figure 5.11 b shows the results of applying the calibration. As expected the general features of the plot did not change. Both DSSSD's cover an azimuthal angle range from -14° to 14° . The opening angle of the correlated particles was $\phi_{opang} = (179.8 \pm 6.7)^\circ$.

5.2 Event selection

After finalizing the calibration, cuts to select on elastic scattering and (p,2p) reactions are presented. To properly define such cuts, one needs to understand the unique kinematics of elastic scattering and the (p,2p) reaction.

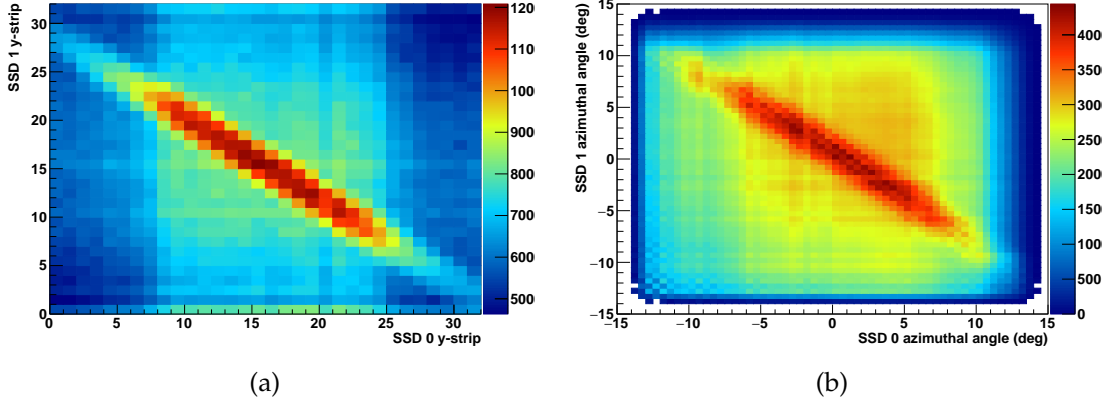


Figure 5.11: Figure a) shows the y strips of DSSSD0 plotted versus the x strips of DSSSD1 to illustrate the azimuthal angle correlation. An anti correlation line through the center of the plot is observed, indicating a symmetric particle emission from the target. Around the center of the plot, the event distribution is stronger than towards the edges as the central strips are closest to the target. Figure b) shows both DSSSD's coordinates calibrated to the azimuth emission angle with respect to the target using equation 5.3. Both DSSSD's cover an azimuth angle range from -14° to 14° . The opening angle of the correlated particles is $\phi_{opang} = (179.8 \pm 6.7)^\circ$.

In the proton-proton elastic scattering reaction, two free protons collide with each other. In case of the experiment presented here, one proton was accelerated to $E_{beam} = 200$ MeV while the other proton rested in the target (more precisely bound in a Polypropylene molecule). As the binding in the molecule ($O(1$ eV)) is negligible compared to the beam energy, the proton in the target can still be considered free. Due to the elastic nature of the scattering and momentum conservation, the beam energy is distributed to both protons depending on the scattering angle of each proton respectively. In a non-relativistic case, the opening angle should be constant and precisely 90° . Due to the Lorentz boost of the center of mass system, the situation is more complicated and the opening angle varies. The azimuth opening angle is expected to be 180° due to back-to-back emission in a two body system.

So the signature of the elastic scattering we expect is the following:

- Only two protons in the exit channel
- Energy correlation between the protons with constant sum energy equals E_{beam}
- Angular correlation with polar opening angle $\leq 90^\circ$
- Angular correlation with constant azimuth opening angle 180°

For the (p,2p) reaction, the signature will be similar, as we also have two correlated protons in the exit channel. Main difference is the target proton being bound in a nucleus with a binding energy $O(10$ MeV), which is compared to the beam energy no longer negligible. This leads to the sum energy of the proton pair in the exit channel to still be constant but smaller than the beam energy. Going from a two-body to a three-body reaction introduces the residual nucleus after the scattering as recipient of recoil momentum. The residual nucleus can be used to tag the reaction in inverse kinematics. The Fermi motion ($\sigma_{pF} \approx 100$ MeV/c) of the proton within the target nucleus creates a smearing of the knocked out protons angular distribution, so the opening angle is no longer fixed (cf. figure 4.1). The azimuth opening angle is expected to be smeared around 180° . This leaves the following event signature.

- Two protons in the exit channel

- Energy correlation between the protons reduced by the binding and recoil energy of each individual state
- Asymmetricly smeared polar opening angle around the average
- Angular correlation with azimuth opening angle smeared around 180°

Using the differences in the event signature regarding angular distribution and sum energy of the detected protons is used to identify and separate both reactions.

5.2.1 Vertex reconstruction

Using the coincidence between the DSSSD and petal on each arm to select particles emitted by the target and passing through the DSSSD and hitting the petal. To get a good representation of correlations the petal columns were plotted against the DSSSD's x-strips (cf. figure 5.12). Here the anti correlation line indicates events emitted from a central

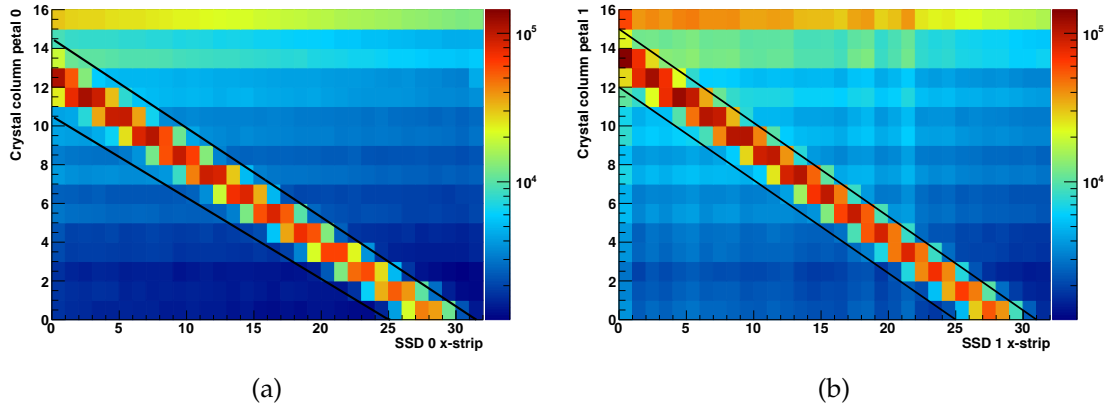


Figure 5.12: Vertex reconstruction histograms for a polypropylene target run with $E_{\text{beam}} = 200$ MeV. Plot a) shows the petal 0 columns plotted against the X strips of DSSSD 0. A correlation between 0 to 14 and the strips 0 to 30 is observable. The cut drawn in black is defined using equation 5.4 to select events emitted from the target. Plot b) shows the same for petal 1 and DSSSD 1. The correlation is observable in this plot as well. Note, that the alignment is slightly different.

point and so were used to select the emission vertex of the protons from the target point. Cutting on this line on both sides (cf. figure 5.12a for petal 0 and figure 5.12b) removes so most of the background stemming from sources other than the target. This was especially important as the whole target and detector setup was operated in air. A cut on the line was done analytically by a simple linear relation:

$$N_{\text{col}} = \frac{N_{\text{col,lim}}}{N_{\text{strip,lim}}} \cdot N_{\text{strip}} + N_{\text{col,lim}} \quad (5.4)$$

where N_{col} is the column number, N_{strip} the strip number and the variables with the "lim" index are the upper or lower limit of either the column or strips used for the cut. For DSSSD0 and petal 0 it is drawn in figure 5.12a. Using this cut on both arms, coincident reactions from the target are selected. As a simple cross check, an empty target run is used for comparison (cf. figure 5.13) of the DSSSD-petal correlation plot. Here the anti correlation line has disappeared due to the dominant source of particles at a single position is missing. The efficiency of the coincident cut extracted from simulations is $\epsilon_{\text{vertex}} = 16.2\%$. This value is rather low, as the overlap of the SDDs and petals in each arm was not perfect and we loose a large fraction of the acceptance.

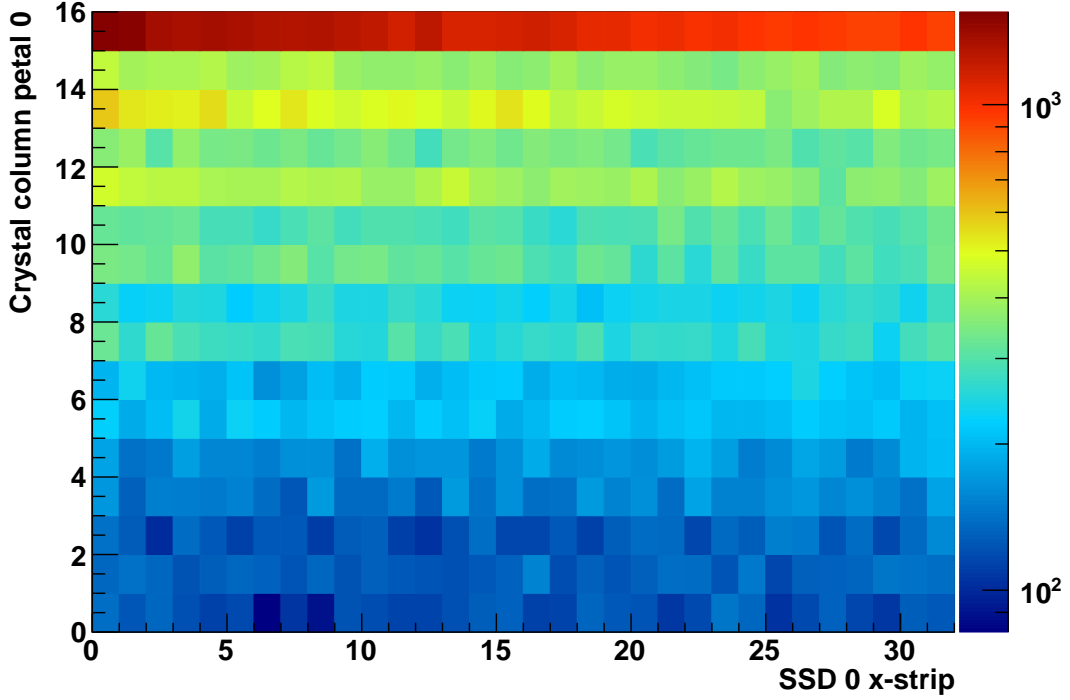


Figure 5.13: Histogram showing DSSSD-petal correlations without target. The anti correlation line observed in figure 5.12 vanished as expected. This behavior proofs the anti correlation belonging to particles emitted from the target location.

5.2.2 Selection of fully stopped protons

For the proper energy reconstruction of each event it is important to select events where both protons had been stopped within the active volume of CsI(Tl), without introducing additional nuclear reactions in the detector material. Using the particle identification (PID) capabilities intrinsic to CsI(Tl) (described in Chapter 2.2) were used to select only protons in both petals. In the following a new method was used by summing up the individual crystal PID amplitudes N_{red} and N_f to generate a overall petal PID plot. This method was advantageous in identifying punch through and stopped particles with energy loss distributed over several crystals. The PID plots for petal 0 and 1 are shown in figure 5.14.

The figure shows the sum PID plot in reduced representation, where the fast component N_f of the scintillation of CsI(Tl) is plotted against the reduced slow component N_{red} defined in section 2.2.4. This representation emphasizes the separation of the branches, labeled in red. In both figures the branches of stopped and punch through protons are separated very well with the threshold visible at 10 MeV. Furthermore deuterons, tritons, ^3He and ^4He were identified as well. These were reaction products either from spallation reactions of the protons with the oxygen content of the target or secondary reactions in the material in front of the CsI(Tl) detectors. The individual peaks contributed to the elastic scattered protons were nicely aligned on the the stopped proton branch in both figures, but the alignment seemed to be slightly better in figure 5.14b than in 5.14a. Selection of the proton branches in the reduced PID plot was done using the following analytical function:

$$N_{red}(N_f)_{\text{stopped}} = A \cdot (\exp(-B \cdot N_f) - 1) \quad (5.5)$$

$$N_{red}(N_f)_{\text{punchthrough}} = A \cdot \exp(-B \cdot N_{f,\text{max}}) \cdot (1 - \exp(B \cdot N_f)) \quad (5.6)$$

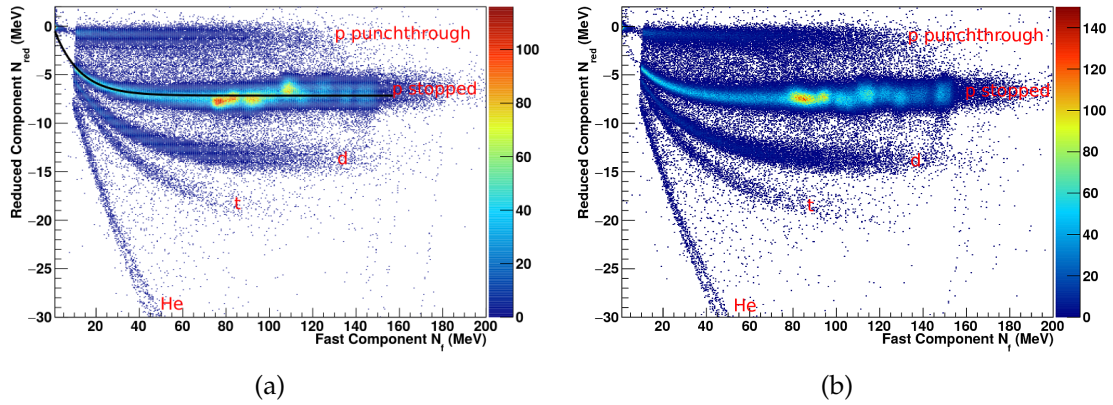


Figure 5.14: Particle Identification (PID) histograms for a polypropylene run with $E_{\text{beam}} = 200$ MeV in reduced representation. Here the individual crystal's PIDs of the petals were summed up. Plot a) shows the PID using petal 0, while plot b) shows the same for petal 1. In both plots several branches are observed, mainly stopped and punch through protons but also heavier particles, like deuterons, tritons and helium can be observed. The multiple peaks on the stopped proton line correspond to the discrete proton energies from the elastic p-p scattering. In figure a) the analytical function (cf. equation 5.6) used for selecting stopped proton events is drawn.

With the empirical variables A and B , and $N_{f,\text{max}}$, representing the end point of the proton branch. These are general functions, that were adapted to any of the branches by choosing suitable values for A, B and $N_{f,\text{max}}$ depending on the crystal length. The analytical cut was then done on a 3σ level to include only the desired particles. In the present case, only the stopped protons were of interest, as the highest energy a scattered proton had is $E_{\text{beam}} = 200$ MeV. The energy a proton would need to punch through the shortest crystal in the petal (17 cm) is 274 MeV^1 . As all scattered protons entering the petals had a lower energy, it was reasonable to select stopped protons at this point. Using the PID cut on stopped protons on both arms, was an effective way for a two proton coincidence cut, demanding the first event condition. The efficiency of the PID cut was calculated by selecting the punch through proton branch and looking a pair of elastic scattered protons in the petal energy correlation plot. These events were missed by the PID cut on stopped protons in the petal, reducing the efficiency. In figure 5.15 a cut on the punch through proton branch is shown together with a cut on energy correlation of petal 0 and 1. Counting the events identified as punch throughs by the PID in figure 5.15 a, but showing the two proton correlation associated with elastic scattering in figure 5.15 b, the efficiency of the PID cut is calculated to be $\epsilon_{\text{PID}} = 99.8\%$.

5.2.3 Selection of correlated pairs

Three classes of events namely, elastic scattering (1), (p,2p) events (2) and background from reactions with heavy nuclei (3), formed by correlated pairs need to be separated as described in the event signature stated in section 5.2. The selection criteria are the following:

1. fixed polar and azimuth opening angle (elastic)
2. certain polar and azimuth opening angle (p,2p)
3. random polar and azimuth opening angle (heavy reactions)

¹Calculated with Lise++

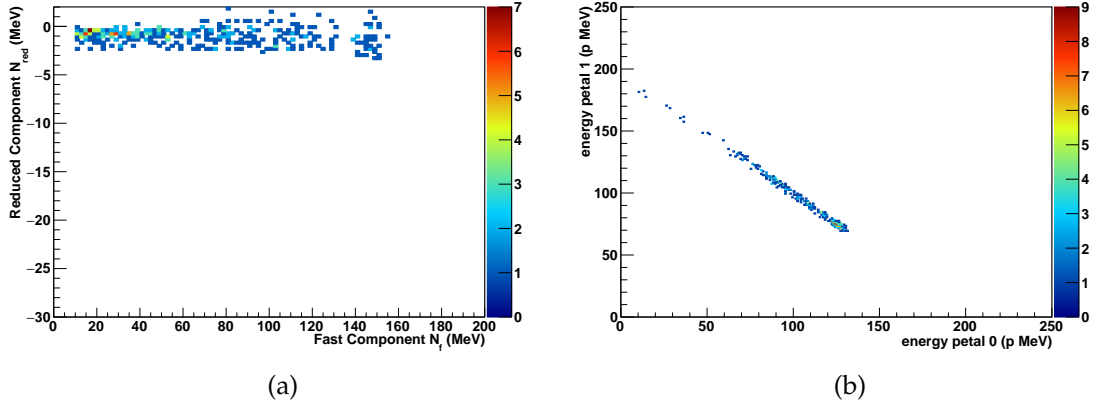


Figure 5.15: Figure a) shows the a PID sum plot with selection on the proton punch through branch and the two proton energy correlation. Since the elastic protons should be stopped in the petal detectors no events should be observed in either figure. Events observed were misidentified by the PID and used to determine the efficiency. 389 events are observed on the elastic proton anti correlation line in figure b).

Last but not least, a selection on the polar opening angle was done by the already in figure 5.10 seen DSSSD correlation plot. There an anti correlation was observed between the polar angle of detected particles to select just the elastic scattering events. The most convenient method of doing a selection on the anti correlation in the polar angle plot was using a linear relation in the following form:

$$\theta_1(\theta_0) = -\theta_0 + \theta_{0,\text{lim}} \quad (5.7)$$

where $\theta_{0,1}$ are the reconstructed polar emission angles and $\theta_{0,\text{lim}}$ the upper and lower limit of the opening angle cut's width. The cut used here is illustrated in figure 5.16. The efficiency of the polar opening angle cut was $\epsilon_{\text{opang}} = 90.3\%$. This value was limited by the resolution of the DSSSD detectors. Note, that this cut was obsolete in the selection process of (p,2p) event selection and only the two proton and vertex cut were used. As a removal of the elastic scattering events in water target data was necessary, the polar opening angle cut was inverted to exclude elastic scattering events.

Applying the vertex, PID and opening angle cut on the raw data from the polypropylene target to select the elastic scattered protons results in figure 5.21. Comparing this to figure 5.5 the differences were easily observed. Most of the background structure from sources other than the target were gone, leaving only the anti correlation line associated with the elastic proton scattering. As the DSSSD's overlap with the petals was limited in both arms, the line in figure 5.17a was shorter due to losing part of the polar angular coverage. The improvement was also observed in figure 5.17b as the signal to background had increased strongly. In addition the low energy tail of the total energy peak was strongly suppressed. Looking at the energy resolution it increased to $\frac{\Delta E}{E} = 1.2\%$. This is the resolution of two protons detected simultaneously in both petal detector modules at 200 MeV. As we were interested in the individual petal resolution at 100 MeV to compare the resolution to CALIFA requirements some considerations were necessary. The sum resolution of independent protons is given by the quadratic sum of the individual resolutions of each petal. As the energies of the protons were comparable (100 MeV) in each petals, the assumption of their energy resolution being the same is valid.

$$\frac{\Delta E}{E}_{\text{sum}} = \sqrt{\left(\frac{\Delta E}{E}\right)_{p0}^2 + \left(\frac{\Delta E}{E}\right)_{p1}^2} \approx \sqrt{2 \cdot \left(\frac{\Delta E}{E}\right)_p^2} \quad (5.8)$$

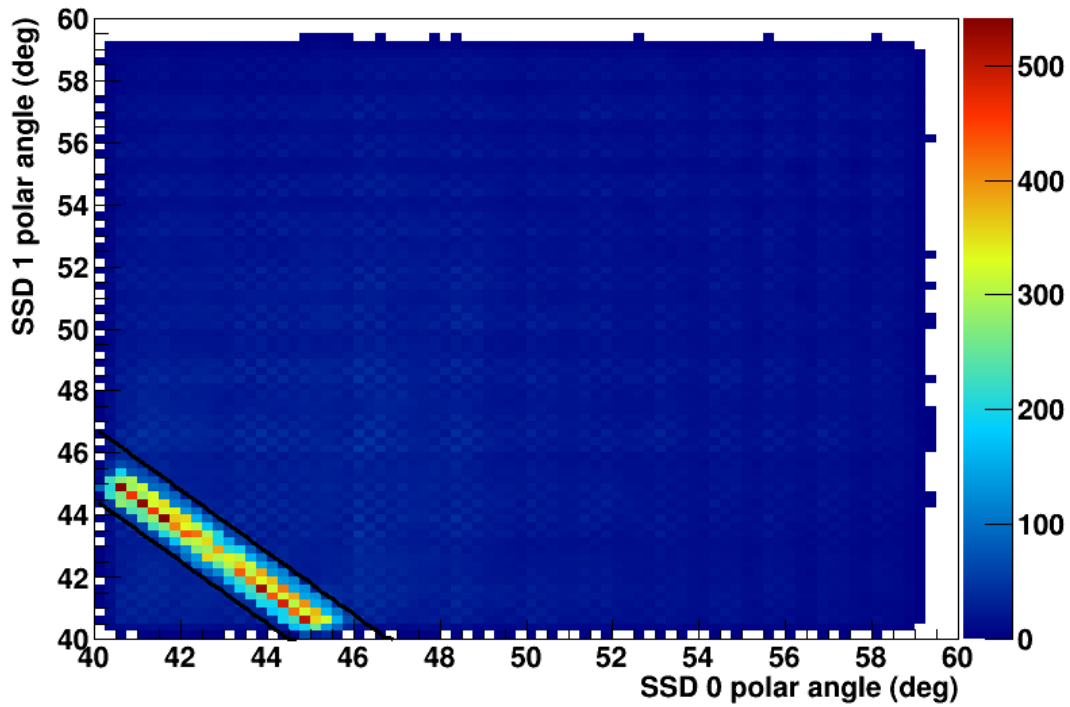


Figure 5.16: Histogram showing polar angle correlation for a polypropylene target run with $E_{beam} = 200$ MeV with a cut on the polar angle correlation associated with the elastic scattered protons. The cut is done analytically as described in equation 5.7.

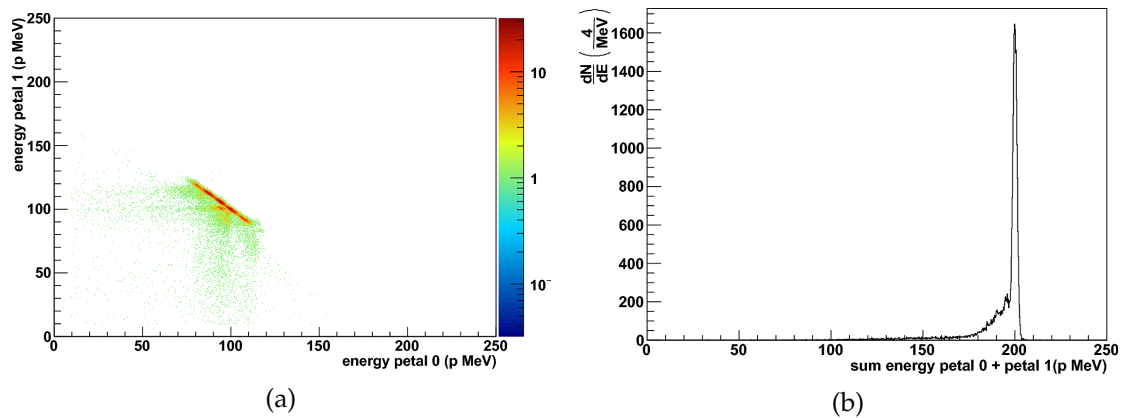


Figure 5.17: Selection on elastic proton events using the vertex, PID and opening angle cuts from a data set taken with a monoenergetic proton beam $E_{beam} = 200$ MeV on a polypropylene target. Figure a) shows the energy correlation plot between petal 0 and petal 1. Compared to figure 5.5, most of the background is removed and the anti correlation line associated with the elastic scattered protons remains. Note, that due to the limited overlap of the DSSSD and petal detectors, the anti correlation line shortens. Figure b) shows the sum energy of both petals. The sum peak associated with the elastics is still observed with an increased signal to background ratio compared to 5.5. The total energy resolution after the cuts increases to $\frac{\Delta E}{E}$ (FWHM) = 1.2%.

Equation 5.8 shows the individual petal resolution $(\frac{\Delta E}{E})_p$ can be calculated through a division by $\sqrt{2}$ resulting in this measurement in a resolution of 0.8%(FWHM). On the other hand, to scale the resolution to 100 MeV the equation 5.9 is used with a as the individual

petal resolution.

$$\frac{\Delta E}{E}(100 \text{ MeV}) = \frac{a \cdot \sqrt{200 \text{ MeV}}}{\sqrt{100 \text{ MeV}}} = \sqrt{2} \cdot a \quad (5.9)$$

In this case these two operations exactly cancel each other, meaning we were left with a individual petal resolution 1.2% (FWHM) at 100 MeV for stopped protons. As we have thus established the working condition of the presented cuts with expected behavior, the next session will be dedicated to the analysis of (p,2p)-event data.

5.3 Quasi-free scattering on Oxygen

As we now have the proper selection of the events done, applying those to data generated by the water target is the next step. First using the intrinsic self calibration capability of the water target, the elastic scattering on the hydrogen atoms in water is used to compare cut results to the ones from the polypropylene target. In figure 5.18 a petal energy correlation plot shows raw data from all water target runs combined with $E_{\text{beam}} = 200 \text{ MeV}$. The elastic

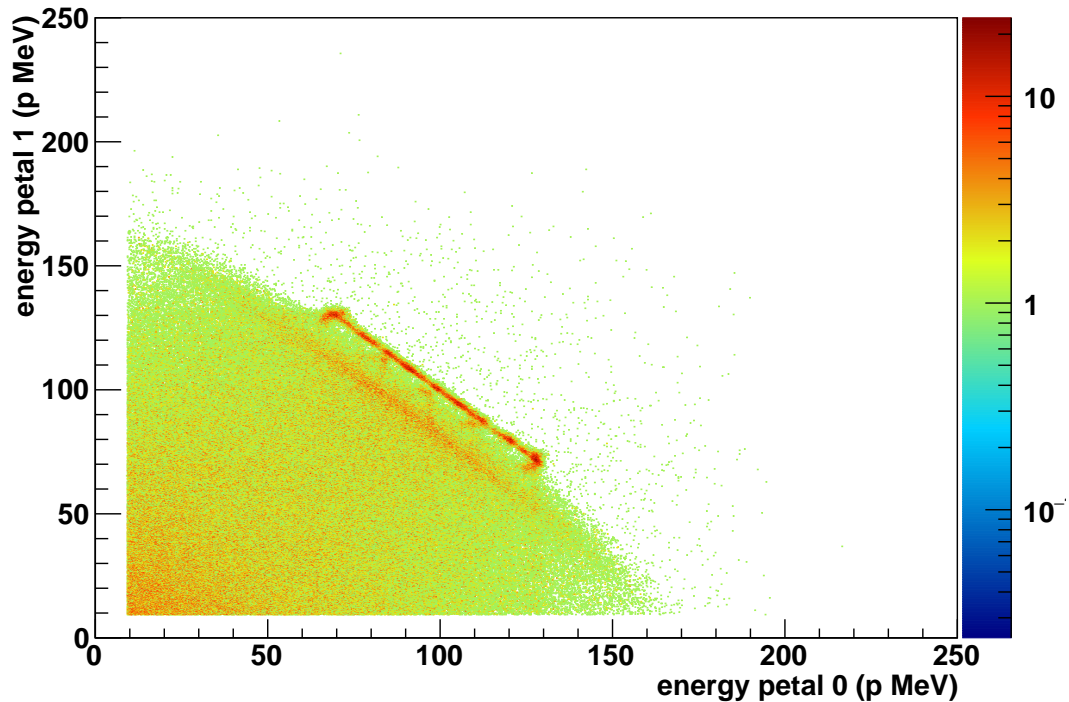


Figure 5.18: Raw data from combined runs with monoenergetic protons $E_{\text{beam}} = 200 \text{ MeV}$ irradiating the water target. The elastic scattering visible by the anti correlation between the deposited energy in petal 0 and 1 are clearly distinguishable. Being similar to figure 5.3a indicates the p,2p signal being being by background from non-target reactions.

scattering identified by the anti correlation between the deposited energy in petal 0 and 1 are clearly visible. Being similar to figure 5.3a indicates the (p,2p) signal is overlapped by background from non-target reactions. To isolate the elastic scattering, the vertex, PID and opening angle cut described in the previous section are applied to the water target data resulting in figure 5.19. In 5.19a the deposited energy in petal 0 and 1 is plotted against each other. As the acceptance is now limited to the DSSSDs due to the cuts, the anti correlation line shortens. Additionally most of the background is now removed leaving an almost clean spectrum. Note the vertical and horizontal distribution leading

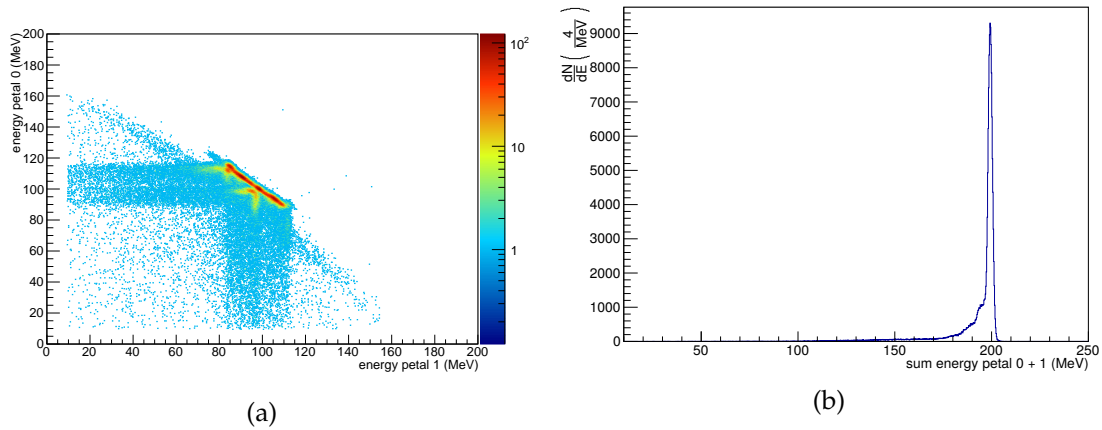


Figure 5.19: Data from combined runs with monoenergetic protons $E_{\text{beam}} = 200$ MeV irradiating the water target with vertex and opening angle cut. In a) their deposited energy in petal 0 and 1 is plotted against each other. As the acceptance is now limited to the DSSSDs due to the cuts, the anti correlation line shortens. Additionally most of the background is now removed leaving an almost clean spectrum. Note the vertical and horizontal distribution leading toward the anti correlation line, where the energy was measured only in one of the petals correctly due to reactions within the CsI(Tl) detector. Plot b) show the sum of both petals for these cuts. The full energy peak is clearly separable from the background with an energy resolution of 1.2%.

toward the anti correlation line, where the energy was measured only in one of the petals correctly due to reactions within the crystal high reflectivity wrapping. As the reaction causing the energy loss in the foil produces stopped protons indistinguishable from target reactions, the PID cut is unable to separate them from the elastic scattering. Close to the anti correlation line a faint shadow of the $p,2p$ events is visible, spanning almost the whole energy range of the petals. This is the fraction of $(p,2p)$ events within the same opening angle distribution as expected from the free scattering. Also next to the anti correlation line, a secondary peak structure is visible. From simulations we learned the origin of these peaks being reactions in the CsI(Tl) crystal wrapping. Figure 5.19b show the sum of both petals for these cuts. The full energy peak is clearly separable from the background with an energy resolution $\frac{\Delta E}{E} = 1.2\%$ (FWHM) at 198.5 MeV. Compared to the data from the polypropylene target we measure the same resolution for the elastic scattered protons originating from the water target. This is certainly expected, but shows how well both runs compare. After establishing the validity of the calibration and the working condition of the cuts for the elastic scattering on the hydrogen atoms in the water target, the next step is separating the QFS events. As selection of the elastics was specifically done by selection of the unique polar angle correlation, a separation is achieved by excluding these events by inverting the elastic proton selection cut. Result of this procedure is shown in figure 5.20. Both plots show the deposited energy correlation between petal 0 and 1 after separating the QFS protons from the rest of the data. Due to the Fermi momentum of the knocked out proton, the angular correlation is smeared out, leading to bands visible. Note that both bands are slightly bent by the difference in energy loss for both protons respectively, where the lower energy proton undergoes a larger energy loss before reaching the active volume. Due to the strong velocity dependence of this process also the total energy is slightly changed at a large energy asymmetry. In figure 5.20b this is compensated by the heuristic equation 4.1 based on Geant4 simulations. Comparing to the simulation in chapter 4 those two energy band can be identified as the $\frac{1}{2}^-$ ground state and a $\frac{3}{2}^-$ excited state (6.3 MeV) of ^{15}N . So this concludes the separation of QFS protons from the two most prominent states visible. This is even better illustrated by looking at the energy sum of petal 0 and 1 as shown in figure 5.20a. The energy spectrum shows a

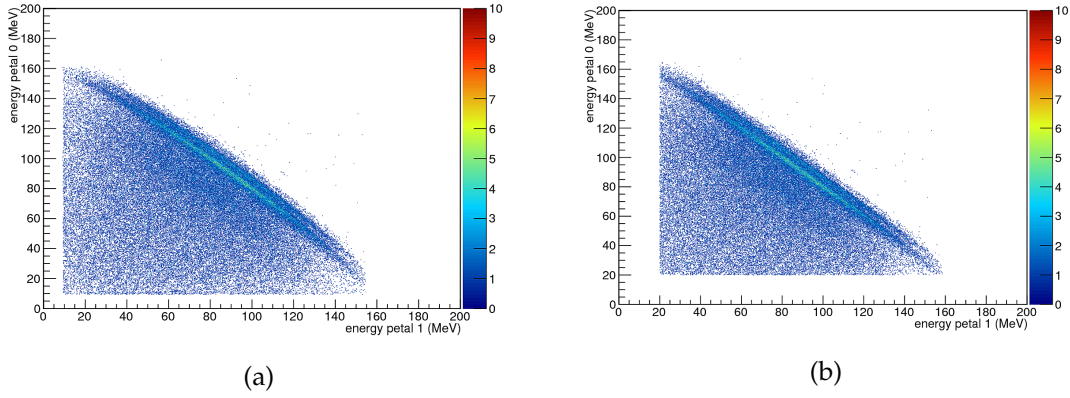


Figure 5.20: The correlations between the energy deposited in petal 0 and petal 1 for all water target runs combined at $E_{\text{beam}} = 200$ MeV. Figure a) shows the data after isolating the QFS protons from the rest of the data. Due to the Fermi momentum of the knocked out proton, the angular correlation is smeared out, leading to two energy bands visible in the plot over the whole energy range. Both lines are slightly bent by the difference in energy loss for both protons respectively. In figure b) this is compensated for analogous to the simulation data using equation 4.1.

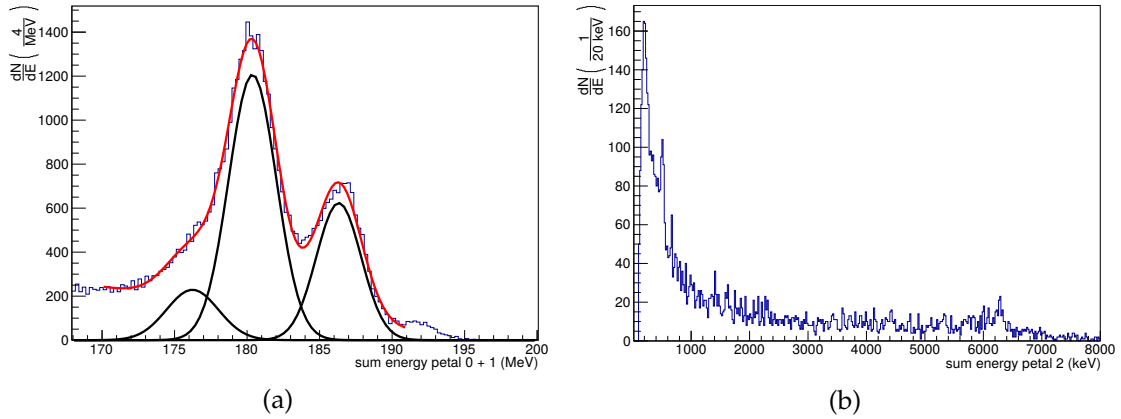


Figure 5.21: Figure a) shows the sum energy of the protons detected in petal 0 and 1. Using a combined fit of three Gaussian functions with linear background (red curve) three peaks (black curves) can be observed corresponding to the ground state at 186.3 MeV, the 6.3 MeV excited state at 180.3 MeV and the 9.9 MeV excited state at 176.2 MeV. With a proton separation energy for ^{16}O $E_s = 12.13$ MeV[46], the calculated separation energy $E_{s,meas} = (12.22 \pm 0.02)$ MeV is consistent with each other. A resolution of $\frac{\Delta E}{E}$ (FWHM) = 1.9%(GS), $\frac{\Delta E}{E}$ (FWHM) = 2.1%(6.3 MeV) and $\frac{\Delta E}{E}$ (FWHM) = 2.3%(9.9 MeV) was achieved. Note the small peak adjacent to the ground state resulting from elastic proton events surviving the p,2p event selection. Figure b) shows coincident events detected in petal 2 as excitation γ -ray candidates. The full energy peak at 6.3 MeV (red) is observed above the background. Also the 511 keV (green) is visible ($\frac{\Delta E}{E}$ (FWHM) = 9%).

zoomed in section onto two peaks well above the background with a tail towards smaller energies. As the beam energy reaching the target is $E_{\text{beam},t} = 198.52$ MeV² and the proton separation energy of ^{16}O is $E_s = 12,13$ MeV[46], the peak corresponding to the ground state should be found at 186.39 MeV in figure 5.21a. From the position of the ground state peak, the separation energy can be calculated to $E_{s,meas} = (12.22 \pm 0.02)$ MeV, which is consistent with the literature value. Using the combined fit of three Gaussian function and with a linear background, the positions of three peaks can be identified. The first

²calculated with Lise++

peak at 186.3 MeV is identified then, as the considerations before suggest, as the ground state contribution. At 180.3 MeV and 176.2 MeV the peaks corresponding to the 6.3 MeV and 9.9 MeV excited states of ^{15}N respectively. Note the additional small peak adjacent to the ground state peak resulting from elastic scattering events surviving the p,2p event selection. The energy resolution of the peaks are $\frac{\Delta E}{E}$ (FWHM) = 1.9%(GS), $\frac{\Delta E}{E}$ (FWHM) = 2.1%(6.3 MeV) and $\frac{\Delta E}{E}$ (FWHM) = 2.3%(9.9 MeV). Compared to the resolution of the elastic scattered protons $\frac{\Delta E}{E}$ (FWHM) = 1.2%, the resolution of the QFS protons is worse than expected. According to the kinematic simulation discussed in chapter 1.2.3, the residual nucleus' recoil momentum plays also a role here. Depending on this momentum transfer the recoil nucleus already carries a significant fraction of the total energy. As figure 4.1 b) illustrates, this leads to a broadening of the total energy measurement of 1% (FWHM). To consider this effect, the raw detector resolution needs to be reconstructed by the equation $\frac{\Delta E}{E}_{detector} = \sqrt{\left(\frac{\Delta E}{E}\right)_{measured}^2 - \left(\frac{\Delta E}{E}\right)_{recoil}^2}$. The raw detector resolution of the peaks is then $\frac{\Delta E}{E}$ (FWHM) = 1.6%(GS), $\frac{\Delta E}{E}$ (FWHM) = 1.8%(6.3 MeV) and $\frac{\Delta E}{E}$ (FWHM) = 2.1%(9.9 MeV). This still does not reach the resolution achieved for elastic scattering. The difference can be accounted for by the difference in emission angle of the protons from the target causing longer paths through passive material, increasing energy loss straggling. This effect was completely accounted for through the proton calibration process for elastic scattered proton pairs, but could only be partially accounted for the (p,2p) proton pairs. As this caused only a small deviation the effect is not concerning, but still needs to be kept in mind for future experiments.

5.3.1 Particle- γ -correlations

With the QFS protons selected using petals 0 and 1, looking at the coincident events in petal 2 is the next step in search of γ -radiation from the excited states (cf. figure 5.21b). A peak (red) is observed in the region of 6.3 MeV above the background, the 511 keV line (green) is observed as well. To investigate the emitted γ radiation further, different proton sum energy windows can be defined as illustrated in figure 5.22a. Three energy selection windows for a detailed investigation of the coincident γ -rays are illustrated on the plot. Figure 5.22b shows the selection on the two protons indicating a population of the 6.3 MeV excited state of ^{15}N (window 2). In the γ -ray spectrum a 6.3 MeV peak is nicely separated from the background after applying this cut. Due to Bremsstrahlung and secondary Compton scattering the 6.3 MeV peak's Compton edge is smeared out and no single or double escape peak can be clearly identified. The resolution achieved is $\frac{\Delta E}{E}$ (FWHM) = 2% at 6.3 MeV. Figure 5.22c shows the γ -ray spectrum using a kinematic selection on the ground state (window 1). Populating the ground state no γ -ray will be emitted, the figure illustrates the background present during the experiment. Also a few events are visible in the region of 6.3 MeV due to the peaks being not perfectly separated in figure 5.22a. Last but not least figure 5.22d shows the selection on higher excited states (window 3). No clear lines remain except for the 511 keV line. Some feed down from higher excited states attributes to the bump structure at 6.3 MeV. The 9.9 MeV line is not observed in any of the figures b) to d). This is mainly due to the probability to populate the 9.9 MeV excited state is a factor of 5 smaller than the population of the ground state or the 6.3 MeV excited state. Furthermore the 9.9 MeV state has a 68% branching into the ground state transition. At this energies the Bremsstrahlung and Pair production reduce the γ -ray detection efficiency significantly due to not having a full calorimeter at our disposal. Another important benchmark is of course the γ detection efficiency. As described in the simulation chapter, the number of events in the QFS proton peak corresponding to the 6.3 MeV excitation in ^{15}N deexcited with emission of exactly one γ -ray. Counting the number of events in the γ peak in petal 2 the overall γ detection efficiency of one

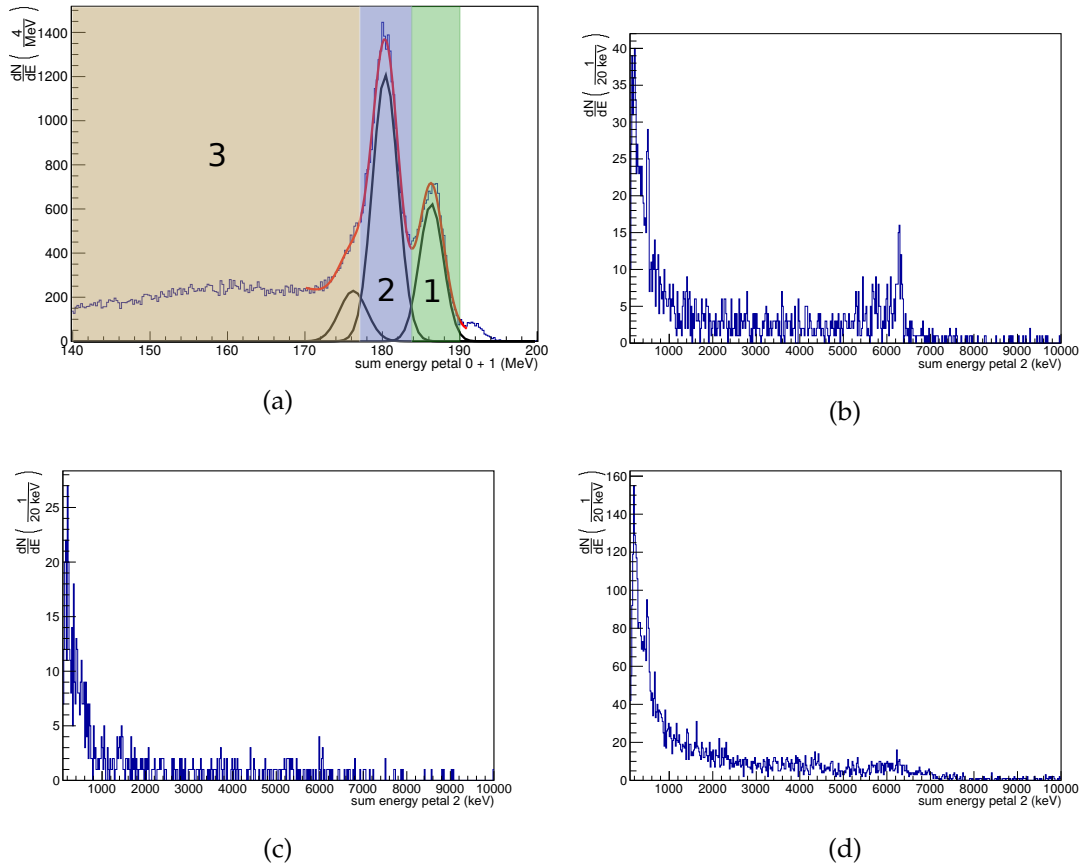


Figure 5.22: Figure a) shows a section of the proton sum energy plot. Three energy selection windows for a detailed investigation of the coincident γ -rays are illustrated on the plot. Window 1 selects coincidents with the ground state, window 2 coincidence with the 6.3 MeV excited state and window 3 coincidence with higher excited states (s-hole). Figure b) shows selection on the 6.3 MeV excited state of ^{15}N (window 2). The 6.3 MeV peak is nicely separated from the background after applying this cut. Due to Bremsstrahlung and secondary Compton scattering the 6.3 MeV peak's Compton edge is smeared out and no single or double escape peak can be clearly identified. The resolution achieved is $\frac{\Delta E}{E}$ (FWHM) = 1.95%. Figure c) shows the γ -ray spectrum using a kinematic selection on the ground state (window 1). Populating the ground state no γ -ray will be emitted. The figure illustrates the background present during the experiment. Also a few events are visible in the region of 6.3 MeV due to peaks being not perfectly separated in figure a). Last but not least figure d) shows the selection on higher excited states (window 3). No clear lines remain except for the 511 keV line. Some feed down from higher excited states attributes to the bump structure at 6.3 MeV. The 9.9 MeV line is not observed in any of the figures b) to d). Also no background subtraction was done in any of the figures.

petal can be calculated. From simulations we know the geometrical coverage of petal 2 is 9.6%. Using only the events in the full energy peak, the calculated efficiency is $\epsilon = (0.99 \pm 0.09)\%$, taking all events in the estimated single and double escape peak region as well, the efficiency increases to $\epsilon = (2.40 \pm 0.13)\%$. This value is in the order of magnitude expected from simulations ($\epsilon_{sim} = 3.1\%$). To increase the setups γ efficiency petal 0 and 1 can be considered for γ detection. As the petals were in particle mode, thus having a gain by a factor of 11 lower, performing a γ separation here is also an important test in regards of CALIFA performance. As petal 2 was closer to the target than petal 0 and 1, this reduced the detection capability by 63.3%. Additionally the crystals with energy deposition by the QFS protons need to be removed, leaving only 86% of the petal active for γ detection. Together this reduces the expected γ -ray efficiency to 54.4%. Considering

this calculation, of 327 γ events detected in petal 2, only 178 would be expected in full energy, single escape and double escape peak together. To achieve an γ isolation, the crystal with the proton signature was identified and to get rid of all light crosstalk, the eight surrounding crystals are left out of the energy sum as well. The remaining crystals should only contain energy depositions coincident to the QFS proton event. Figure 5.23 shows the result of the γ isolation in petal 0 and 1. A small bump in the 6.3 MeV region

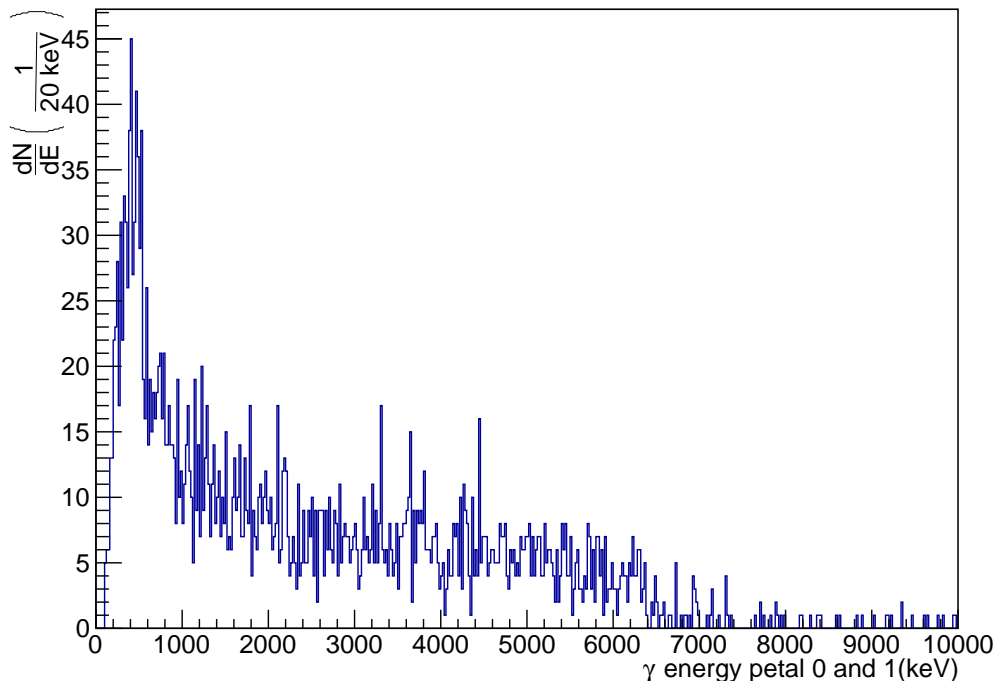


Figure 5.23: The figure shows a γ -ray spectrum of petal 0 and 1 coincident with the population of the 6.3 MeV state of the ^{15}N nucleus. A small bump at 6.3 MeV indicates the excitation γ -rays with no clear peak observable. Due to efficiency loss from isolating the particle hits in petals 0 and 1, the γ -ray add back does not work as in petal 2. Also secondary radiation from δ -electrons in the detector material smears out the full energy peak. This underlines the need for cluster finding algorithm for CALIFA.

indicates the excitation γ -rays with no full energy peak observable. Due to efficiency loss from isolating the particle hits in petals 0 and 1, the γ -ray add back does not work as in petal 2. This underlines the need for specialized γ -cluster-finding algorithms in the CALIFA calorimeter to reconstruct γ -events more precisely (part P.Klenze's PhD thesis). Also secondary radiation from δ -electrons in the detector material smears out the full energy peak. With a total of 318 events, the detection efficiency increases to $\varepsilon = (4.7 \pm 0.19)\%$. Using a full scale simulation of CALIFA³ results for 6.3 MeV γ -rays in a detection efficiency $\varepsilon = 40.8\%$. All these results are summarized in table 5.1. Considering only using three petal detectors, a detection efficiency of almost five percent at 6.3 MeV is already a very promising result.

5.3.2 Momentum distribution and excitation energy

To compare the direct measurement of the excitation energy using petals 0 and 1, it is also possible to use the missing mass spectroscopy method to reconstruct the excitation energy

³done using the R3Broot framework

	N_{peak}	$N_{E>5\text{MeV}}$	ϵ_{peak}	$\epsilon_{E>5\text{MeV}}$	ϵ_{sim}	ϵ_{CALIFA}
Petal 2	134	327	$(0.99 \pm 0.09)\%$	$(2.40 \pm 0.13)\%$	2.6%	40.8%
total	217	654	$(1.60 \pm 0.11)\%$	$(4.8 \pm 0.2)\%$	5.0%	40.8%

Table 5.1: Summary of γ efficiency calculations

by measuring the 4-momenta of the emitted QFS protons. As in inverse kinematics the

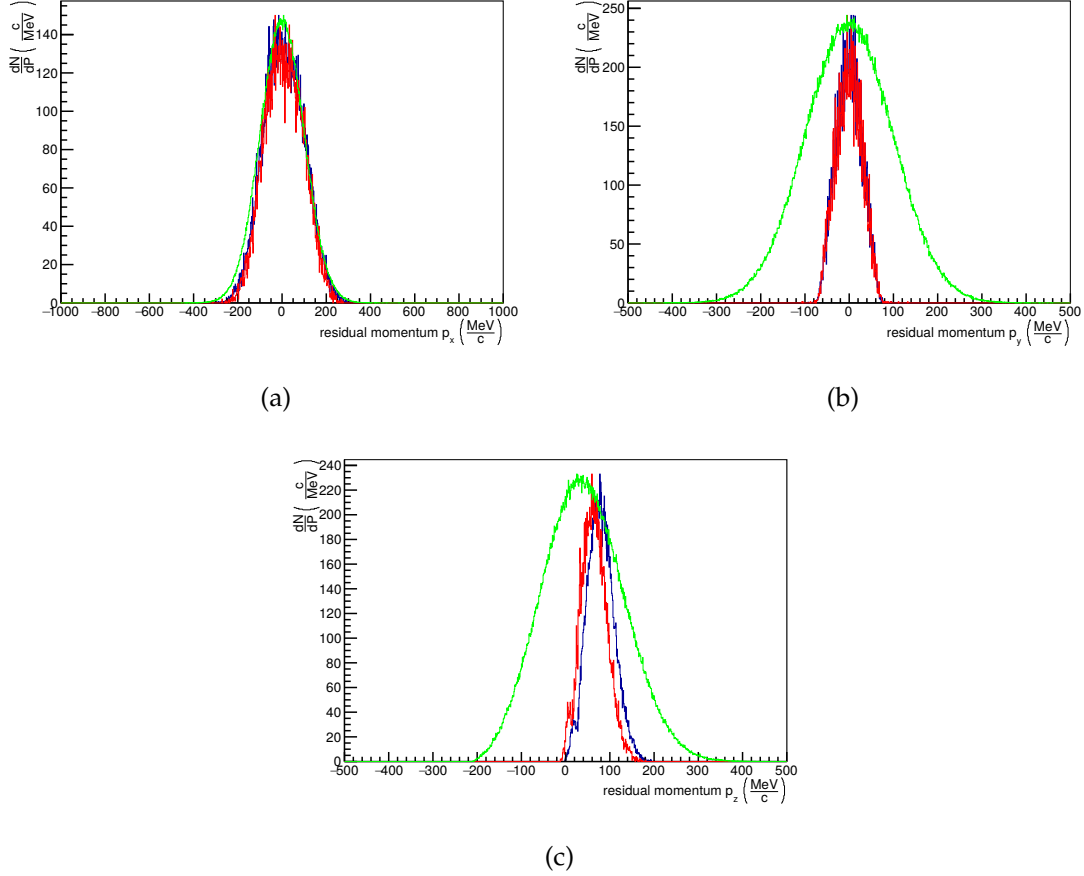


Figure 5.24: Residual momenta of the ^{15}N nucleus for the ground state (blue), 6.3 MeV excited state (red) and a kinematic simulation of the ground state with $\sigma_{p_F} = 100$ MeV (green). Figure (a) shows the residuals momentum in x dimension P_x . All three histograms agree with each other, with the simulation having a slightly larger width. In figure (b) the distribution of the momentum P_y measured in the experiment is dominated by the setups acceptance and is narrower than the simulated distribution. The lacking geometric coverage of the setup in azimuthal direction dominates the spectral shape. Figure (c) displays the residual momentum distribution P_z . While the experimental data is restricted by the experiments geometrical acceptance to only the positive part of the momentum distribution, the simulation shows a asymmetric distribution around $P_{z,\text{max}} \approx 26$ MeV/c with a tail towards positive momenta. The central position of the ground state momentum is shifted to $P_{z,\text{GS,max}} \approx 60$ MeV/c, while the excited state distribution is even shifted to $P_{z,\text{GS,max}} \approx 78$ MeV/c. This indicates larger excitations of the residual nucleus being correlated to a shift in the residual's P_z towards larger momenta.

proton's energy was smeared by the Fermi momentum, a direct measurement in CALIFA is out of the question and for comparability with future inverse kinematics experiments, it is imperative to reconstruct the excitation energy using Missing Mass method as well. In the experiment, the DSSSD detectors are used to supply a better measurement of the polar

(Θ) and azimuth(φ) emission angle of the protons. Through these and the measured energy the residual 4 momentum Q was calculated as described in chapter 1.2.3. This residual momentum is shown in figure 5.24. For comparison, residual momenta reconstructed for the ground state (blue), 6.3 MeV excited state (red) and a kinematic simulation of the ground state with $\sigma_{p_F} = 100$ MeV (green) are shown. As the proton mass was low compared to the mass of ^{16}O the momentum distribution was dominated by the Fermi momentum of the knocked out proton before the reaction. Figure 5.24 a) shows the residuals momentum in x dimension P_x . This momentum component is Gaussian distributed around 0, with all three distributions agreeing with each other. This indicates a low dependence of the momentum measurement in x -dimension on the setups acceptance and excitation energy. Looking at figure 5.24 b) containing the distribution of the momentum P_y , the experimental data's distributions agree with each other, but differ from the simulation. The lacking geometric coverage of the setup in azimuthal direction dominates the spectral shape of the residual's momentum in y dimension, but seemed to be insensitive on the excitation energy. Figure 5.24 c) displays the residual momentum distribution P_z . While the experimental data is restricted by the experiments geometrical acceptance to only the positive part of the momentum distribution, the simulation shows a asymmetric distribution around $P_{z,\text{max}} \approx 26$ MeV/ c with a tail towards positive momenta. The central position of the ground state momentum was shifted to $P_{z,\text{GS,max}} \approx 60$ MeV/ c , while the excited state distribution was even shifted to $P_{z,\text{GS,max}} \approx 78$ MeV/ c . This indicates larger excitations of the residual nucleus being correlated to a shift in the residual's P_z towards larger momenta. From the now known 4 momentum Q and the residual's rest mass the excitation energy is calculated by $E_{\text{exe}} = Q^2 - M_{\text{RESIDUAL}}$. In figure 5.25 the excitation energy spectra created by direct

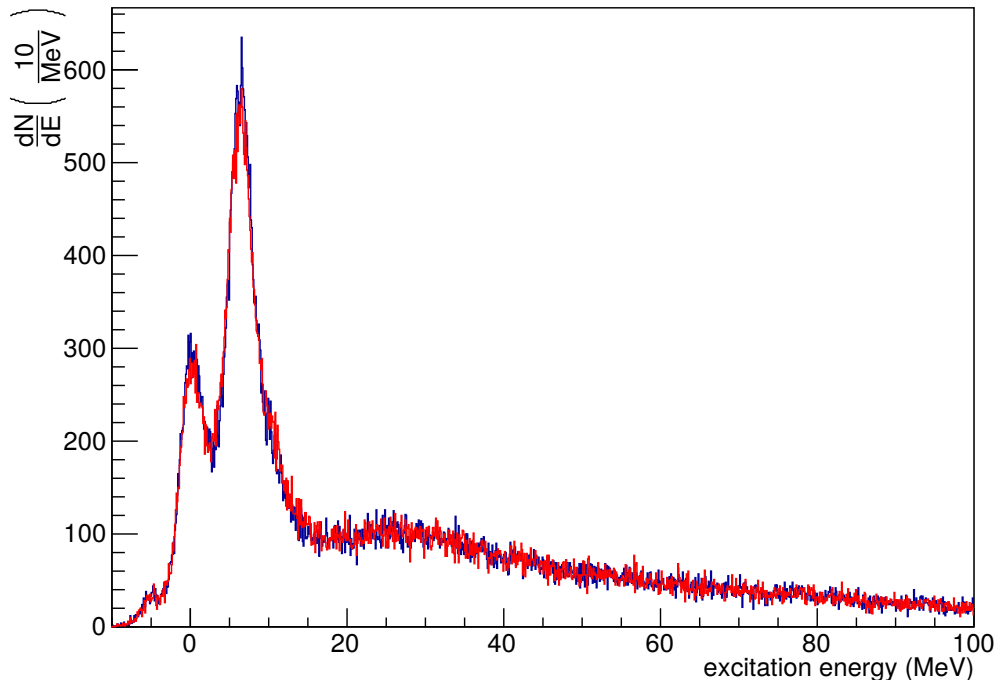


Figure 5.25: Comparison of the excitation energy measured directly (blue histogram) and the excitation energy calculated by missing mass spectroscopy (red histogram). Both methods create exactly the same spectra, making them equivalent, as should be expected. In total the ground state and two excited states at 6.3 MeV and 9.9 MeV are identified next to the tail towards larger excitation energies associated with s -hole states. The width of the excited states is determined to $\sigma_{\text{gs}} = 1.8$ MeV, $\sigma_{6.3 \text{ MeV}} = 1.6$ MeV and $\sigma_{9.9 \text{ MeV}} = 2.0$ MeV

measurement and missing mass spectroscopy are compared. Position and resolution in both plots are in perfect agreement showing both methods being equivalent. The excitation energy's sigma width of the three identified peaks is $\sigma_{gs} = 1.3 \text{ MeV} (\frac{1}{2}^-)$, $\sigma_{6.3 \text{ MeV}} = 1.4 \text{ MeV} (\frac{3}{2}^-)$ and $\sigma_{9.9 \text{ MeV}} = 1.5 \text{ MeV} (\frac{3}{2}^-)$. The width of the 9.9 MeV line is difficult to determine as it is almost completely absorbed by the 6.3 MeV line. As this higher excited state as well as the 10.7 MeV line's intensity is one order of magnitude smaller than either the ground state and 6.3 MeV excitation, these states are hard to distinguish with the limited resolution of the setup. The tail towards higher excitation energies is due to s-hole states creating a continuous distribution. Considering the drawback of lacking a residual nucleus identification as possible in inverse kinematics, the setup is capable of extracting the desired excitation energy data with admirable precision. This leads to the logical follow up to extract more physical output by calculating the QFS cross section for the $^{16}\text{O}(p,2p)^{15}\text{N}$ reaction in the following section.

5.3.3 $^{16}\text{O}(p,2p)^{15}\text{N}$ cross section

An elegant way to show the performance of the setup is the extraction of physical quantities, such as the cross section of the reaction measured. Usually this involves measuring incoming beam currents and emission angles (for differential cross section $\frac{d\sigma}{d\Omega}$) with high precision and additionally also having a very large geometric acceptance. As seen in chapter 3.2.4, the angular coverage in this experiment was quite small (7.08% for each petal). But in case of using a H_2O target we measure two reactions in parallel. Elastic proton-proton scattering is well understood in theory and many data sets are available from measurements. This allows us to perform just a relative measurement where all parameters like beam intensity, geometric acceptance or even dead time of the data acquisition cancel. What remains are small differences in proton detection efficiencies at slightly different energies. Figure 5.26 shows (p,p) elastic and total scattering cross sections from literature[58]. For proton energies below 400 MeV the inelastic contribution can be neglected. Above 400 MeV also other reaction mechanisms influence the cross section. Theory calculations nicely describe the measurements of the total p-p cross section[59]. In general describes the cross section σ can be described by

$$\sigma = r \cdot \frac{1}{D \cdot N_{beam}} \quad D = \frac{N_{target}}{A} \quad (5.10)$$

with r the number of desired reactions, N_{beam} total number of incoming beam particles and D the thickness of the target in units of number of target particle N_{target} per area A. As described before, in the present experiment a measurement of N_{beam} was not available, but we can normalize the two reaction channels with respect to each other. As we measure r_{pp} and know σ_{pp} the value calculated here is known and is even valid in differential form. Furthermore, as the proton-proton scattering events were from the same data set as the (p,2p) events, D and N_{beam} can be substituted by known quantities. So the (p,2p) cross section was calculated as described in equation 5.11.

$$\Delta\sigma_{p,2p} = \frac{r_{p,2p}}{r_{pp}} \cdot \Delta\sigma_{pp} \quad (5.11)$$

Using the known elastic cross section σ_{pp} and the number of detected pp events r_{pp} , the (p,2p) cross section $\sigma_{p,2p}$ was determined by a direct comparison of the simulation of the full detector setup and the experimental data using the (p,2p) and (p,p) reactions respectively. To deduce a total cross section the angular range has to be extrapolated to the full phase space. The first step is obtaining differential cross section data for $\frac{d\sigma_{pp}}{d\Omega}$ from [60]. This data set is visualized in figure 5.27. The red data set shows the cross section

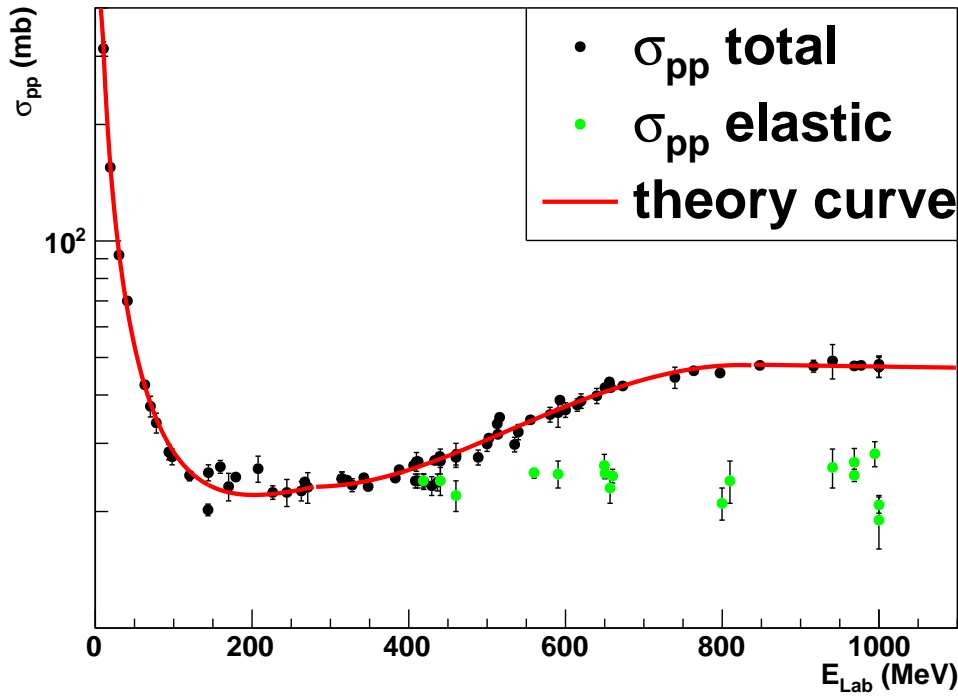


Figure 5.26: Figure illustrating experimental cross section data measured by various groups in comparison with theoretical calculations (curve [59]). The black data points represent the total and the green data points the elastic p-p cross section (data source [58]). Here is clearly observable, that for proton energies below 400 MeV both are the same. Above 400 MeV also other reaction mechanisms become relevant and the elastic cross section diverges from the total cross section.

in the center-of-mass system (CMS). For the experiment's analysis the data needs to be converted into the laboratory frame of reference using the equations 5.12 and 5.13:

$$\theta_{lab} = \arctan \left(\frac{\sin \theta_{cm}}{\gamma \cdot \left(\cos \theta_{cm} + \frac{\beta}{\beta_{cm}} \right)} \right) \quad (5.12)$$

$$\frac{d\Omega}{d\Omega_{cm}} = \gamma \cdot \frac{1 + \frac{\beta}{\beta_{cm}} \cdot \cos \theta_{cm}}{\sqrt{\sin^2 \theta_{cm} + \gamma^2 \left(\cos \theta_{cm} + \frac{\beta}{\beta_{cm}} \right)^2}} \quad (5.13)$$

The resulting data set is drawn as black dots in figure 5.27. To control the resulting total cross section after the conversion, the differential cross section in the laboratory frame was integrated using equation 5.14.

$$\sigma = \int d\varphi \int \sin \theta d\theta \frac{d\sigma}{d\Omega} \quad (5.14)$$

Integrating over the whole range and comparing to results calculated in [59] is done as cross check. This results in the total cross section for elastic p-p scattering at 200 MeV $\sigma_{pp} = 22.074$ mb (in comparison 22.068 mb from [59]). This agrees with various experimental data summarized in figure 5.26 as well. The integration over the petal's acceptance results in $\Delta\sigma_{pp}^{petal} = 0.1763$ mb. This already contains the setup's azimuth acceptance of 16.6%. Using these results on the experimental data of the water target and insert everything into

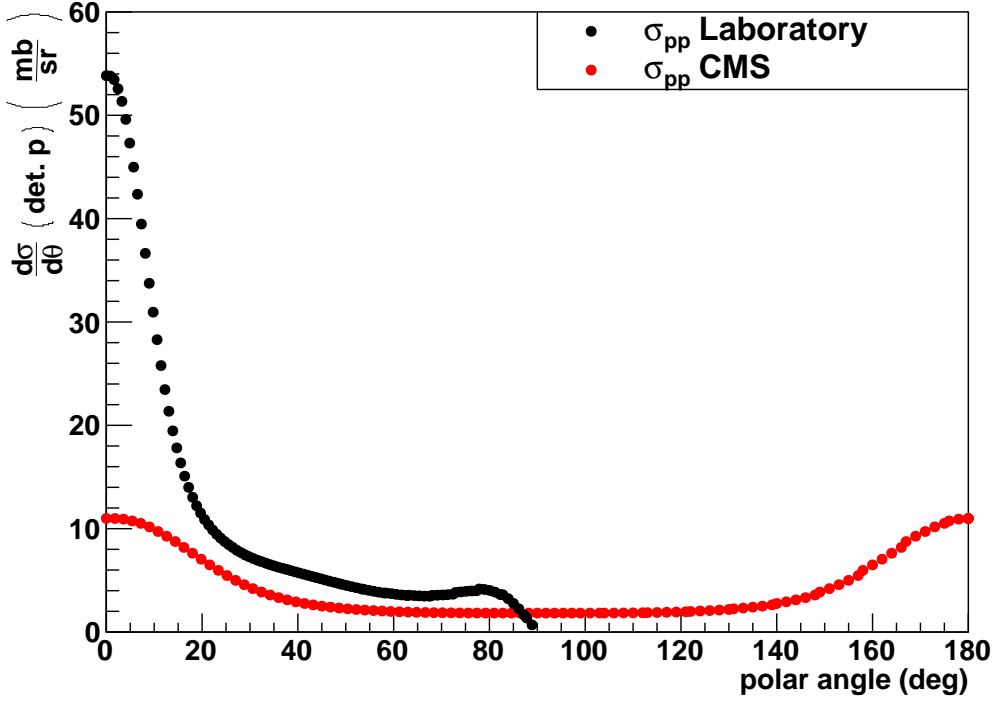


Figure 5.27: Figure shows the theoretical calculations of the differential (p,p) elastic scattering cross section at 200 MeV beam energy[60] to detect one of the protons. The red data set shows the cross section in the center-of-mass system. Using equation 5.13, the black data showing the cross section in the laboratory frame of reference are calculated from the given CMS data set.

the following formula, the cross section can be extracted:

$$\Delta\sigma_{p,2p}^{petal} = \frac{2 \cdot r_{p,2p}}{r_{pp}} \cdot \Delta\sigma_{pp}^{petal} = (0.0653 \pm 0.0003) \text{ mb} \quad (5.15)$$

Note that this already compensates for twice as many hydrogen atoms as oxygen ones in the water target. As the differential cross section of the elastic p-p scattering at 200 MeV is known[60], the simulation was used as a cross check to see if the event distribution for elastic scattering in simulation and experiment agree. Differences were considered as systematic inaccuracies of the cross section. For this the normalized event ration is plotted against the polar angle for experiment and simulation both (cf. figure 5.28). From the plot is a general agreement in distribution observable with a average difference of 4.4%, which dominated the systematic uncertainties. Note, the first data point exhibits a large variation due to border effects of the petal's acceptance caused by the strong correlation of the proton's polar emission angle in elastic scattering. As this effect is not relevant for the (p,2p) event data, we could exclude this data point from the calculation of systematic uncertainties. Now the missing step is extrapolating the cross section measured in the angular acceptance to the full cross section. For the extrapolation the in chapter 4 described simulation with the angular distribution of the Panin event generator was used. After application of the vertex and PID cut, from the 10^6 created (p,2p)-events only 28800 events were identified as (p,2p)-events in the setup, resulting in a scaling factor $s_{p,2p} = 0.229\%$. Applying this correction as described in equation 5.16 to account for the missing angular coverage and overall detection efficiency, table 5.2 summarizes the $^{16}\text{O}(p,2p)^{15}\text{N}$ cross

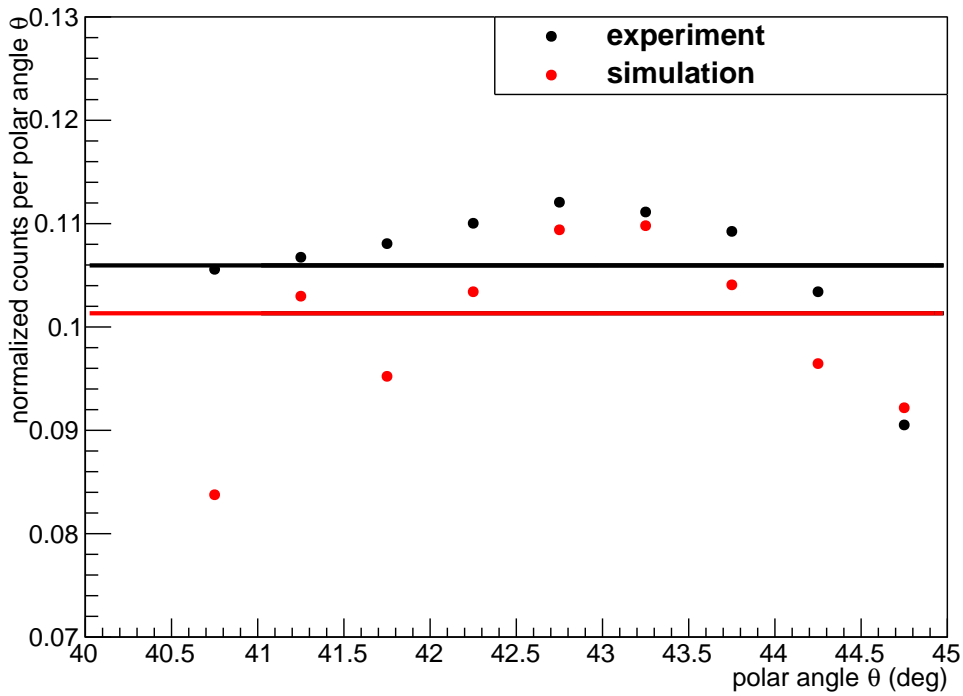


Figure 5.28: Figure shows the normalized event distribution per polar angle measured by the DSSSDs. The red dots represent the experiment data taken using the water target, while the black dots show data from a simulation using the Bertulani cross section. The shape of the distribution's agree with each other, except for the last data point, which is dominated by border effects of the petal and was neglected. The average difference between simulation and experiment is represented by the horizontal lines and is 4.4%.

section extracted from the experimental data.

$$\sigma_{p,2p}^{total} = \frac{\Delta\sigma_{p,2p}^{petal}}{S_{p,2p}} \quad (5.16)$$

A comparison of cross section measurements of the $^{16}\text{O}(p,2p)^{15}\text{N}$ reaction in inverse

State	cross section (mb)	stat. error (mb)	sys. error (mb)
ground state	7.88	± 0.44	± 0.35
excited state (6.3 MeV)	20.67	± 0.87	± 0.91
total	28.56	± 1.31	± 1.26

Table 5.2: Cross sections for $^{16}\text{O}(p,2p)^{15}\text{N}$ for the total reaction and the ground and 6.3 MeV excited state population seperately

kinematics at 290 MeV/u (S. Reichert [25]) and at 451 MeV/u (L. Atar et al. [45]) are collected in table 5.3. The total cross sections agree with each other within the errors, which concludes a successful experiment with competitive physics output to underline the proper operational conditions of the tested detectors.

State	E_{beam} (MeV/u)	cross section (mb)	error (mb)
ground state	290 [25]	9.8	± 0.8
excited state (6.3 MeV)	290 [25]	18.7	± 0.11
total	451 [45]	26.84	± 2.6

Table 5.3: Measurements of $^{16}\text{O}(p,2p)^{15}\text{N}$ cross section by other groups as comparison to the calculated values [25][45].

Chapter 6

Summary and Outlook

6.1 Resume

In the region of exotic nuclei with their unknown and complex shell structure the currently available experimental techniques reach their limit in penetrating deeper into undiscovered territory. With the (p,2p) technique in inverse kinematics a conceptually new approach is available to open up new experimental opportunities with the R³B setup. The presented thesis lays the groundwork of commissioning the central part of R³B. the CALIFA calorimeter using the (p,2p) technique in a realistic experimental environment in normal kinematics. For this purpose, a unique liquid water fiber target was developed and constructed to create a low background highly localized and oxygen-rich target with build in calibration capabilities in terms of proton elastic scattering. A simplified two arm spectrometer setup with one demonstrator petal and one layer of tracking detector's on each arm to measure particle and γ -ray energy with high precision and characterize the setup's particle identification capabilities was used in order to minimize any superfluous interference from additional components. A comparison of the measured petal parameters with the specifications set for the CALIFA calorimeter in [29] is shown in table 6.1. The

	CALIFA	Petal 0	Petal 1	Petal 2
γ -ray $\frac{\Delta E}{E}$ 1 MeV (single)	5-6%	6.06%	5.95%	4.98%
γ -ray $\frac{\Delta E}{E}$ 1 MeV (sum)	5-6%	7.15%	6.93%	5.96%
γ -ray $\frac{\Delta E}{E}$ 6 MeV (sum)	< 10%	NA	NA	1.95%
proton $\frac{\Delta E}{E}$ 100 MeV (sum)	< 1.4%	1.2%	1.2%	NA
proton γ -ray separation	down to 1 MeV	down to 1.2 MeV	down to 1.2 MeV	NA

Table 6.1: Comparison between the requirements of the CALIFA calorimeter and the parameters determined for the demonstrator petals in the Krakow experiment. Note, the single crystal values for the petals are mean values. Resolutions are given in FWHM.

single crystal (petal average) and sum γ -ray resolution for all three petals are in good agreement with the requirements for the CALIFA calorimeter. The proton energy resolution of the overall petal sum also complied with the requirements. A good separation of proton and γ -rays into the CsI(Tl) PID was achieved for the petals as well. The proton separation energy was measured by missing energy with a value of $E_{s,meas} = (12.22 \pm 0.02)$ MeV, agreeing perfectly with the literature. Three excitation lines could be reconstructed using missing mass spectroscopy and direct energy measurement with a resolution of $\sigma_{GS} = (1.8 \pm 0.5)$ MeV, $\sigma_{6.3} = (1.6 \pm 0.4)$ MeV and $\sigma_{9.9} = (2.0 \pm 0.5)$ MeV. The 6.3 MeV γ -rays were detected with $\epsilon_{\gamma} = (4.7 \pm 0.19)\%$. Also the measured ((p,2p)) cross sections agreed with several previous experiments, which is an important feature in sight of extracting cross sections of reactions with exotic beams using CALIFA. As the measurement was already possible with the limited setup presented here, much more precise experiments will be possible in the future. To even improve the Krakow setup's performance some minor improvements are proposed in the following section.

6.2 Improvements of the experiment setup

Already in the analysis, the DSSSD and petals in both arms were found to be slightly miss aligned. This is illustrated in figure 6.1. Optimizing the petal position in regards

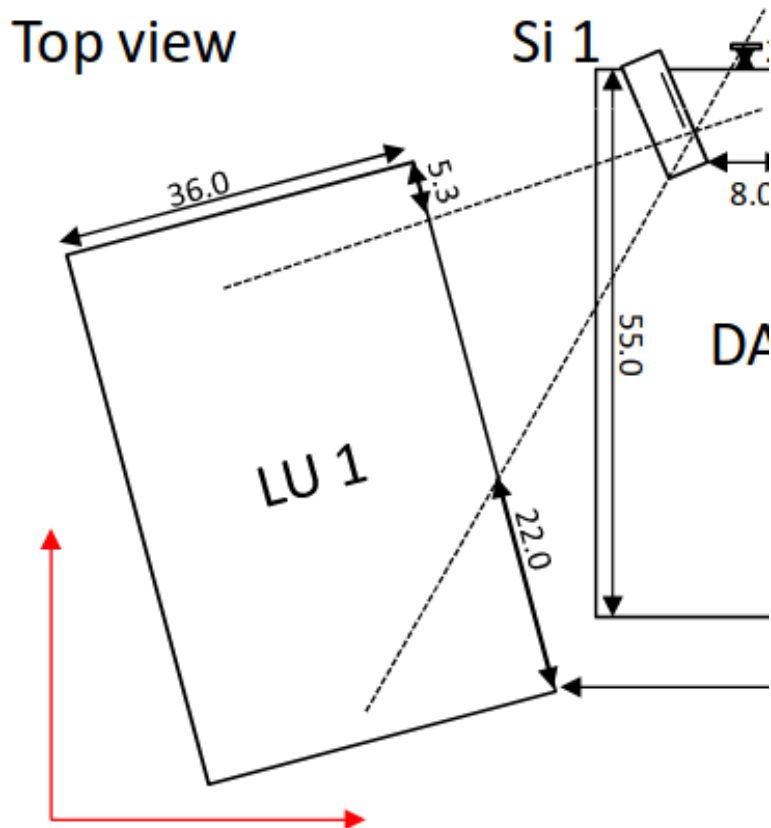


Figure 6.1: The figure shows the alignment of one demonstrator petal with the corresponding DSSSD. By the dotted line, the focal point of the petal is projected onto the DSSSD which is not centered properly.

of polar angular coverage can be done to increase the (p,2p) event rate impinging on the demonstrator detectors. Figure 6.2 shows how the position may be improved. A correlation between the minimum polar angle (cf. 6.2 b) and the number of (p,2p) events detected by the demonstrator is shown in figure 6.2 a. Assuming the same distance to the target as in the Krakow experiment results in the red distribution. While the largest event rate is observed around $\theta_{min,peak} \approx 32^\circ$, the angle used in the Krakow experiment is indicated in green ($\theta_{min,krakow} \approx 48^\circ$). So choosing the minimum polar angle of the demonstrator in the area indicated in blue would increase the event rate by a factor of three. Aim for future experiments is also the usage of so called "double" petals. These represent two petals next to each other in one housing. The usage of double petals increases the azimuth angular coverage, as this was very limited in the presented experiment.

6.3 Light crosstalk in CALIFA

An effect already observed in other experiments, is crosstalk of scintillation light from large energy deposition in CsI(Tl) by light charged particles[43]. The light intensity is so large, that the transmission through the VM2000 reflective foil is so large, that it is measureable in crystals sharing flat surfaces with each other.

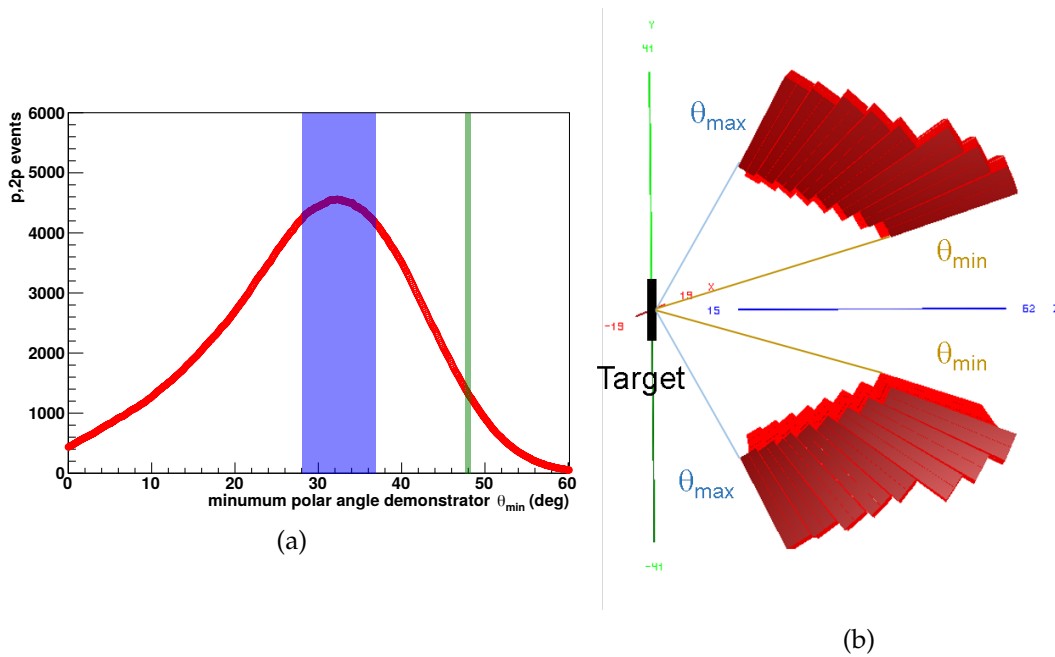


Figure 6.2: Figure a shows the correlation between the minimum polar angle of the demonstrator θ_{min} (cf. figure b) and the number of (p,2p) events detected by the demonstrator. In green the angle used in the Krakow experiment is indicated (48°), while the optimum angle is indicated by the blue area. This would increase the event rate by approximately a factor of three.

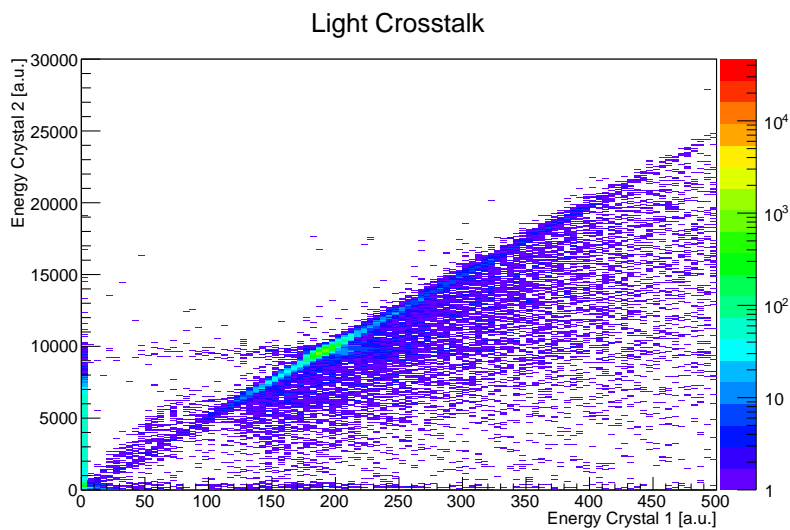


Figure 6.3: Illustration of light crosstalk between two crystals. The crystals chosen for this plot were flat neighbors sharing a 4 cm x 15 cm area. The scintillation light produced in Crystal 2 is strong enough to permeate the reflective foil and lead to a small signal in Crystal 1, as the correlation between the picture above shows.

Figure 6.3 represents the crosstalk between two "flat neighbor" crystals sharing a 4 cm x 15 cm area with each other. On both axis should therefore be events, that deposit energy in only one of the crystals, but almost no events are located on one of the axis[43]. Instead the events are correlated and have a linear relation to the energy deposited in Crystal 1 meaning that light leaks through to Crystal 1. A similar effect can be observed for the data taken with a demonstrator petal at the Krakow experiment for neighboring and next neighboring crystals (cf. figure 6.4).

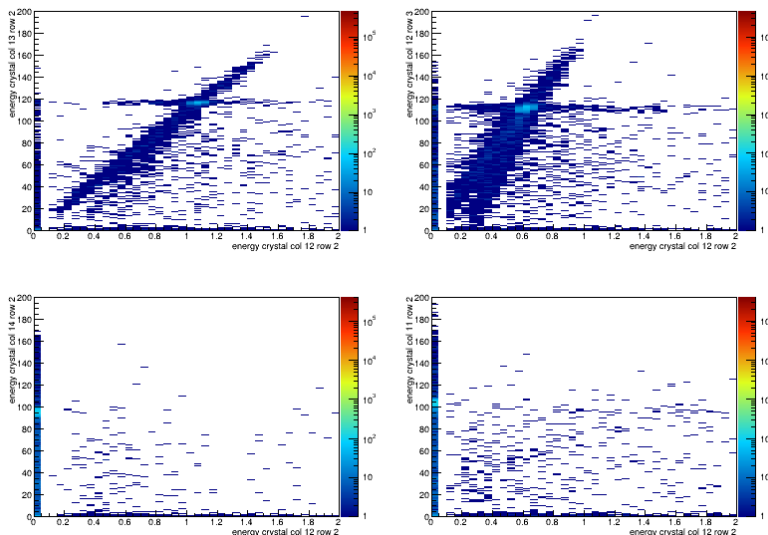


Figure 6.4: Illustration of light crosstalk between two crystals in a demonstrator petal. The upper left plot shows the energy deposition between two neighboring crystals sharing the broad side. A correlation between the energy deposition in both crystals is observed, about 0.9% at the peak. A similar effect is observed in the upper right figure, sharing the small side. The crosstalk here is smaller, only 0.5%. Compared to that, the plot on the lower left shows the correlation between two crystals separated by one crystal. No correlation is observable, as the light crosstalk is shielded by one crystal. In the lower right histogram the energy deposited in two neighboring crystals separated by the 250 μm carbon fiber wrapping of the alveoli. The expected crosstalk is not observed as the carbon fiber is light tight enough to prevent a bleed through of the scintillation light.

The upper left plot shows the energy deposition between two neighboring crystals sharing the broad side. A correlation between the energy deposition in both crystals is observed, about 0.9% at the peak. As the area shared between the next neighbor crystals was smaller than in the case shown in figure 6.3, the reduction in cross talk is understood. A similar effect is observed in the upper right figure, sharing the small side. The crosstalk here is smaller, only 0.5%. Compared to that, the plot on the lower left shows the correlation between two crystals separated by one crystal. No correlation is observable, as the light crosstalk is shielded by one crystal. In the lower right histogram the energy deposited in two neighboring crystals separated by the 250 μm carbon fiber wrapping of the alveoli. The expected crosstalk is not observed as the carbon fiber is light tight enough to prevent a bleed through of the scintillation light. Knowing this is necessary to exclude particle events and their crosstalk by the γ -ray reconstruction in CALIFA. From the observed results, only the alveolus containing the particle hit needs to be excluded. Table 6.2 summarized the observed light crosstalk in both experiments.

TRIUMF	petal broad neighbor	petal small neighbor
$\approx 1.8\%$	$\approx 0.9\%$	$\approx 0.5\%$

Table 6.2: Summary of light crosstalk observed at TRIUMF[43] and Krakow.

6.4 Outlook

The analysis and testing of the demonstrator petals of CALIFA are mainly a test run for the upcoming FAIR-Phase 0 experiment at the GSI using the upgraded accelerators to

commission the new R³B detectors and the GLAD magnet scheduled in February 2019. Figure 6.5 shows the setup that is going to be used for the Phase 0 experiment.

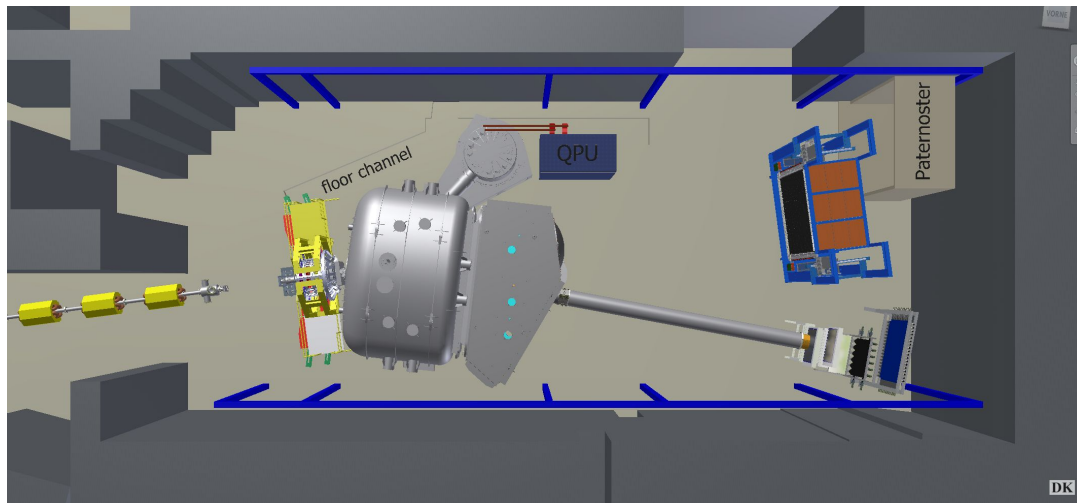


Figure 6.5: Setup of the R³B Phase 0 experiment (picture taken from [61]). The beam line from the Super-FRS enters the picture from the left. Right before the GLAD magnet around the target, CALIFA and the L³T silicon tracker are positioned for detection of target-like fragments and γ -rays. For neutron detection NeuLAND is positioned downstream of the magnet. The projectile-like are detected using the TOF detectors after the GLAD magnet.

The beam line from the Super-FRS enters the picture from the left. Right before the GLAD magnet around the target, CALIFA and the L³T (Lamp shape Low mass Light particle Tracker) silicon tracker are positioned for detection of target-like fragments and γ -rays. For neutron detection NeuLAND is positioned downstream of the magnet. The projectile-like particles are detected using TOF detectors after the GLAD magnet. During Phase 0 most detectors are replaced by their demonstrators. The CALIFA demonstrator will consist of four single petals (64 detector units) and two double petals (128 detector units) partly positioned in the nominal barrel position ($42^\circ < \Theta < 90^\circ$) and partly tilted forward in an encap-like position ($28^\circ < \Theta < 70^\circ$) coming up to a total azimuthal angle coverage of 50%. A schematic drawing is shown in figure 6.6. Aim of the experiment is commissioning of the demonstrator detectors in order to guarantee excellent performance of the final setup at FAIR. In the experiment a ^{12}C beam at different energies is used to irradiate a plastic target with $I = 10^7$ 1/s. Some preliminary simulation results of the expected detector response analyzing the $^{12}\text{C}(p,2p)^{11}\text{B}$ reaction at 200 AMeV are shown in the following. In the simulation an excitation of 4.444 MeV of the residual ^{11}B nucleus was assumed with a branching ratio of 50%. This simplification is used to reduce the complex level structure, while retaining a decent picture of the most prominent excitation line populated by the (p,2p) reaction. Aim is inspecting the Doppler correction and excitation energy reconstruction capabilities of the demonstrator angles compared to a perfect angular resolution in order to access the effect of the angular measurement has on the each desired quantity. Additionally for comparability with the Krakow experiment, the simulation was also done in normal kinematics and will be presented.

Figure 6.7 shows the emitted (a) and detected (b) protons' energy distribution smeared by the beam nucleus' internal momentum distribution so in both figures only one broad line is visible. In total 5.8% of the emitted protons are detected in the demonstrator setup. Opposed to normal kinematics no additional information is accessible from the energy distribution of the protons. Studying the polar angular distribution (cf. figure 6.8 a) reveals a sharp edged correlation of the proton's emission angle with a tail towards smaller angles. The detected angles by the demonstrator are shown in figure 6.8 b) and reproduce the

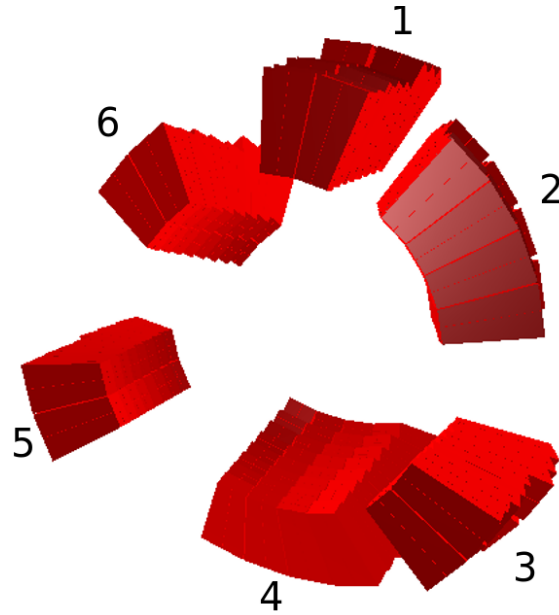


Figure 6.6: Schematic setup of the CALIFA demonstrator with 4 single petals and 2 double petals. Detectors (1,3,5) are positioned in $42^\circ < \Theta < 90^\circ$, while detectors (2,4,6) in $28^\circ < \Theta < 70^\circ$ with a total azimuthal angle coverage is roughly 50%.

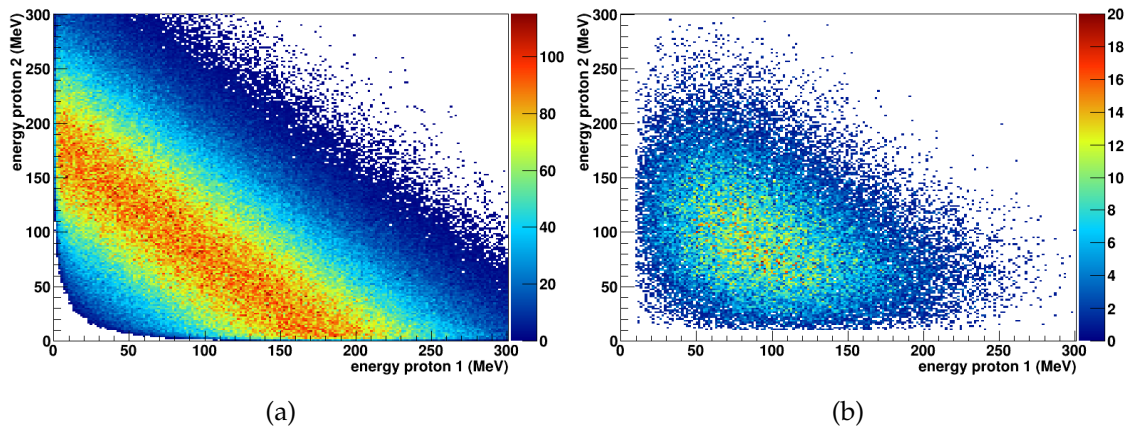


Figure 6.7: Figure a) shows the emitted protons energy distribution from a $^{12}\text{C}(p,2p)^{11}\text{B}$ simulation in inverse kinematics at $E_{beam} = 200$ AMeV. It is smeared out by the ^{12}C nucleus' internal momentum distribution. Due to this, information accessible in normal kinematics like the proton separation energy and a separation of the ground and excited states is lost. Figure b) shows the energy of protons detected by the experiment setup. It shows a part of the distribution in figure a) as only 5.8% of the events are detected in the demonstrator, but the same distribution shape.

correlation observed in figure a) between 20° and 60° . This well defined opening angle ($\theta_{op} = 80.1^\circ$) increases the need for accurate proton angle measurement. Additionally the azimuth angular distribution is of interest. Figure 6.9 a shows the distribution of protons around the expected 180° opening angle. In figure 6.9 b the detected azimuth emission angle reproduces the observed correlation but due to lacking angular coverage the plot just covers a small area. Though the angular coverage and resolution of the demonstrator setup are limited, Doppler correction is done successfully using the average crystal angles as figure 6.10 shows. The black histogram shows the γ -ray spectrum detected by the demonstrator detectors Doppler shifted in the laboratory frame, where instead of a sharp

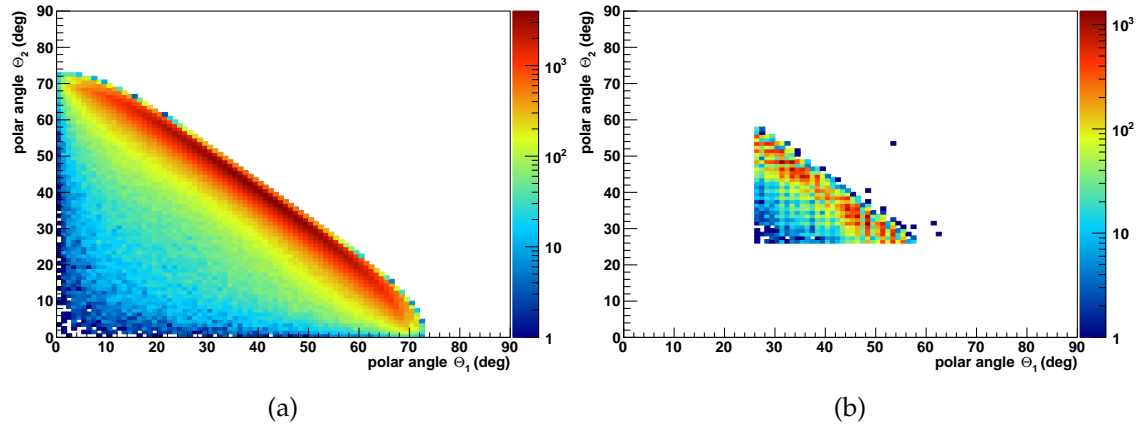


Figure 6.8: Figure a) shows the (p,2p) protons' polar emission angles taken from the primary track vectors (perfect angular measurement). The sharp correlation between the emission angles leads to a well defined polar opening angle $\theta_{op} = 80.1^\circ$ and indicates the importance of proper angular measurement. In comparison figure b) shows the polar emission angles measured by the demonstrator within its acceptance. The correlation observed in figure a) is reproduced with limited resolution.

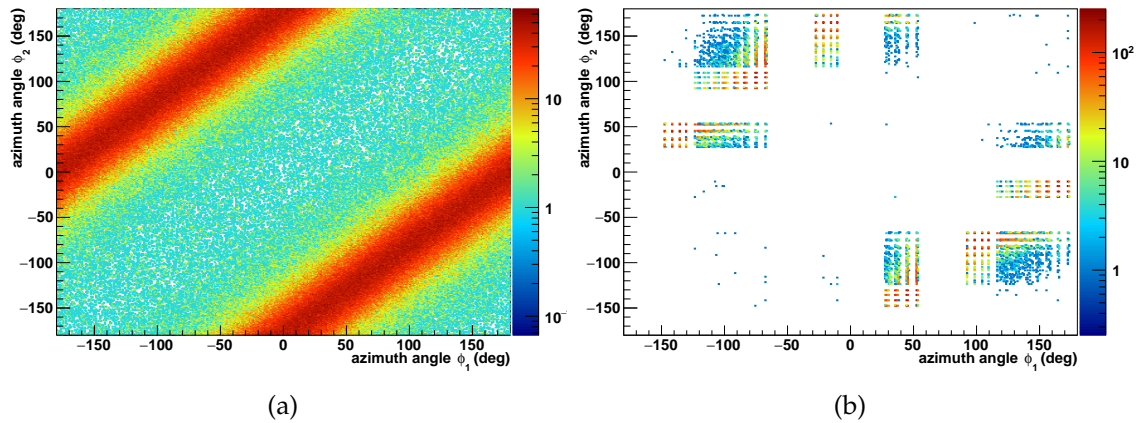


Figure 6.9: Figure a) shows the (p,2p) protons' azimuth emission angles taken from the primary track vectors (perfect angular measurement). The expected 180° opening angle can be observed by the correlation between the emission angles. In comparison figure b) shows the azimuth emission angles measured by the demonstrator within its acceptance. Due to a not continuous azimuthal coverage only parts of the correlation lines observed in figure a) is reconstructed.

photo peak only a broad distribution is observable. Correcting for this shift by emission from an ion moving at relativistic velocities is done by measuring the γ -ray's emission angle, i.e. the center of gravity of the crystal with the largest energy deposit, and using equation 6.1.

$$E_\gamma = E'_\gamma \cdot (1 - \beta \cdot \cos \theta_\gamma) \cdot \gamma \quad (6.1)$$

After the correction the full energy peak is observed at 4.446 MeV at a resolution of $\frac{\Delta E}{E} = 3.3\%$ (cf. figure 6.10). In blue the true emission angles of the γ -radiation is used for reconstruction of the energy. The resulting full energy peak is slightly more narrow than the red one, which in numbers means a resolution of $\frac{\Delta E}{E} = 2.5\%$. So this shows only a small increase in resolution by using perfect angular measurement, the granularity of the demonstrator is sufficient for the reconstruction. On the other hand the angular measurement is also of import for the reconstruction of the excitation energy as described

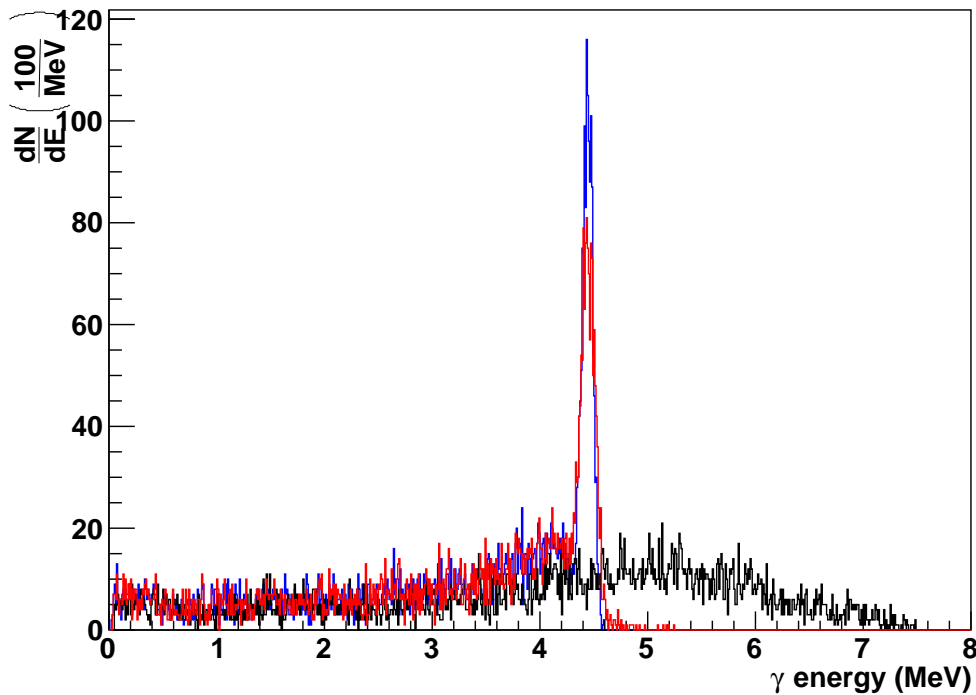


Figure 6.10: Figure shows γ -ray spectra using the energy measured by the demonstrator and different angular measurements for Doppler reconstruction. In the black histogram the raw data is shown. Only a broad peak is observed and no full energy peak can be discerned. Using the primary vector angles results in the blue histogram. A peak at 4.446 MeV is observed associated with the full energy peak of the excitation γ -ray with a resolution of $\frac{\Delta E}{E} = 2.5\%$. To create the red histogram the emission angles measured using the demonstrator were used. With the energy resolution only a bit worse with $\frac{\Delta E}{E} = 3.3\%$, the angular measurement's precision is sufficient for a proper Doppler reconstruction.

in chapter 1.2.3. The reconstruction of the excitation energy is shown in figure 6.11. In the red histogram the excitation energy reconstructed by a missing mass calculation using the protons emission angles supplied by the simulation and the detected proton energies. Two peaks are observed associated with the ground state ($\sigma_{GS} = 136$ keV) and 4.444 MeV ($\sigma_{4.4} = 152$ keV) excited state. The peaks are well separated with some background from miss identified (p,2p) protons. Using the L³T silicon tracker for angular measurement ($\sigma_{\theta} = 1.3$ mrad, $\sigma_{\theta} = 0.2$ mrad) results in the blue histogram. Similar to the red histogram, both the ground state and the excited state peaks are observed but with increased width ($\sigma_{GS} = 472$ keV, $\sigma_{4.4} = 491$ keV). In contrast to this, the black histogram is the result of using the measured angles by the demonstrator for the reconstruction of the excitation energy. As the accuracy of the angular measurement is insufficient it results in a broad peak. This histogram impressively shows the need for a particle tracker in experiments in inverse kinematics, which was less important in the normal kinematics experiment (see chapter 5).

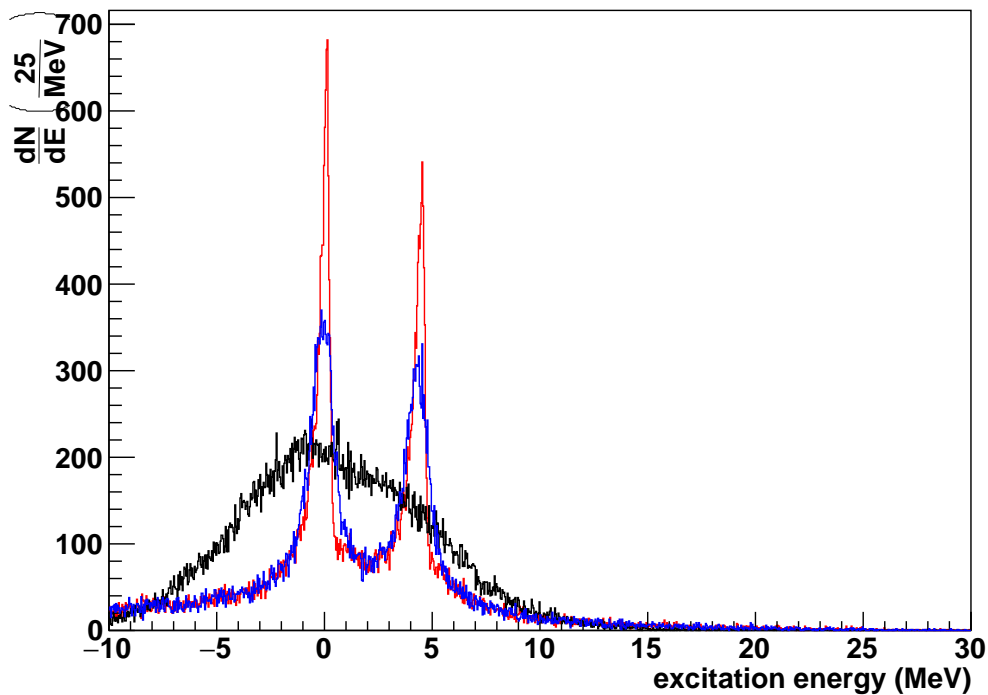


Figure 6.11: Figure shows the excitation energy reconstructed in inverse kinematics using different angular measurements and the proton energy measured by the demonstrator. In red the excitation energy is calculated using the emission angles of the primary vectors representing the best achievable resolution ($\sigma_{GS} = 136$ keV, $\sigma_{4.4} = 152$ keV). Two peaks associated with the ground state and the excited state at 4.444 MeV are observed and well separated. Using the emission angles measured by the L³T results in the blue histogram. Here also both peaks are observed with a decreased resolution ($\sigma_{GS} = 472$ keV, $\sigma_{4.4} = 491$ keV) compared to the red histogram. Finally the black histogram represents the reconstructed excitation energy using the demonstrator angles. Due to the insufficient angular resolution the peaks are no longer separable and result in one broad distribution.

Appendix A

Appendix

A.1 Interstrip method

Additional to using the DSSSD strips individually, the so called "inter strip" technique can be used to increase the angular resolution by using the ratio of the deposited energy by a particle in adjacent strips. Figure A.1 shows a schematic drawing to illustrate the methodology of the inter strip technique. The arrows represent particles passing through the silicon strips. The red arrow passes only through strip a) and so angular measurement is limited to the position information gained by this strip. The green and purple arrows both pass through two strips each with different ratios of energy deposition. While in case of the green arrow more energy is deposited in strip b) than in strip c), for the purple arrow the situation is reversed. Using the energy deposition in the strips a weighting factor r_n can be defined (cf. equation A.1).

$$r_n = \frac{E_n - E_{n-1}}{E_n + E_{n-1}} \quad (\text{A.1})$$

with the energy deposition in the adjacent strips E_n and E_{n-1} and the strip number n . This weighting factor r_n enables a finer sampling of the measured emission angle than using the sampling given by the 1.8 mm wide strips of the DSSSD detectors used. Figure A.2 shows the correlation of energy deposited in adjacent strips in arbitrary units. In figure A.2a shows a prominent correlation between the energy deposited in strips i and j . The cut out corner around the origin of the histogram is produced by the DSSSD strips individual threshold set to 100 a.u., which in this case cuts into the correlation, as the overall signal is small compared to the threshold selected. Figure A.2b shows the energy deposition

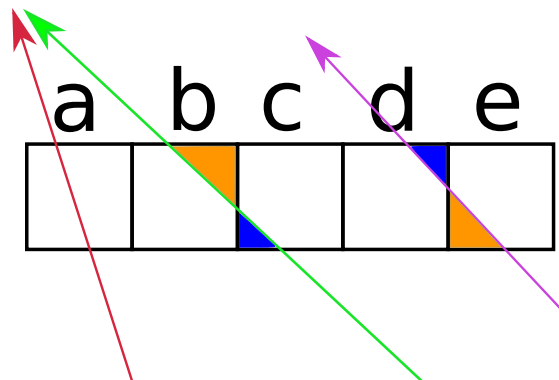


Figure A.1: Figure shows a schematic drawing of five silicon detector strips labeled a) to e) to illustrate the inter strip technique. The arrows represent particles passing through the silicon strips. The red arrow passes only through strip a) and so angular measurement is limited to the position information gained by this strip. The green and purple arrows both pass through two strips each with different ratios of energy deposition. While in case of the green arrow more energy is deposited in strip b) than in strip c), for the purple arrow the situation is reversed. This defines a weighting factor for the angular measurement introduced in equation A.1.

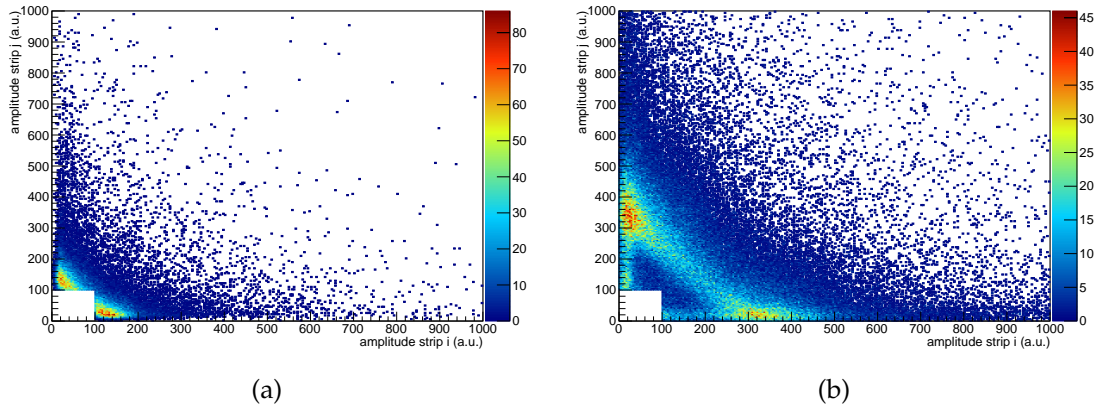


Figure A.2: Figure shows the correlation between energy deposited in adjacent strips i and j in arbitrary units. In figure a) shows a prominent correlation between the energy deposited in strips i and j . The cut out corner around the origin of the histogram is produced by the DSSSD strips individual threshold set to 100 a.u., which in this case cuts into the correlation, as the overall signal is small compared to the threshold selected. Figure b) shows the energy deposition in adjacent strips for DSSSD1. As in figure a) a correlation is clearly observed, but opposed to before the signal is at least by a factor of two larger, making the cut off effect of the trigger threshold negligible.

in adjacent strips for DSSSD1. As in figure A.2a a correlation is clearly observed, but opposed to before the signal is at least by a factor of two larger, making the cut off effect of the trigger threshold negligible. Compared to the full statistics of the DSSSDs, in DSSSD0 only 2.3% are usable as inter strip events, due to the trigger cutoff, while in DSSSD1 11.8% of the events can be used in the inter strip technique. If we require inter strip events in both DSSSDs, only 0.3% of the total events survive the cuts. Due to this rather low value, the use of the inter strip technique is disregarded in the following analysis, but nevertheless needs to be kept in mind for future experiments, as some potential was lost here.

A.2 Petal Mapping

As the calibration of the DSSSDs is concluded, only one calibration step remains. It is known, that the three petal detectors contain 64 CsI(Tl) detectors each, distributed over 16 columns in 4 rows. These detectors were constructed in different locations (two at the Lund University, one at the TU Darmstadt), so the mapping of the detector positions within the housing may vary. Without a proper mapping, an event reconstruction in the petals is impossible, so one needs to take great care to have the crystals properly mapped. Figure A.3 shows the event distribution for raw polypropylene target data of one of the Lund Petals before and after the mapping process. In figure A.3 a the distribution is chaotic with the highest intensity in the upper end of the petal. As column 15 was closest to the beam line, one would expect the highest intensity to be found there. Also the whole distribution is checkered so the channel mapping seems to be wrong indeed. Figure A.3 b shows the event distribution after applying the mapping. The distribution is now sorted from high intensity to low from column 15 to 0. Also the rows now have roughly the same intensity per column. The mapping is the same for the second Lund petal. As the third petal was constructed in a different location, the mapping needs to be checked for it independently. Figure A.4 shows the event distribution for petal 2. The unmapped distribution is shown in figure A.4 a. The whole plot exhibits an odd even

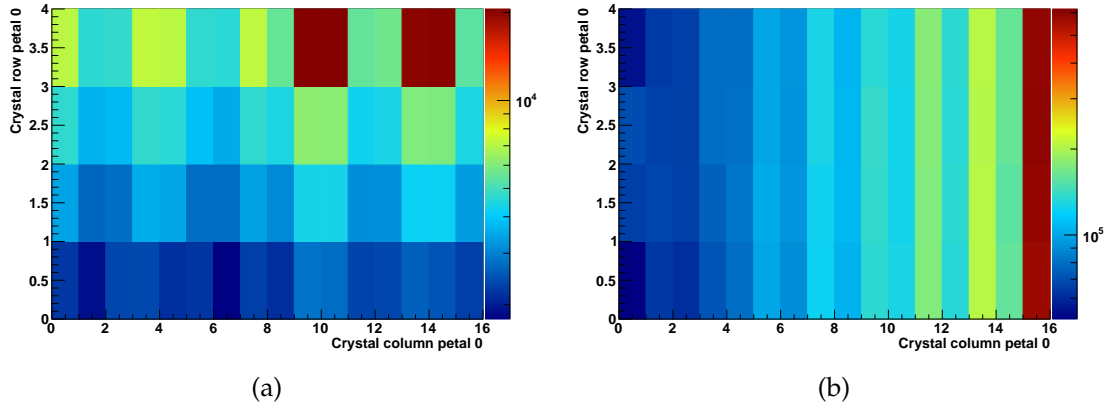


Figure A.3: In figure a) the distribution is chaotic with the highest intensity in row three, so the upper end of the petal. As column 15 was closest to the beam line, one would expect the highest intensity to be found there. Also the whole distribution is checkerboarded so the channel mapping seems to be wrong indeed. Figure b) shows the event distribution after applying the mapping. The distribution is now sorted from high intensity to low from column 15 to 0. Also the rows now have roughly the same intensity per column.

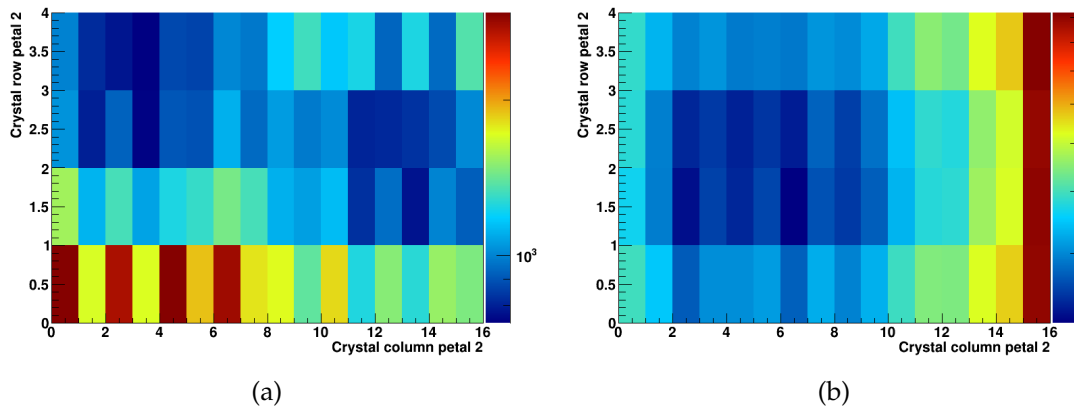


Figure A.4: Figure a) shows the unsorted events distribution. The odd even staggering and the highest intensity in the lower left corner of the plot indicate the need for remapping the crystal positions. Figure b) shows the remapped event distribution. The plot shows the expected intensity sorting as in figure A.3, but with an additional feature in the row 1 and 2 for columns 2 to 10, where the intensity is lower than in the surrounding crystals. This effect is due to the DSSSD mounting table between the petal and the target.

staggering with the highest intensity in the lower left corner. Also in petal 2 a mapping needs to be applied, but a different one from the Lund petals. This is done in figure A.4 b. On first glance the event distribution looks wrong as well, as one would expect a similar one to figure A.3 b. The highest intensity is on the expected crystal row in the most forward direction, as most elastics are emitted here. Moving closer to the target with decreasing crystal column, the middle two rows detect a lower intensity than the surrounding ones, which seems like the crystals being miss-sorted. Keeping in mind, that the petal was positioned below the target, where also a table was placed for the DSSSD mounting plate as can be seen in figure 5.8. So the reduced intensity is the petal being shaded by the table being positioned between it and the target.

A.3 Elastic cross section data

#Ep_lab = 200 MeV

#theta_cm	dsigma/dOmega_cm [mb/sr]
0.00	6.18
1.80	6.17
3.60	6.14
5.40	6.10
7.20	6.03
9.00	5.95
10.8	5.85
12.6	5.74
14.4	5.61
16.2	5.47
18.0	5.32
19.8	5.15
21.6	4.98
23.4	4.80
25.2	4.61
27.0	4.42
28.8	4.23
30.6	4.03
32.4	3.84
34.2	3.65
36.0	3.46
37.8	3.28
39.6	3.10
41.4	2.93
43.2	2.77
45.0	2.61
46.8	2.47
48.6	2.33
50.4	2.21
52.2	2.09
54.0	1.99
55.8	1.90
57.6	1.82
59.4	1.74
61.2	1.68
63.0	1.62
64.8	1.58
66.6	1.54
68.4	1.51
70.2	1.49
72.0	1.47
73.8	1.45
75.6	1.44
77.4	1.43
79.2	1.43
81.0	1.43
82.8	1.42

84.6	1.42
86.4	1.42
88.2	1.42
90.0	2.24
91.8	2.24
93.6	2.24
95.4	2.24
97.2	2.24
99.0	2.24
101.	2.24
103.	2.24
104.	2.24
106.	2.24
108.	2.24
110.	2.24
112.	2.24
113.	2.24
115.	2.24
117.	2.24
119.	2.24
121.	2.24
122.	2.24
124.	2.25
126.	2.25
128.	2.26
130.	2.27
131.	2.28
133.	2.31
135.	2.35
137.	2.40
139.	2.48
140.	2.59
142.	2.74
144.	2.94
146.	3.19
148.	3.51
149.	3.90
151.	4.37
153.	4.93
155.	5.58
157.	6.32
158.	7.13
160.	8.01
162.	8.95
164.	9.93
166.	10.9
167.	11.9
169.	12.8
171.	13.6
173.	14.4
175.	15.0

Appendix A Appendix

176.	15.4
178.	15.7
180.	15.8

0	30.2717
0.813307	30.217
1.62669	30.0528
2.44022	29.8285
3.25396	29.4467
4.06801	29.0061
4.88242	28.4586
5.69727	27.8542
6.51263	27.1453
7.32858	26.3819
8.14519	25.5653
8.96253	24.649
9.78067	23.7306
10.5997	22.7636
11.4196	21.7497
12.2406	20.7376
13.0627	19.7285
13.8859	18.6771
14.7103	17.6774
15.5361	16.6837
16.3631	15.6972
17.1917	14.7637
18.0217	13.8385
18.8532	12.9668
19.6864	12.1482
20.5213	11.3389
21.3579	10.6255
22.1964	9.92117
23.0367	9.31064
23.8789	8.70846
24.7231	8.1975
25.5694	7.73465
26.4178	7.31882
27.2683	6.90916
28.1211	6.58436
28.9761	6.26424
29.8334	6.02531
30.6931	5.78935
31.5552	5.59358
32.4198	5.43649
33.2868	5.28058
34.1564	5.12596
35.0286	5.00752
35.9034	4.8894
36.7808	4.80528
37.6609	4.72045
38.5438	4.60256
39.4294	4.51708

40.3177 4.43106
41.2089 4.34456
42.1029 6.71625
42.9997 6.57851
43.8994 6.44025
44.8019 6.30154
45.7074 6.16244
46.6157 6.02305
47.6283 5.86788
48.6446 5.71251
49.154 5.63477
50.1756 5.47924
51.2008 5.3237
52.2295 5.16823
53.2617 5.0129
53.7791 4.9353
54.8166 4.78029
55.8576 4.62555
56.902 4.47116
57.9497 4.31714
58.4749 4.24029
59.5277 4.10516
60.5837 3.95159
61.6429 3.81541
62.7053 3.67841
63.2377 3.61754
64.3046 3.50941
65.3746 3.41235
66.4474 3.3244
67.5229 3.26997
68.0618 3.32897
69.1413 3.34029
70.2235 3.39015
71.3081 3.4688
72.395 3.58701
72.9393 3.85829
74.0295 4.03882
75.1217 4.23665
76.2159 4.4346
77.3119 4.61559
77.8605 4.97805
78.9589 5.07885
80.0588 5.1026
81.16 5.02803
82.2623 4.82565
82.8139 4.89039
83.9178 4.44827
85.0226 3.86498
86.1279 3.18162
87.2339 2.36654
87.787 1.9435

88.8934 0.990524

90 -1.48731e-09

Bibliography

- [1] Wikipedia, "Atomism." <https://en.wikipedia.org/wiki/Atomism>, 2016.
- [2] T. Mayer-Kuckuk, *Kernphysik, Eine Einführung, 4. Auflage*. Stuttgart: Teubner Studienbücher, 1984.
- [3] M. O. Winkel, "Komplexe Pulsformalgorithmen und Teilchenidentifikation zur Echtzeit-Implementierung in CALIFA." phd thesis, 2015.
- [4] M. Bendel, "Entwicklung einer neuartigen Nachweismethode für hochenergetische Teilchen für das CALIFA Kalorimeter." phd thesis, 2014.
- [5] C. Weizsäcker, "Zur theorie der kernmassen," *Zeitschrift der Physik*, vol. 96, pp. 431 – 458, 1935.
- [6] N. Bohr, "Can quantum-mechanical description of physical reality be considered complete?," *Phys. Rev.*, vol. 48, pp. 696–702, Oct 1935.
- [7] Povh, Rith, Scholz, and Zetsche, *Particles and Nuclei, 8th Edition*. Heidelberg: Springer Verlag, 2008.
- [8] . J. J. H. D. Mayer, M. G., "Elementary theory of nuclear shell structure," 1955.
- [9] T. Otsuka and D. Abe, "Mean field properties of exotic nuclei and the tensor force," *Progress in Particle and Nuclear Physics*, vol. 59, no. 1, pp. 425 – 431, 2007. International Workshop on Nuclear Physics 28th Course.
- [10] T. Otsuka, T. Suzuki, R. Fujimoto, H. Grawe, and Y. Akaishi, "Evolution of nuclear shells due to the tensor force," *Phys. Rev. Lett.*, vol. 95, p. 232502, Nov 2005.
- [11] R. Krucken, "Introduction to shell structure of exotic nuclei," *Submitted to: Contemp. Phys.*, 2010.
- [12] T. Otsuka, T. Suzuki, M. Honma, Y. Utsuno, N. Tsunoda, K. Tsukiyama, and M. Hjorth-Jensen, "Novel features of nuclear forces and shell evolution in exotic nuclei," *Phys. Rev. Lett.*, vol. 104, p. 012501, Jan 2010.
- [13] D. Rohe, C. S. Armstrong, R. Asaturyan, O. K. Baker, S. Bueltmann, C. Carasco, D. Day, R. Ent, H. C. Fenker, K. Garrow, A. Gasparian, P. Gueye, M. Hauger, A. Honegger, J. Jourdan, C. E. Keppel, G. Kubon, R. Lindgren, A. Lung, D. J. Mack, J. H. Mitchell, H. Mkrtchyan, D. Mocolj, K. Normand, T. Petitjean, O. Rondon, E. Segbefia, I. Sick, S. Stepanyan, L. Tang, F. Tiefenbacher, W. F. Vulcan, G. Warren, S. A. Wood, L. Yuan, M. Zeier, H. Zhu, and B. Zihlmann, "Correlated strength in the nuclear spectral function," *Phys. Rev. Lett.*, vol. 93, p. 182501, Oct 2004.
- [14] P. Batham, I. J. Thompson, and J. A. Tostevin, "Dynamical core deformation effects on single-nucleon knockout reactions at fragmentation beam energies," 2005.
- [15] B. A. Brown, P. G. Hansen, B. M. Sherrill, and J. A. Tostevin, "Absolute spectroscopic factors from nuclear knockout reactions," *Phys. Rev. C*, vol. 65, p. 061601, May 2002.

- [16] J. A. Tostevin and A. Gade, "Systematics of intermediate-energy single-nucleon removal cross sections," *Phys. Rev. C*, vol. 90, p. 057602, Nov 2014.
- [17] F. Käppeler, R. Gallino, S. Bisterzo, and W. Aoki, "The s process: Nuclear physics, stellar models, and observations," *Rev. Mod. Phys.*, vol. 83, pp. 157–193, Apr 2011.
- [18] FAIR, "FAIR - Baseline Technical Report, Volume 1." Website, 2006.
- [19] M. Winkler, S. Althoff, F. Amjad, K. Behr, A. Bergmann, T. Blatz, A. Brünle, E. J. Cho, W. Freisleben, H. Geissel, M. Gleim, C. Karagiannis, B. Kindler, H. Kollmus, E. Kozlova, A. Krämer, A. Kratz, J. Kurdal, H. Leibrock, H. Müller, G. Münzenberg, C. Mühle, I. Mukha, C. Nociforo, L. M. Orona, S. Pietri, A. Prochazka, S. Purushotaman, M. V. Ricciardi, C. Scheidenberger, F. Schirru, C. Schlör, P. Schnizer, H. Simon, P. Szwangruber, F. Wamers, H. Weick, C. Will, J. Winfield, and Y. Xiang, *Super-FRS design status report*, vol. 2015-1 of *GSI Report*, pp. 496–497 p. Darmstadt: GSI Helmholtzzentrum für Schwerionenforschung, 2015.
- [20] R3B, "Technical Report for the Design, Construction and Commissioning of the CALIFA Barrel: The R3B CALorimeter for In Flight detection of gamma rays and high energy charged pArticles." Website, 2011.
- [21] B. Gastineau, A. Donati, J. Ducret, D. Eppelle, P. Fazilleau, P. Graffin, B. Hervieu, D. Loiseau, J. Lottin, C. Mayri, C. Meuris, C. Pes, Y. Queinec, and Z. Sun, "Design status of the r3b-glad magnet: Large acceptance superconducting dipole with active shielding, graded coils, large forces and indirect cooling by thermosiphon," *IEEE Transactions on Applied Superconductivity*, vol. 18, pp. 407–410, June 2008.
- [22] The R³B Collaboration, "Technical Report for the Design, Construction and Commissioning of the Tracking Detectors for R³B," 2014.
- [23] C. A. Bertulani, "Theory and Applications of Coulomb Excitation," 2009.
- [24] The R³B Collaboration, "A universal setup for kinematical complete measurements of Reactions with Relativistic Radioactive Beams R³B," 2004.
- [25] S. Reichert, "Detector Development for High Precision Measurements of (p,2p) Reactions in Inverse Kinematics using the Missing Mass Spectroscopy." phd thesis, 2018.
- [26] V. Panin, J. Taylor, S. Paschalis, F. Wamers, Y. Aksyutina, H. Alvarez-Pol, T. Aumann, C. Bertulani, K. Boretzky, C. Caesar, M. Chartier, L. Chulkov, D. Cortina-Gil, J. Enders, O. Ershova, H. Geissel, R. Gernhäuser, M. Heil, H. Johansson, B. Jonson, A. Kelić-Heil, C. Langer, T. L. Bleis, R. Lemmon, T. Nilsson, M. Petri, R. Plag, R. Reifarth, D. Rossi, H. Scheit, H. Simon, H. Weick, and C. Wimmer, "Exclusive measurements of quasi-free proton scattering reactions in inverse and complete kinematics," *Physics Letters B*, vol. 753, pp. 204 – 210, 2016.
- [27] T. Aumann, C. A. Bertulani, and J. Ryckebusch, "Quasifree (p,2p) and (p,pn) reactions with unstable nuclei," *Phys. Rev. C*, vol. 88, p. 064610, Dec 2013.
- [28] W.-M. Y. et al, "Review of particle physics," *Journal of Physics G: Nuclear and Particle Physics*, vol. 33, no. 1, p. 1, 2006.
- [29] The R³B Collaboration, "Technical Report for the Design, Construction and Commissioning of the CALIFA Barrel," 2011.

- [30] The R³B Collaboration, "Technical Report for the Design, Construction and Commissioning of the CALIFA Endcap," 2015.
- [31] R3B, "Technical Report for the Design, Construction and Commissioning of the CALIFA Endcap: The R3B CALorimeter for In Flight detection of gamma rays and high energy charged pArticles." Website, 2015.
- [32] M. Bendel, R. Gernhäuser, M. Winkel, H. Alvarez-Pol, D. Cortina-Gil, B. Heiss, W. F. Henning, P. Klenze, T. L. Bleis, C. Pfeffer, and B. Pietras, "iphos, a new technique for the califa csi(tl) calorimeter," *Journal of Physics: Conference Series*, vol. 587, no. 1, p. 012049, 2015.
- [33] M. Gascon, H. Alvarez-Pol, J. Benlliure, E. Casarejos, D. Cortina-Gil, and I. Duran, "Optimization of energy resolution obtained with csi(tl) crystals for the r3b calorimeter," *Nuclear Science, IEEE Transactions on*, vol. 55, pp. 1259–1262, June 2008.
- [34] G. F. Knoll, *Radiation detection and measurement; 4th ed.* New York, NY: Wiley, 2010.
- [35] R. S. Storey, W. Jack, and A. Ward, "The fluorescent decay of csi(tl) for particles of different ionization density," *Proceedings of the Physical Society*, vol. 72, no. 1, p. 1, 1958.
- [36] A. N. Jette, T. L. Gilbert, and T. P. Das, "Theory of the Self-Trapped Hole in the Alkali Halides," *Phys. Rev.*, vol. 184, pp. 884–894, Aug 1969.
- [37] V. Babin, K. Kalder, A. Krasnikov, and S. Zazubovich, "Luminescence and defects creation under photoexcitation of CsI(Tl) crystals in Tl+-related absorption bands," *Journal of Luminescence*, vol. 96, no. 1, pp. 75 – 85, 2002.
- [38] V. Nagirnyi, A. Stolovich, S. Zazubovich, V. Zepelin, E. Mihokova, E. Nikl, G. P. Pazzi, and L. Salvini, "Peculiarities of the triplet relaxed excited-state structure and luminescence of a CsI:Tl crystal," *Journal of Physics: Condensed Matter*, vol. 7, no. 18, p. 3637, 1995.
- [39] J. Valentine, W. W. Moses, S. E. Derenzo, D. K. Wehe, and G. F. Knoll, "Temperature dependence of CsI(Tl) gamma-ray scintillation decay time constants and emission spectrum," *Proc. SPIE*, vol. 1734, pp. 32–43, 1992.
- [40] M. Winkel, "Implementierung und Erprobung einer digitalen Pulsformanalyse zur Auslese von Kalorimetern." diploma thesis, 2011.
- [41] M. Winkel, "Komplexe Pulsformalgorithmen und Teilchenidentifikation zur Echtzeit-Implementierung in CALIFA." phd thesis, 2016.
- [42] A. Georgiev and W. Gast, "Digital pulse processing in high-resolution, high-throughput, gamma-ray spectroscopy," in *Nuclear Science Symposium and Medical Imaging Conference, 1992., Conference Record of the 1992 IEEE*, pp. 534–536 vol.1, Oct 1992.
- [43] B. Heiss, "Experimental Verification of the iPhos Energy Reconstruction Method for the CALIFA Calorimeter." master thesis, 2014.
- [44] I. PAN, "Bronowice Cyclotron Center," 2018.
- [45] L. e. a. Atar, "Quasifree ($p, 2p$) reactions on oxygen isotopes: Observation of isospin independence of the reduced single-particle strength," *Phys. Rev. Lett.*, vol. 120, p. 052501, Jan 2018.

- [46] B. N. Laboratory, "National nuclear datagroup chart of nuclei." Website, 2018.
- [47] K. K. et al., "De-excitation gamma-rays from the s-hole state in n-15 associated with proton decay in o-16," 2006.
- [48] H. P. K.K., "Data sheet of Si APD S8664-1010." Website, 2005.
- [49] D. R. et al., "LYCCA Technical Design Report, FAIR-NUSTAR," June 2008.
- [50] P. Golubev, A. Wendt, L. Scruton, J. Taprogge, D. Rudolph, P. Reiter, M. Bentley, V. Avdeichikov, P. Boutachkov, S. Fox, J. Gerl, C. Gorgen, R. Hoischen, N. Kurz, B. N. Singh, G. Pascovici, S. Pietri, H. Schaffner, M. Taylor, S. Thiel, and H. Wollersheim, "The lund-york-cologne calorimeter (lycca): Concept, design and prototype developments for a fair-nustar detector system to discriminate relativistic heavy-ion reaction products," *Nuclear Instruments and Methods in Physics Research Section A: Accelerators, Spectrometers, Detectors and Associated Equipment*, vol. 723, pp. 55 – 66, 2013.
- [51] J. Hoffmann, "FEBEX3 manual," July 2013.
- [52] S. L. Jorn Adamczewski-Musch, Nikolaus Kurz, "Mbs reference manual," Nov 2017.
- [53] V. Panin, *Fully exclusive measurements of quasi-free single-nucleon knockout reactions in inverse kinematics*. PhD thesis, Technische Universitat, Darmstadt, November 2012.
- [54] U. collaboration, "Official webpage of the urqmd collaboration," 2018.
- [55] V. Sundararaman, "Effect of bremsstrahlung on scattered gamma ray spectra," *Nuclear Instruments and Methods*, vol. 171, no. 3, pp. 561 – 565, 1980.
- [56] J. Park, "Private communication," 2017.
- [57] "Atan2 definition," September 2018.
- [58] H. Landolt, R. Bornstein, H. Fischer, O. Madelung, and G. Deuschle, *Landolt-Bornstein: Numerical Data and Functional Relationships in Science and Technology*. No. Bd. 17 in Numerical Data and Functional Relationships in Science and Technology Series, Springer, 1987.
- [59] C. A. Bertulani and C. De Conti, "Pauli blocking and medium effects in nucleon knockout reactions," *Phys. Rev. C*, vol. 81, p. 064603, Jun 2010.
- [60] C. Bertulani, "Differential cross section calculation elastic proton-proton scattering at 200 MeV (private communication)," 2018.
- [61] D. Koerper, "Private communication," 2017.

Danksagung

Zum Abschluss meiner Arbeit möchte ich mich noch bei allen bedanken, die mich in der vergangenen Zeit unterstützt haben.

Zu Beginn möchte ich mich bei Prof. Laura Fabbietti für die interessante Themenstellung bedanken. Desweiteren bedanke ich mich bei Dr. Roman Gernhäuser für seine wissenschaftliche Betreuung und seinen allzeit unermüdlichen Einsatz bei Fragen aller Art. Zusätzlich danke ich Prof. Elisa Resconi für die Anstellung als Systemadministrator und Prof. Stefan Schönert für die Anstellung als wissenschaftlicher Mitarbeiter.

Meinen (ehemaligen) Kollegen bin ich besonders zu Dank verpflichtet. Hierbei seien vor allem Max Winkel, Philipp Klenze, Patrick Remmels und Felix Stark erwähnt, wegen ihrer geduldigen Hilfe und Unterstützung, und den vielen netten Unterhaltungen während meiner Zeit am Lehrstuhl. Danken möchte ich auch Steffen Maurus, Joana Wirth und Tobias Kunz für die lustige Zeit im Serverraum und bei verschiedenen Systemadministrations-Sessions, sowie die vielen Kaffeepausen, die jederzeit für eine willkommene Ablenkung vom wissenschaftlichen Alltag gesorgt haben. Neben diesen Aktivitäten unterstützten sie mich auch mit ihrer wissenschaftlichen Expertise und bei wunderlichen Codebugs in root. Rico Burkhardt, Bernhard Hohlweger und Raimund Heigl danke ich für das legendäre gemeinschaftliche Physikstudium, die, manchmal, sinnlosen Diskussionen und einfach die genial Zeit, die wir gemeinsam verbracht haben. Auch Ralf Lang und Michael Klöckner möchte ich für ihren geduldigen und hilfsbereiten Einsatz in der Werkstatt danken, sowie allen Kollegen bei E12/E62, für die andauernde Unterstützung und sehr angenehme Arbeitsatmosphäre.

Besonderer Dank gebührt meiner Frau Sarah, die mich nun schon seit über elf Jahren auf meinem Lebensweg begleitet und mich in jeder Minute unterstützt und motiviert hat, meine Ziele zu verfolgen und mich aufgebaut hat, falls es mal nicht so lief. Dabei war die Geburt unseres gemeinsamen Sohnes Kilian eine weitere Quelle der Freude und Motivation, die vor Kurzem in unser gemeinsames Leben getreten ist.

Nicht zuletzt möchte ich mich bei meinen Eltern, meinem Bruder und meiner restlichen Familie für deren ständige moralische Unterstützung und Beistand in den letzten Jahren bedanken, ohne den all das nicht möglich gewesen wäre.

List of Figures

1.1	Potential well with energy states of protons and neutrons in the Fermi gas model. Due to the Coulomb repulsion the potential for the protons is lower than for neutrons. The Fermi energy E_f are thus different for the two different types of nucleons. Above the Fermi energy the states are unoccupied. To remove a nucleon from the potential well the binding energy E_B needs to be expanded (based on [2, p. 42])	2
1.2	Single particle energy levels for nucleons using shell model calculations and their splitting due to the spin-orbit interaction introduced by Mayer-Goepfert and Jensen[8]. The shell closures and magic numbers appear at particularly large gaps between successive energy levels[7, p. 257]	4
1.3	Illustration of the tensor forces in the interacting shell model. Figure a) illustrates the tensor force between a proton in the $j_>$ or $j_<$ orbit and a neutron in the $j_>'$ or $j_<'$ orbit. If the spins of the proton and the neutron couple constructively to a total spin of $S = 1$ and parallel to the radial distance between them, the force is attractive. In the opposed case of a coupling of the proton's and neutron's spin to $S = 0$ and perpendicular to the radial distance between the particles, the tensor force is repulsive. Figure b) illustrates the shifting of the orbitals energy due to the tensor forces between protons and neutrons interaction with pion exchange[10]. .	4
1.4	The dependence of the reduction factors R on the difference in separation energies of protons and neutrons ΔS [16].	5
1.5	The Facility for Antiproton and Ion Research (FAIR) extends the existing GSI Facility in Darmstadt.[18]	7
1.6	Overview over the individual detectors of the R ³ B experiment. The radioactive ion beam supplied to the experiment by the Super-FRS irradiates the target area. Projectile-like charged particles and heavy fragments are analyzed by the GLAD dipole magnet and subsequent detectors. Neutrons are detected by the NeuLAND detector. Target-like charged particles and γ -rays are detected by the CALIFA calorimeter. Additionally the L ³ T silicon tracker is used for vertex reconstruction.[20] .	7
1.7	Sketch of a (p,2p) reaction in normal kinematics. The beam proton scatters on a bound one in the A nucleus at rest and knocks it out. After the reaction the two protons are emitted with polar angles $\theta_{1,2}$. The residual $A-1$ nucleus is left at the target position as spectator. If the reaction populates an excited state of the $A-1$ nucleus, emission of γ radiation becomes possible.	10
1.8	Cross section for proton-proton and proton-neutron scattering at energies below 200 MeV[28]. Both cross sections increases strongly for decreasing proton energy. In case of the (p,2p) reaction at low beam energy leads to an increasing probability of final state interactions in the shape of re-scattering of protons with energies below 60 MeV off the nucleons.	10

1.9	Schematic picture of the CALIFA calorimeter with its three parts. This highly segmented calorimeter is made up of 2560 detector units, which are divided into the Barrel (red, 1952 CsI(Tl) crystals), the iPhos Endcap (blue, 512 CsI(Tl) crystals) and the CEPA (green, 96 LaBr ₃ (Ce)/LaCl ₃ (Ce) phoswich detectors) part[20]	12
2.1	Comparison between raw and MWD pulse	18
2.2	Illustration of QPID windows	19
2.3	Example QPID neutrons	20
2.4	Example reduced QPID neutrons	21
3.1	Overview of the Bronowice Cyclotron Center. In green the Proteus C-235 cyclotron is visible, as are the beamlines leading to the different medical and experiment sites. The gantry setup (red) with a revolving beam line is used for medical applications and two experimental halls (E1 and E2) are available for physics experiments. The location within hall E1 used for the experiment is indicated in blue [44].	23
3.2	A figure illustrating shell model configuration of the ¹⁶ O target before the (p,2p) reaction and residual ¹⁵ N afterwards[34]. In figure a) the ¹⁶ O target nucleus configuration before the reaction with it's closed proton and neutron shells (double magic) is shown. After the knockout of one proton from the 1p _{3/2} shell the residual ¹⁵ N is left in an excited state (figure (b)). The removal of a 1p _{1/2} shell proton results in the ground state of ¹⁵ N as shown in figure c).	24
3.3	Level scheme of ¹⁵ N reduced to emission radiation created by excitation of ¹⁵ N from 1p _{3/2} shell proton knockout using data taken from [46]. The three relevant 3/2 ⁻ states with 6324 keV, 9925 keV and 10702 keV level energy cascade with the indicated branching ratios to the ground state. Note that the 6324 keV level decays only decays directly to the ground state, while the other two lines populate three intermediate states as well.	25
3.4	Excitation energy spectra of ¹⁵ N resulting from ¹⁶ O(p,2p) ¹⁵ N in direct kinematics ($E_{beam} = 392$ MeV) measured with a two-arm spectrometer in Osaka, Japan [47]. Figure a) shows the correlation of the energy detected in both arms (GR and LAS). The ground state and two excited states of ¹⁵ N are observed as sharp correlation bands. Towards lower energies a broad distribution is observed. Figure b) shows the reconstructed excitation energy E_x is shown, where the ground state and three excited states with 6.32 MeV, 9.93 MeV and 10.7 MeV are observed as well as higher excitations (s-hole states). Note, that the intensity of the ground and 6.32 MeV excited state are attenuated by a factor of 10.	25
3.5	Schematic drawing of the water target. A medical cannula is used to create a thin water fiber. This water is collected in a collection vessel from which a pump is transporting the water through medical tubing to the cannula again. To ensure a constant water pressure a syringe with a pressure gauge is used as a compensating volume.	27
3.6	Picture of the target mount mechanics. Figure a) shows the crane like universal mounting structure with the water target mount (schematic cf. figure 3.5) on the left and a solid state target mount on the right. Below the water target mount the collection vessel is visible. To adjust the position on the target, high precision measures are visible at the top with an accuracy of 0.5 mm. Figure b) shows the 0.46 mm water jet illuminated by a laser beam.	28

- 3.7 Beam profile recorded on radio-sensitive film. Upper spot represents the default 6 mm x 5 mm slit setting (measures: $dx = (6.5 \pm 0.1)$ mm, $dy = (5.3 \pm 0.1)$ mm) while the lower spot represents a 5 mm x 2 mm slit setting (measures: $dx = (3.0 \pm 0.1)$ mm, $dy = (2.8 \pm 0.1)$ mm). The lower one was used for the water target. 28
- 3.8 Overview over the Petal demonstrator unit. Left a schematic overview of the CALIFA Calorimeter with a Petal unit cut out of the full calorimeter. One unit represents 64 crystals of the forward part of the Barrel (red). Right side shows the interior of a Petal unit. The silvery wrapped crystals with the LAAPDs (white squares) mounted on top are clearly visible with their individual connection to a flat ribbon cable and packed into units of four crystals per Carbon fiber Alveolus. In the middle two empty alveoli are also visible. 29
- 3.9 Overview of the DSSSD detector. On the left side the full detector is shown, with the detector mounted on the back plate of the aluminum housing already connected to the 32 channel preamplifiers. The front cover was removed here. On the right the DSSSD is shown mounted onto a PCB with readout connectors for preamplifier. The individual strips on the front side are clearly visible here. 30
- 3.10 Figure a) shows the MPRB-32 preamplifier specifically designed for the readout of the CsI(Tl) detectors. It contains two independent 16 channel preamplifier modules with a common power supply and individual pulser and slow control connectors. In figure b) the rack containing 20 FEBEX3 digitizer cards complete with FAB boards to read out the total 320 detector channels. The cards are separated in two FEBEX crates for power supply, trigger bus and fiber readout. 31
- 3.11 Raw signal traces of one strip of a silicon detector sampled with the FEBEX3 ADC at 50 MHz decimated by a factor of 2. On the y-axis the pulse height in arbitrary units is plotted versus the time in 40 ns samples on the x-axis. The characteristic fast rising edge of the silicon signal is clearly visible. The data was taken with $E_{\text{beam}} = 200$ MeV on a polypropylene target. 32
- 3.12 Raw signal traces of a CALIFA Petal detector in 300 MeV range sampled with FEBEX3 ADC at 50 MHz decimated by a factor of 2. On the y-axis the pulse height in arbitrary units is plotted versus the time in 40 ns samples on the x-axis. The traces show the characteristic slow rising edge of the CsI(Tl) scintillator as well as the preamplifier decay with $\tau=35$ μ s. The data was taken with $E_{\text{beam}} = 200$ MeV on a polypropylene target. 32
- 3.13 Overview of the experiment's setup. Figure a) shows a schematic view from the top of the setup. The **proton beam** comes in from the top hitting the **target**. The setup is separated into two detector arms right at the **target**, each containing one **silicon strip detectors** and one demonstrator detector (**petal 0** and **petal 1**). Below the target area, another demonstrator (**petal 2**) is positioned. Figure b) shows the setup as an illustrated picture viewing the experiment from the back. The color code used is analogue to the one used in figure a). 33

4.1	<p>Figures show the kinematic features of a (p,2p) reaction in normal kinematics in this case with a ^{16}O nucleus as target and ^{15}N in the ground state after the reaction. Figure a) shows the emitted proton's energy anti correlation with a constant total sum as should be expected(cf. figure b). The shape of the sum energy peak in figure b) is created by the residual nucleus' recoil momentum leading to a $\Delta E/E \approx 1.0\%$ (FWHM). The polar emission angle of both protons is shown in figure c) which is broadened by the intrinsic momentum distribution of the knocked-out proton. Figure d) shows the sum of the polar emission angle of both protons.</p>	36
4.2	<p>Comparison between polar emission angles of the $^{16}\text{O}((p,2p))^{15}\text{N}$ simulated with different simulation packages. Both figures show the normalized polar angular distribution $\frac{dN}{d\theta}$ is plotted versus the polar angle for the three different event generation approaches. The black dots represent the distribution created by using the Panin generator with the pp cross section, while the distribution in red is created by using the isotropic one. Data from the UrQMD simulation is shown in green. While the distributions created by all three generators vary in figure 4.2b ($E_{beam} = 1000$ MeV), they agree nicely in figure 4.2a ($E_{beam} = 200$ MeV).</p>	37
4.3	<p>Comparison of simulated data using the Panin QFS generator with the pp cross section for $E_{beam} = 50 - 950$ MeV. The data up to $E_{beam} = 450$ MeV shows a similar distribution as expected using the isotropic approximation, but starts to deform towards smaller emission angles starting from 550 MeV, making the isotropic cross section approach invalid with increasing beam energy.</p>	37
4.4	<p>Setup converted into Geant4 geometry. Only the detectors and the water fiber are displayed here to avoid confusion. Red represent the wrapped crystals within the alveoli, the backside of the silicon detectors is shown in blue. In the simulation, all detector housings are considered to ensure an exact representation of the experiment.</p>	38
4.5	<p>Hit distribution of raw data in all detectors with the forward pointing detector arms in the upper row and the third petal below. As expected the majority of quasi free scattered (QFS) protons is emitted in forward direction, but missing each of the arms slightly. Third petal's event distribution starts at the forward facing end, increasing away from the target.</p>	39
4.6	<p>Response of simulated DSSSD with (p,2p) events at $E_{beam} = 200$ MeV. Figure a) shows the correlation of DSSSD x strips corresponding to the polar opening angle of the QFS protons. The plot shows the expected smearing from the intrinsic momentum distribution of nuclei in the target nucleus. Figure b) shows the correlation of DSSSD y strips corresponding to the azimuthal opening angle of the QFS proton emission. The expected back-to-back emission of the QFS protons can be observed.</p>	39
4.7	<p>Vertex reconstruction simulation with (p,2p) events at $E_{beam} = 200$ MeV. The correlation between the DSSSD's x-strips and the crystals's vertical columns show a clear track stemming from the target reactions.</p>	40
4.8	<p>Correlation between the energy deposited in petal 0 and petal 1 for raw simulation data of (p,2p) events at $E_{beam} = 200$ MeV. Two anti correlation lines are already distinguishable from the background. These two correlations are associated to the ground state and excited state event data used as input. The additional third line observed in the histogram is due to energy loss in the DSSSD housing box.</p>	41

- 4.9 Correlation between the energy deposited in petal 0 and petal 1 after QFS selection cuts. Both plots show two anti correlation lines corresponding to the states used as input for the simulation. In plot a) the lines are bent slightly towards lower energy deposition, especially notable for low energy protons as indicated by comparison with the black diagonal. Figure b) shows the same plot with this effect corrected for by using the empiric function 4.1. 41
- 4.10 Illustration of the asymmetric energy loss correction ΔE of (p,2p) protons in petals 0 and 1. This correction was calculated by calculating the variation from the expected linear correlation for petal 0 (ΔE_0) and petal 1 (ΔE_1) individually using 4.2. These create a triangle, its hypotenuses being twice the sought energy loss correction ΔE 42
- 4.11 Sum of the kinetic energy for both protons (a) and coincident γ -rays in petal 2 (b) spectra after the vertex cut in simulation. The energy sum shows peaks for the two simulated states of ^{15}N with a tail towards lower energy deposition. These events stem from reaction in some passive material or the detector itself. In plot b) the full energy peak in petal 2 at 6.3 MeV as well as the single escape peak and a very weak double escape peak can be observed. Note that no finite detector resolution was used in this simulation. Clearly the smearing through Bremstrahlungs-effects in the high energy regime is observable in the missing Compton edges for the photo peaks detected. 42
- 4.12 Cut on the two proton correlation line associated with the excited state (a) with corresponding coincident γ -ray spectrum (b). The 6.3 MeV excitation γ -ray full energy peak was observed with additional some single and double escape peak structure recognizable. The total detection efficiency using events with $E_\gamma > 5$ MeV is $\epsilon = 2.6\%$. Note, that for this simulation a realistic energy resolution of 6% at 1 MeV was implemented. 43
- 4.13 Comparison of γ -ray detection in petal 0 (red) and petal 2 (blue). In figure a) all detected γ -rays are plotted with the full energy and single escape peak clearly observable. The petal 2 (blue) also shows a broad double escape peak, which is strongly suppressed, while petal 0 (red) this seems to vanish within the Compton continuum, as peak statistics are much smaller here. Figure b) shows the remaining γ -ray events after applying a 2 proton cut and a cut on the excitation energy on the simulation data. In both histograms the full energy peak at 6.3 MeV is observed as well as the single escape peak with strongly reduced statistics. Using all three petals combined for proton and γ detection increases the efficiency to $\epsilon_{\text{total}} = 5\%$. 44
- 4.14 Coincident two proton correlations (a) and γ (b) detection using the whole CALIFA calorimeter with the same number of events as used in figure 4.13. The effect of increasing the angular coverage is drastic in terms of the γ spectrum showing a single full energy peak far above the background opposed to figure 4.13. Using CALIFA an efficiency of $\epsilon_{\gamma, \text{simCALIFA}} = 40.8\%$ is expected. 44
- 4.15 Figure shows the simulated excitation energy spectrum from direct energy measurement. The ground state and 6.3 MeV used as simulation input are observed as well as a background tail towards higher excitation energies. Their width is 2.0 MeV(GS) and 2.1 MeV(6.3 MeV) in FWHM. 45

5.1	Energy spectra of γ -rays emitted by a ^{60}Co source. Figure a) shows a single crystal spectrum from petal 0 in low gain mode. The 1.173 MeV and 1.333 MeV lines can be clearly distinguished from the compton background and are nicely separated. Their resolution is $\frac{\Delta E}{E}(\text{FWHM}) = 5.6\%$. Figure b) shows a single crystal spectrum from petal 2 in high gain mode. Apart from the higher statistics due to a lower distance to the target, the two peaks are even better separated than in figure a). Their resolution is $\frac{\Delta E}{E}(\text{FWHM}) = 4.6\%$.	48
5.2	Figure a) shows the calibrated ^{60}Co spectra of each crystal in petal 0 identified by its crystal id. The calibration of the two peaks was succesfull as they can be found at their associated energy. Some detectors differ concerning their energy threshold setting as the resolution of the lines seems to vary between the detectors. Figure b) shows the calibrated ^{60}Co spectra of each crystal in petal 2 identified by its crystal id. The calibration of the two peaks was succesfull as they can be found at their associated energy. The thresholds and individual resolutions look more homogeneous in figure b) compared to a).	48
5.3	Figure a) shows the energy correlation between petal 0 and 1 from raw data taken with a polypropylene target and a 200 MeV proton beam. The anti correlation line of the elastic scattered protons is observed next to background created by reactions in the air. The anti correleation line is not straight but made up of several individual peaks with varying energy sum. Figure b) shows the energy sum of petal 0 and 1 for the same data. A large peak with a tail toward smaller energies at 213.5 MeV is identified as the sum peak of the elastic scattered protons ($\frac{\Delta E}{E}(\text{FWHM}) = 2\%$). The tail is associated with the scattered composition of the anti correlation line in figure a). The secondary peak is associated with background reactions in the air.	49
5.4	Correlation plot between the crystals in petal 0 and petal 1 for data taken with a polypropylene target and a 200 MeV proton beam. The stair like structure in the plot indicates correlated events in a crystal pair from elastic scattering exhibiting a constant energy sum to calibrate on. The square shaped area in the upper right corner, and the two bands protruding from it, are due to reactions of beam protons in the air after the target preferably hitting the forward detector elements.	50
5.5	Figure a) shows the proton calibrated energy correlations for petal 0 and 1 from the raw data taken using the polypropylene target and a proton beam with 200 MeV energy. After the calibration the anti correlation line is now straight except for acceptance effects at the edges. Translated to the energy sum in figure b) the tail of the peak is reduced, increasing the resolution to $\frac{\Delta E}{E}(\text{FWHM}) = 1.5\%$	51
5.6	Hit pattern of the used DSSSD detectors. Figure a) shows the pattern measured by DSSSD0. Most noticable feature of the hit pattern is the red shaded rectangle associated with the DSSSD pixel coincident with the petal detector behind it. This feature is observed due to the trigger method used(cf. chapter 3.2.3). The remaining area shows a homogeneous irradiation decreasing towards higher strip numbers indicating the side of the DSSSD being tilted towards the beam. Figure b) shows the hit pattern of DSSSD1. It shows similar features as figure a), but the petal projection is smaller. Together with the higher overall event rate of DSSSD1, a slightly lower distance to the beam could be the reason.	52

- 5.7 Hit pattern of the DSSSDs with the strip number converted to mm. Figure a) shows the the hit pattern of DSSSD0 and figure b) the one of DSSSD1. The features remain unchanged by the conversion as should be expected. The petal projection in figure b) is 1.5 mm smaller than the one in figure a). 52
- 5.8 A drawing of the setup with all relevant measures in cm with 0.1 cm accuracy(source [56]). Figure a) shows the tow view with all three petals in respect to the DSSSD detectors and the target. Note, that the petal detectors where tilted by 15° and the DSSSDs by 23° with respect to the beam axis. As indicated by the projection, the DSSSD detector does not completely overlap with the petal detectors. Figure b) shows the setup's front view facing in beam direction. The measurements represented in this picture are used to calculate polar and azimuthal angle, distance to the target of the detectors and so on. 53
- 5.9 Reconstruction of the detectors position in respect to the target with the DSSSDs and petal 0 and 1 displayed in this figure. Based on these, more sophisticated calibration steps such as the DSSSD's angle calibration are done. The distance to the center of the DSSSD can be calculated as 9.9 cm (DSSSD0) and 9.4 cm(DSSSD1). The center of the petals was positioned 41 cm from the target. 53
- 5.10 Figure a) shows the x strips of DSSSD0 plotted versus the x strips of DSSSD1 to illustrate the polar angle correlation. Between the strips an anti correlation line is observed, indicating a polar angle correlation between two emitted particles. Figure b) shows both DSSSD's coordinates calibrated to the polar emission angle with respect to the target using equation 5.2. Both DSSSD's cover a polar angle range from 40° to 58° . The opening angle of the correlated particles is $\theta_{opang} = (85.8 \pm 0.9)^\circ$ 54
- 5.11 Figure a) shows the y strips of DSSSD0 plotted versus the x strips of DSSSD1 to illustrate the azimuthal angle correlation. An anti correlation line through the center of the plot is observed, indicating a symmetric particle emission from the target. Around the center of the plot, the event distribution is stronger than towards the edges as the central strips are closest to the target. Figure b) shows both DSSSD's coordinates calibrated to the azimuth emission angle with respect to the target using equation 5.3. Both DSSSD's cover an azimuth angle range from -14° to 14° . The opening angle of the correlated particles is $\phi_{opang} = (179.8 \pm 6.7)^\circ$ 55
- 5.12 Vertex reconstruction histograms for a polypropylene target run with $E_{\text{beam}} = 200$ MeV. Plot a) shows the petal 0 columns plotted against the X strips of DSSSD 0. A correlation between 0 to 14 and the strips 0 to 30 is observable. The cut drawn in black is defined using equation 5.4 to select events emitted from the target. Plot b) shows the same for petal 1 and DSSSD 1. The correlation is observable in this plot as well. Note, that the alignment is slightly different. 56
- 5.13 Histogram showing DSSSD-petal correlations without target. The anti correlation line observed in figure 5.12 vanished as expected. This behavior proofs the anti correlation belonging to particles emitted from the target location. 57

5.14	Particle Identification (PID) histograms for a polypropylene run with $E_{\text{beam}} = 200$ MeV in reduced representation. Here the individual crystal's PIDs of the petals were summed up. Plot a) shows the PID using petal 0, while plot b) shows the same for petal 1. In both plots several branches are observed, mainly stopped and punch through protons but also heavier particles, like deuterons, tritons and helium can be observed. The multiple peaks on the stopped proton line correspond to the discrete proton energies from the elastic p-p scattering. In figure a) the analytical function (cf. equation 5.6) used for selecting stopped proton events is drawn.	58
5.15	Figure a) shows the a PID sum plot with selection on the proton punch through branch and the two proton energy correlation. Since the elastic protons should be stopped in the petal detectors no events should be observed in either figure. Events observed were misidentified by the PID and used to determine the efficiency. 389 events are observed on the elastic proton anti correlation line in figure b).	59
5.16	Histogram showing polar angle correlation for a polypropylene target run with $E_{\text{beam}} = 200$ MeV with a cut on the polar angle correlation associated with the elastic scattered protons. The cut is done analytically as described in equation 5.7.	60
5.17	Selection on elastic proton events using the vertex, PID and opening angle cuts from a data set taken with a monoenergetic proton beam $E_{\text{beam}} = 200$ MeV on a polypropylene target. Figure a) shows the energy correlation plot between petal 0 and petal 1. Compared to figure 5.5, most of the background is removed and the anti correlation line associated with the elastic scattered protons remains. Note, that due to the limited overlap of the DSSSD and petal detectors, the anti correlation line shortens. Figure b) shows the sum energy of both petals. The sum peak associated with the elastics is still observed with an increased signal to background ratio compared to 5.5. The total energy resolution after the cuts increases to $\frac{\Delta E}{E}$ (FWHM) = 1.2%.	60
5.18	Raw data from combined runs with monoenergetic protons $E_{\text{beam}} = 200$ MeV irradiating the water target. The elastic scattering visible by the anti correlation between the deposited energy in petal 0 and 1 are clearly distinguishable. Being similar to figure 5.3a indicates the p,2p signal being being by background from non-target reactions.	61
5.19	Data from combined runs with monoenergetic protons $E_{\text{beam}} = 200$ MeV irradiating the water target with vertex and opening angle cut. In a) their deposited energy in petal 0 and 1 is plotted against each other. As the acceptance is now limited to the DSSSDs due to the cuts, the anti correlation line shortens. Additionally most of the background is now removed leaving an almost clean spectrum. Note the vertical and horizontal distribution leading toward the anti correlation line, where the energy was measured only in one of the petals correctly due to reactions within the CsI(Tl) detector. Plot b) show the sum of both petals for these cuts. The full energy peak is clearly separable from the background with an energy resolution of 1.2%.	62

- 5.20 The correlations between the energy deposited in petal 0 and petal 1 for all water target runs combined at $E_{\text{beam}} = 200$ MeV. Figure a) shows the data after isolating the QFS protons from the rest of the data. Due to the Fermi momentum of the knocked out proton, the angular correlation is smeared out, leading to two energy bands visible in the plot over the whole energy range. Both lines are slightly bent by the difference in energy loss for both protons respectively. In figure b) this is compensated for analogous to the simulation data using equation 4.1. 63
- 5.21 Figure a) shows the sum energy of the protons detected in petal 0 and 1. Using a combined fit of three Gaussian functions with linear background (red curve) three peaks (black curves) can be observed corresponding to the ground state at 186.3 MeV, the 6.3 MeV excited state at 180.3 MeV and the 9.9 MeV excited state at 176.2 MeV. With a proton separation energy for ^{16}O $E_s = 12.13$ MeV[46], the calculated separation energy $E_{s,meas} = (12.22 \pm 0.02)$ MeV is consistent with each other. A resolution of $\frac{\Delta E}{E}$ (FWHM) = 1.9%(GS), $\frac{\Delta E}{E}$ (FWHM) = 2.1%(6.3 MeV) and $\frac{\Delta E}{E}$ (FWHM) = 2.3%(9.9 MeV) was achieved. Note the small peak adjacent to the ground state resulting from elastic proton events surviving the p,2p event selection. Figure b) shows coincident events detected in petal 2 as excitation γ -ray candidates. The full energy peak at 6.3 MeV (red) is observed above the background. Also the 511 keV (green) is visible ($\frac{\Delta E}{E}$ (FWHM) = 9%). 63
- 5.22 Figure a) shows a section of the proton sum energy plot. Three energy selection windows for a detailed investigation of the coincident γ -rays are illustrated on the plot. Window 1 selects coincidents with the ground state, window 2 coincidence with the 6.3 MeV excited state and window 3 coincidence with higher excited states (s-hole). Figure b) shows selection on the 6.3 MeV excited state of ^{15}N (window 2). The 6.3 MeV peak is nicely separated from the background after applying this cut. Due to Bremsstrahlung and secondary compton scattering the 6.3 MeV peak's compton edge is smeared out and no single or double escape peak can be clearly identified. The resolution achieved is $\frac{\Delta E}{E}$ (FWHM) = 1.95%. Figure c) shows the γ -ray spectrum using a kinematic selection on the ground state (window 1). Populating the ground state no γ -ray will be emitted. The figure illustrates the background present during the experiment. Also a few events are visible in the region of 6.3 MeV due to peaks being not perfectly separated in figure a). Last but not least figure d) shows the selection on higher excited states (window 3). No clear lines remain except for the 511 keV line. Some feed down from higher excited states attributes to the bump structure at 6.3 MeV. The 9.9 MeV line is not observed in any of the figures b) to d). Also no background subtraction was done in any of the figures. 65
- 5.23 The figure shows a γ -ray spectrum of petal 0 and 1 coincident with the population of the 6.3 MeV state of the ^{15}N nucleus. A small bump at 6.3 MeV indicates the excitation γ -rays with no clear peak observable. Due to efficiency loss from isolating the particle hits in petals 0 and 1, the γ -ray add back does not work as in petal 2. Also secondary radiation from δ -electrons in the detector material smears out the full energy peak. This underlines the need for cluster finding algorithm for CALIFA. 66

5.24	Residual momenta of the ^{15}N nucleus for the ground state (blue), 6.3 MeV excited state (red) and a kinematic simulation of the ground state with $\sigma_{p_F} = 100$ MeV (green). Figure (a) shows the residuals momentum in x dimension P_x . All three histograms agree with each other, with the simulation having a slightly larger width. In figure (b) the distribution of the momentum P_y measured in the experiment is dominated by the setups acceptance and is narrower than the simulated distribution. The lacking geometric coverage of the setup in azimuthal direction dominates the spectral shape. Figure (c) displays the residual momentum distribution P_z . While the experimental data is restricted by the experiments geometrical acceptance to only the positive part of the momentum distribution, the simulation shows a asymmetric distribution around $P_{z,\text{max}} \approx 26$ MeV/c with a tail towards positive momenta. The central position of the ground state momentum is shifted to $P_{z,\text{GS,max}} \approx 60$ MeV/c, while the excited state distribution is even shifted to $P_{z,\text{GS,max}} \approx 78$ MeV/c. This indicates larger excitations of the residual nucleus being correlated to a shift in the residual's P_z towards larger momenta.	67
5.25	Comparison of the excitation energy measured directly (blue histogram) and the excitation energy calculated by missing mass spectroscopy (red histogram). Both methods create exactly the same spectra, making them equivalent, as should be expected. In total the ground state and two excited states at 6.3 MeV and 9.9 MeV are identified next to the tail towards larger excitation energies associated with s-hole states. The width of the excited states is determined to $\sigma_{gs} = 1.8$ MeV, $\sigma_{6.3\text{ MeV}} = 1.6$ MeV and $\sigma_{9.9\text{ MeV}} = 2.0$ MeV	68
5.26	Figure illustrating experimental cross section data measured by various groups in comparison with theoretical calculations(curve [59]). The black data points represent the total and the green data points the elastic p-p cross section (data source [58]). Here is clearly observable, that for proton energies below 400 MeV both are the same. Above 400 MeV also other reaction mechanisms become relevant and the elastic cross section diverges from the total cross section.	70
5.27	Figure shows the theoretical calculations of the differential (p,p) elastic scattering cross section at 200 MeV beam energy[60] to detect one of the protons. The red data set shows the cross section in the center-of-mass system. Using equation 5.13, the black data showing the cross section in the laboratory frame of reference are calculated from the given CMS data set.	71
5.28	Figure shows the normalized event distribution per polar angle measured by the DSSSDs. The red dots represent the experiment data taken using the water target, while the black dots show data from a simulation using the Bertulani cross section. The shape of the distribution's agree with each other, except for the last data point, which is dominated by border effects of the petal and was neglected. The average difference between simulation and experiment is represented by the horizontal lines and is 4.4%.	72
6.1	The figure shows the alignment of one demonstrator petal with the corresponding DSSSD. By the dotted line, the focal point of the petal is projected onto the DSSSD which is not centered properly.	76

6.2	Figure a shows the correlation between the minimum polar angle of the demonstrator θ_{min} (cf. figure b) and the number of (p,2p) events detected by the demonstrator. In green the angle used in the Krakow experiment is indicated (48°), while the optimum angle is indicated by the blue area. This would increase the event rate by approximately a factor of three.	77
6.3	Illustration of light crosstalk between two Crystals	77
6.4	Crosstalk between neighboring crystal in petal at Krakow	78
6.5	Setup of the R ³ B Phase 0 experiment (picture taken from [61]). The beam line from the Super-FRS enters the picture from the left. Right before the GLAD magnet around the target, CALIFA and the L ³ T silicon tracker are positioned for detection of target-like fragments and γ -rays. For neutron detection NeuLAND is positioned downstream of the magnet. The projectile-like are detected using the TOF detectors after the GLAD magnet.	79
6.6	Schematic setup of the CALIFA demonstrator with 4 single petals and 2 double petals. Detectors (1,3,5) are positioned in $42^\circ < \Theta < 90^\circ$, while detectors (2,4,6) in $28^\circ < \Theta < 70^\circ$ with a total azimuthal angle coverage is roughly 50%.	80
6.7	Figure a) shows the emitted protons energy distribution from a $^{12}\text{C}(p,2p)^{11}\text{B}$ simulation in inverse kinematics at $E_{beam} = 200$ AMeV. It is smeared out by the ^{12}C nucleus' internal momentum distribution. Due to this, information accessible in normal kinematics like the proton separation energy and a separation of the ground and excited states is lost. Figure b) shows the energy of protons detected by the experiment setup. It shows a part of the distribution in figure a) as only 5.8% of the events are detected in the demonstrator, but the same distribution shape.	80
6.8	Figure a) shows the (p,2p) protons' polar emission angles taken from the primary track vectors (perfect angular measurement). The sharp correlation between the emission angles leads to a well defined polar opening angle $\theta_{op} = 80.1^\circ$ and indicates the importance of proper angular measurement. In comparison figure b) shows the polar emission angles measured by the demonstrator within its acceptance. The correlation observed in figure a) is reproduced with limited resolution.	81
6.9	Figure a) shows the (p,2p) protons' azimuth emission angles taken from the primary track vectors (perfect angular measurement). The expected 180° opening angle can be observed by the correlation between the emission angles. In comparison figure b) shows the azimuth emission angles measured by the demonstrator within its acceptance. Due to a not continuous azimuthal coverage only parts of the correlation lines observed in figure a) is reconstructed.	81
6.10	Figure shows γ -ray spectra using the energy measured by the demonstrator and different angular measurements for Doppler reconstruction. In the black histogram the raw data is shown. Only a broad peak is observed and no full energy peak can be discerned. Using the primary vector angles results in the blue histogram. A peak at 4.446 MeV is observed associated with the full energy peak of the excitation γ -ray with a resolution of $\frac{\Delta E}{E} = 2.5\%$. To create the red histogram the emission angles measured using the demonstrator were used. With the energy resolution only a bit worse with $\frac{\Delta E}{E} = 3.3\%$, the angular measurement's precision is sufficient for a proper Doppler reconstruction.	82

- 6.11 Figure shows the excitation energy reconstructed in inverse kinematics using different angular measurements and the proton energy measured by the demonstrator. In red the excitation energy is calculated using the emission angles of the primary vectors representing the best achievable resolution ($\sigma_{GS} = 136$ keV, $\sigma_{4.4} = 152$ keV). Two peaks associated with the ground state and the excited state at 4.444 MeV are observed and well separated. Using the emission angles measured by the L³T results in the blue histogram. Here also both peaks are observed with a decreased resolution ($\sigma_{GS} = 472$ keV, $\sigma_{4.4} = 491$ keV) compared to the red histogram. Finally the black histogram represents the reconstructed excitation energy using the demonstrator angles. Due to the insufficient angular resolution the peaks are no longer separable and result in one broad distribution. 83
- A.1 Figure shows a schematic drawing of five silicon detector strips labeled a) to e) to illustrate the inter strip technique. The arrows represent particles passing through the silicon strips. The red arrow passes only through strip a) and so angular measurement is limited to the position information gained by this strip. The green and purple arrows both pass through two strips each with different ratios of energy deposition. While in case of the green arrow more energy is deposited in strip b) than in strip c), for the purple arrow the situation is reversed. This defines a weighting factor for the angular measurement introduced in equation A.1. 85
- A.2 Figure shows the correlation between energy deposited in adjacent strips i and j in arbitrary units. In figure a) shows a prominent correlation between the energy deposited in strips i and j. The cut out corner around the origin of the histogram is produced by the DSSSD strips individual threshold set to 100 a.u., which in this case cuts into the correlation, as the overall signal is small compared to the threshold selected. Figure b) shows the energy deposition in adjacent strips for DSSSD1. As in figure a) a correlation is clearly observed, but opposed to before the signal is at least by a factor of two larger, making the cut off effect of the trigger threshold negligible. 86
- A.3 In figure a) the distribution is chaotic with the highest intensity in row three, so the upper end of the petal. As column 15 was closest to the beam line, one would expect the highest intensity to be found there. Also the whole distribution is checkered so the channel mapping seems to be wrong indeed. Figure b) shows the event distribution after applying the mapping. The distribution is now sorted from high intensity to low from column 15 to 0. Also the rows now have roughly the same intensity per column. 87
- A.4 Figure a) shows the unsorted events distribution. The odd even staggering and the highest intensity in the lower left corner of the plot indicate the need for remapping the crystal positions. Figure b) shows the remapped event distribution. The plot shows the expected intensity sorting as in figure A.3, but with an additional feature in the row 1 and 2 for columns 2 to 10, where the intensity is lower than in the surrounding crystals. This effect is due to the DSSSD mounting table between the petal and the target. 87

List of Tables

5.1	Summary of γ efficiency calculations	67
5.2	Cross sections for $^{16}\text{O}(p,2p)^{15}\text{N}$ for the total reaction and the ground and 6.3 MeV excited state population separately	72
5.3	Measurements of $^{16}\text{O}(p,2p)^{15}\text{N}$ cross section by other groups as comparison to the calculated values [25][45].	73
6.1	Comparison between the requirements of the CALIFA calorimeter and the parameters determined for the demonstrator petals in the Krakow experiment. Note, the single crystal values for the petals are mean values. Resolutions are given in FWHM.	75
6.2	Summary of light crosstalk observed at TRIUMF[43] and Krakow.	78